3D MATERIAL CYTOMETRY (3DMAC): HIGH-THROUGHPUT, HIGH REPLICATE SCREENING OF MATERIALS USING FLOW CYTOMETRY

A Dissertation

Presented to

The Academic Faculty

By

Kirsten Helen Parratt

In Partial Fulfillment

of the Requirements for the Degree of

Ph.D. in the

Interdisciplinary BioEngineering Program -

School of Materials Science and Engineering

Georgia Institute of Technology

August 2018

3D MATERIAL CYTOMETRY (3DMAC): HIGH-THROUGHPUT, HIGH REPLICATE SCREENING OF MATERIALS USING FLOW CYTOMETRY

Approved by:

Dr. Krishnendu Roy, Advisor
Department of Biomedical Engineering
Georgia Institute of Technology

Dr. Valeria Milam
School of Materials Science and Engineering
Georgia Institute of Technology

Dr. Robert Guldberg
School of Mechanical Engineering
Georgia Institute of Technology

Dr. Johnna Temenoff
Department of Biomedical Engineering
Georgia Institute of Technology

Dr. Hang Lu
School of Chemical and Biomolecular Engineering
Georgia Institute of Technology

Date Approved: July 20 2018

To my husband, Seth, for all of his support and patience.

ACKNOWLEDGEMENTS

I would like to think that this is just my dissertation, but many people contributed to reaching this point and I am thankful for their help. Of course Dr Roy has been instrumental directing my work, interpreting results, and dealing with my stressing. For all of his advice, scientific or otherwise, he is a wonderful PI. The members of the Roy Lab, especially Ingrid, Joscelyn, and Michael, have contributed countless ideas and time troubleshooting. Also, this thesis would not have been possible without the contributions of dedicated high school and undergraduate students (Qwantayvious Stiggers, Madeline Smerchansky, Simran Dhal, Ama Asseh, Kate Richardson, and Zahra Mousavi Karimi); learning and working with them has been one of the best parts of graduate school.

I am grateful to my committee members for their help troubleshooting this project, as well as our collaborators in Dr Peng Qiu's group. The broader BioE community has helped me tremendously; especially Laura Paige, Dr Andrés García, and the BGA. I would also like to thank Carol Mills, Lakeita Servance, Dr Manu Platt, Dr Robert Nerem, Aqua Asberry, Sommer Durham, Angela Lin, Andrew Rae, Andrew Shaw, Dr Kira Smith, Dr David Lawrence, and Dr Kate Williams.

Finally, there is life outside the lab and I am grateful for the support of everyone who listened to rambling discussions of cells-in-gels. This includes Karis and Melody, Gabe, and countless BioE, BME, and MSE students. (I also acknowledge the *Hamilton* soundtrack which played on loop while writing my dissertation to motivate me to write non-stop and never be satisfied while editing.) Finally, my parents Susan and Steffen, my brother Justin, and my husband Seth have been wonderfully supportive throughout graduate school and I am so thankful that I have them.

TABLE OF CONTENTS

LIST OF TABLES

LIST OF FIGURES

LIST OF SYMBOLS AND ABBREVIATIONS

3DMaC	3D Material Cytometry
AR	Alizarin Red
BMP-2	Bone Morphogenic Protein-2
CSMA	Chondroitin Sulfate Methacrylate
CyTOF	Mass cytometry, Cytometry by Mass-of-Flight
DAPI	4′,6-diamidino-2-phenylindole
DHR	Dihydrorhodamine 123
DMEM	Dulbecco's Modified Eagle Medium
DMMB	Dimethymethylene Blue stain
DMSO	Dimethyl Sulfoxide
DNA	Deoxyribonucleic Acid
DTT	Dithiothreitol
ECM	Extracellular Matrix
ELISA	Enzyme-Linked Immunosorbent Assay
ELISpot	Enzyme-Linked Immunospot
FACS	Fluorescence Activated Cell Sorting
FBS	Fetal Bovine Serum
FSC	Forward Scatter
GMP	Good Manufacturing Practices
HA	Hydroxyapatite
HAMA	Hyaluronic Acid Methacrylate
hBMSC	Human Bone Marrow Stromal/Stem Cell
HEPES	4-(2-hydroxyethyl)-1-piperazineethanesulfonic acid
hMSC	Human Mesenchymal Stromal/Stem cell. Human Medicinal Signaling Cell
HTS	High Throughput Screening
I2959	Irgacure 2959
IDEAS	Image Data Exploration and Analyis Software
IPN	Interpenetrating Network
ISX	ImageStreamX Mark II, imaging flow cytometer
LAP	Lithium phenyl-2,4,6-trimethylbenzoylphosphinate
MMP	Matrix metalloproteinases
NVP	N-vinyl Pyrrolidone
PBS	Phosphate Buffered Saline
PDMS	Poly(dimethylsiloxane)
PEG	Poly(ethylene glycol)
PEG-4NB	Poly(ethylene glycol) 4-armed norbornene terminated
PEG-4SH	Poly(ethylene glycol) 4-armed thiol terminated
PEGDA	Poly(ethylene glycol) diacrylate
Pen-Strep	Penicillin - streptomycin
PMT	Photomultiplier Tube
PNIPAAm	Poly(N-isopropylacrylamide)
qRT-PCR	Quantitative Real Time Polymerase Chain Reaction

ROS	Reactive Oxygen Species
sGAG	Sulfated Glycosaminoglycan
SSC	Side Scatter
SSF	Shape-, Size-, and Fluorescence-barcoding
TBS	Tris Buffered Saline
TE	Tissue Engineering
TGFβ	Transforming Growth Factor beta

SUMMARY

Biomaterials have become a common feature in everyday life ranging from disposable daily contact lenses to implanted devices engineered to outlast the patient. There is a great deal of unrealized commercial potential for biomaterials systems and ample interest in determining optimal biomaterials for applications such as tissue engineering (TE) and detection of biological analytes. Unlike past challenges in polymer selection, candidate biomaterials need to be tested while also accounting for the complexity of living cells and the variability in biological systems. These challenges can be partially addressed by analyzing a large number of biomaterials in a high-throughput manner with high replicate number; however, such methods are lacking.

This thesis shows how flow cytometry can be adapted to the study of biomaterials. Flow cytometry allows for the automated collection of a large number of unique events in a short time period and is already widely used for cell analyses. Here, biomaterial, specifically hydrogel, constructs are fabricated and a combination of shape-, size-, and fluorescence-barcoding (SSF) enables high-throughput, high replicate, highly multiplexed analyses using imaging flow cytometry. This dissertation illustrates how this new method, 3D Material Cytometry (3DMaC), can be applied to tissue engineering and analyte detection, and discusses how the method can be extended to additional biomaterial studies.

CHAPTER 1 INTRODUCTION

1.1 Overview

The definition of a biomaterial continues to be widely debated, and has different meanings for different fields.[1, 2] In the field of medical materials, a biomaterial can be considered as "a material intended to interface with biological systems to evaluate, treat, augment or replace any tissue, organ or function of the body".[1] Biomaterials in clinical use today include hip and knee implants, contact lenses, heart valves, and dental implants, among others.[3] Additionally, the definition of biomaterials can also include diagnostic tools such as biosensors that, for example, measure blood glucose level[3] or blood oxygen level[4]. Regenerative or tissue engineering (TE) is a subfield focused on replacing organs with materials that can support a seeded cell population to function as the replacement tissue.[5] In 2007, it was estimated that the worldwide commercial sales of tissue engineering products reached $1,500 million and that 1.2 million patients had been treated with such products.[6]

Although biomaterials have been translated to commercial products;[6] similar to many fields biomaterial research suffers from irreproducibility of data. This problem is fully explained by Halsey et al.,[7] and some of the key points of that paper are discussed here. Biological assays inherently suffer from high "noise" that limits experimental reproducibility, and current analytical methods often have low statistical power. Additionally, individual cells in a population can have large differences in gene expression.[8] Together, these limitations result in incomplete and often poorly reproducible data, and potentially skewed results. This is in part due to low replicate numbers ("n") leading to low powered studies.[9] Biological replicates are often expensive in terms of time and money, and true differences between groups may be small.

However, without a large number of replicates, the statistical power of the study can be too low to discern the true differences between experimental groups and can also lead to a high proportion of false positives.[9]

There is therefore a need to increase the replicate number in biomaterial studies. Additionally, a high replicate number necessitates a high-throughput assay to process the samples in a time-efficient manner. Often the best solution is to miniaturize samples as this avoids ballooning costs and time; however, miniaturization introduces new organizational challenges during experimentation and analysis. Many of these challenges can be addressed within the flow cytometry-based 3DMaC method that uses size, shape, and fluorescence barcoding to analyze individual microhydrogels. Flow cytometry collects data on individual events, analyzes nano- to micro-sized materials, and has existing data handling methods for high replicate number. For each of the applications discussed in this dissertation, there is great need for high-throughput, high replicate analysis of biomaterials.

1.1.1 Tissue Engineering Applications

In order to select the best materials for engineered tissue, screening methods compare a large number of biomaterials at once. Currently, the need for replacement organs and tissues dramatically outstrips the supply and this deficit is projected to grow.[10] Given this dearth and the challenges posed by potential immune responses to allogenic tissue, artificial tissues composed of polymeric scaffolds with autologous cells are a promising

alternative.[11] However, rules to predict *a priori* which scaffold materials will cause desired cellular function on a patient-specific basis have not been established.

Currently the field has settled on "rational design" to select biomaterials; meaning that materials are selected on the basis of similarity to the desired *in vivo* microenvironment.[12] However, it is still important to screen materials to determine which native material properties are most important to replicate. Given the large number of independent variables when forming a polymer network, the optimization of scaffolds requires high-throughput testing to evaluate the design space. This is especially true when studying the effect of material composition on a differentiating stem cell population because a range of responses are expected due to the heterogeneous starting population.[13] The 3DMaC analysis method is well-suited to the future of biomaterials research because of the ongoing push towards personalized medicine. This is important from a clinical perspective as 3DMaC analysis could be used to select a scaffold material that enables optimal cell differentiation for each individual patient.

In this dissertation the osteogenic differentiation of MSCs (defined here as mesenchymal stem cells and discussed further on pg. 34) is used as a model system to demonstrate how 3DMaC could be applied to TE biomaterials analysis. Poly(ethylene glycol)-based (PEG) polymers are widely used in TE scaffolds and specifically have been used for osteogenic differentiation of MSCs. The Roy lab has extensive experience using poly(ethylene glycol) diacrylate (PEGDA) systems, including for inducing chondrogenic differentiation of MSCs.[14, 15] This previous work[16] served as major motivation to find a high-throughput

way to compare biomaterials and is covered in the Background of this dissertation. Osteogenesis of MSCs in a biomaterial scaffold is important because 5-10% of fractures result in non-union[17] and current techniques to bridge critically-sized defects, such as bone grafts, can result in donor site morbidity. In this dissertation, 3DMaC's ability to measure the mineralization of MSCs encapsulated in different biomaterials is demonstrated.

1.1.2 Bioanalyte Measurement Applications

Biomaterials also are increasingly used for detecting biological species. Specifically, researchers are measuring an ever-growing number of variables related to their biological systems. Due to the convoluted signaling in biological systems, this desire to measure as many variables as possible is understandable. Broadly characterized as "'omics" research, there is a need to increase the number of variables that can be measured in a single study.[18] At the same time, it is important that new high-throughput tools for detection maintain high specificity and low background signal. Hydrogel biomaterials make good detection platforms because their hydrophilicity decreases non-specific binding which would increase background signal.[19] Additionally, many hydrogels have tunable chemistries that allow for the conjugation of antibodies such that high specificity is maintained via the relatively high affinity of antibodies for specific analytes.

Antibodies are used to determine specificity in many biodetection assays such as ELISA (enzyme-linked immunosorbent assay)[20], Luminex[21], and ELISpot (enzyme-linked immunospot)[22]. Protein segments of the antibody called the antigen-binding sites use

non-covalent interactions to reversibly bind analytes of interest. For these detection assays, the antibodies are first chemically attached to a substrate for read-out purposes, for example a 96-well plate or polymeric nano- or micro-particles. Existing detection methods have used size, shape, or fluorescence to barcode different reporters such that multiple analytes can be measured in a single assay. However, the 3DMaC method combines these to yield a massive number of potential barcoding combinations and has the additional benefit of flow cytometry-based data analysis. The Roy lab also has previous experience fabricating large numbers of shape-specific PEG-based particles.[23-25] In this dissertation, 3DMaC's applicability to molecular analytics is demonstrated by measuring protein concentrations in solution.

1.2 Hypothesis

The **overall hypothesis** was that by combining microhydrogel shape, size, and fluorescence as multiplexing variables in flow cytometry, a high throughput, high replicate ("n") assay system for biomaterials can be developed. The **overall objective** was to analyze biomaterials using imaging flow cytometry and develop protocols for two different biomaterial applications.

1.3 Specific Aims

1.3.1 Aim 1: Develop and characterize a high-throughput, flow cytometry-based screening assay for shape-, size-, and fluorescence-barcoded microhydrogels.

In this Aim, suitable microhydrogels were fabricated and analyzed using an ImageStreamX (ISX) imaging flow cytometer. This formed the basis of the 3DMaC method.

A. Generate shaped microparticles from relevant hydrogel materials with high "n" and low size dispersity.
B. Develop gating parameters for multiplexed analysis and determine experimental accuracy using the ISX.

Hypothesis: Shape, size, and fluorescence barcodes can be automatically determined from images of microhydrogels collected in the ISX for high-throughput biomaterials analysis.

1.3.2 Aim 2: Demonstrate how 3DMaC can measure the differentiation of encapsulated cells in response to barcoded material compositions.

This Aim studied an important bioengineering model system to demonstrate an application of the developed method. 3DMaC was evaluated to study how material composition influences stem cell osteogenic differentiation by measuring mineralized material.

A. Develop screening assays for evaluating osteogenic differentiation using the ISX.
B. Encapsulate viable cells into microparticles with controlled encapsulation density.
C. Measure the effect of material composition on the mineralization of MSCs during osteogenic differentiation using barcoded, peptide-functionalized microhydrogels.

Hypothesis: MSCs encapsulated in PEG-based microhydrogels and cultured in osteogenic media will produce more mineralization when RGD peptide is incorporated into microhydrogels and less when HAVDI peptide is included.

1.3.3 Aim 3: Characterize 3DMaC's suitability for performing highly multiplexed, microhydrogel-based sandwich immunoassays.

This Aim used 3DMaC as a biomaterials-based detection platform. Existing microhydrogel-based functionalization techniques were optimized for the 3DMaC analysis system such that the SSF barcoded particles serve as platforms for sandwich immunoassays.

A. Expand the number of shape and fluorescence barcodes that can be used.
B. Functionalize microhydrogels for sandwich immunoassays and measure the extent to which protein binding and detection can be maximized.
C. Measure the detection sensitivity of barcoded microhydrogels when detecting a protein standard curve.

Hypothesis: Microhydrogels can be used as substrates for sandwich immunoassays such that highly multiplexed analyses can be performed using 3DMaC.

1.4 Outline

This concludes the Introduction to the dissertation, which detailed the central hypothesis, three Specific Aims, and hypotheses for each Specific Aim. Chapter 2 provides background information regarding biomaterials, high-throughput screening (HTS), and flow cytometry. Chapter 3 covers the first Aim, specifically how the 3DMaC method was developed and its capabilities. Chapter 4 and Chapter 5 illustrate the application of the

3DMaC method to two separate applications, tissue engineering and molecular analytics. Finally, Conclusions and Future Directions are presented. This progression is detailed in **Figure 1**.

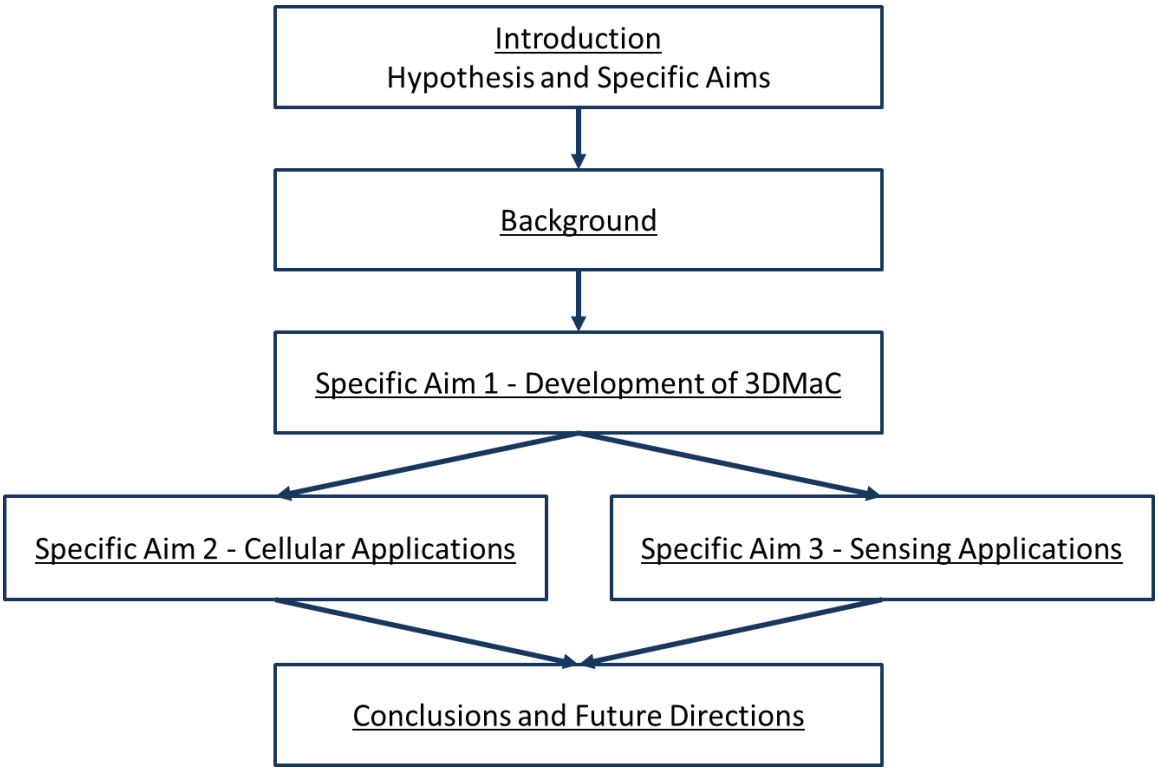

Figure 1. Relationship between Aims

CHAPTER 2 Background

In the Introduction, biomaterials were broadly defined as materials that interact with biological systems or components. The key materials used in this dissertation are hydrogels. In particular, the selection of a hydrogel for tissue engineering focuses on the importance of structure-function relationships that are critical for normal organs.[26] The interactions of materials and cells have been extensively reviewed[2, 5, 26-29] and a wide range of exciting investigations are currently ongoing on topics such as 3D printing and organ-on-a-chip systems, among others. This section discusses the considerations when choosing a hydrogel material for inducing differentiation and then discusses my previous work in the Roy lab selecting materials using a low-throughput method which motivated this dissertation. Next, hydrogels are evaluated in the context of detecting analytes in solution and key characteristics of current technologies are explained. Finally, flow cytometry is reviewed with specific emphasis in the context of assaying biomaterials.

2.1 Hydrogels: Types, Key Properties, and Considerations

Hydrogels are polymer chains that are physically or chemically networked together into a solid that imbibes a large amount of water.[2] In everyday life, Jell-O is a familiar hydrogel consisting of long gelatin chains (denatured collagen) that physically crosslink via entanglements upon cooling. As a result of the network structure and high aqueous volume, hydrogels are an ideal material to mimic the physical and chemical properties of human tissues.

2.1.1 Natural vs. Synthetic Hydrogels

Natural biomaterials were the first investigated TE scaffolds according to historical records[2], and are still widely researched today. The advantage of native biomaterials is that many are inherently bioactive meaning cells have receptors capable of recognizing the material and responding appropriately. This is widely used to control cell adhesion in tissue engineering applications.[29] Natural biomaterials also enable other recognition events, for example, some adhesion proteins contain stretches of positively charged amino acids that will interact with negatively charged ECM (extracellular matrix) components or growth factors.[29] However, natural biomaterials are subject to more concerns regarding sterility, can be mechanically weak, and may have more batch-to-batch variability.[5, 30] Additionally, it may not be clear which property of the material dictates the desired response due to the number of different factors that are not controlled.[31]

Synthetic polymers were not invented until much later and so they did not enter the literature until the 1940s.[2] Many successful biomaterials fall into this category with contact lenses (silicone acrylate) and hip implants (ultra-high molecular weight polyethylene) as familiar examples.[2] The relatively high degree of control over properties is one advantage[31], others include: manufacturability, quality control, and chemical functionality.[28] However, disadvantages includes the need to remove unreacted monomer[2] and limited inherent biological functionality. Poly(ethylene glycol) (or PEG) is a canonical synthetic biomaterial due to its low protein adsorption, high water uptake, ease of chemical modification, and low immunogenicity.[2, 32] It has been used extensively for building TE organs, coating drug delivery vehicles, and preventing surface fouling.[2]

2.1.2 Crosslinking

The networking process that creates hydrogels, called crosslinking, converts a liquid solution into a solid structure capable of supporting applied forces. Depending on the polymer chosen this crosslinking can take many different forms. Physical crosslinking is the simplest, relying on either small nodes of crystallinity (not common in hydrogel systems) or entanglements that form when long chains become wrapped around one another and pulled in different directions.

Chemical crosslinking in hydrogels frequently occurs via ionic bonding, pH changes, temperature changes, or free-radical polymerization. Ionic bonding, for example calcium ions used to crosslink alginate chains, forms reversible crosslinks which is convenient for *in vitro* studies. pH and temperature-based crosslinking reactions are useful in some applications, especially for minimally invasive surgeries and drug delivery applications. However, photo-initiated polymerizations are useful because they can be precisely controlled by the engineer and afford spatial control as well.[32] It is important to note that UV-photoinitiated crosslinking reactions[33] are among the least cyto-compatible due to the presence of free-radicals and so experimental conditions must be carefully balanced to minimize cell death. In this dissertation, relatively high viability has been achieved using LAP (lithium phenyl-2,4,6-trimethylbenzoylphosphinate) as the photoinitiator. This photoinitiator has rapidly replaced I2959 (2-hydroxy-1-[4-(2-hydroxyethoxy) phenyl]-2-methyl-1-propanone), which was previously the predominant initiator for cell-encapsulation polymerizations, due to LAP's higher water solubility and absorbance.[34]

2.1.3 Mechanical Properties

For many tissues the mechanical properties of a replacement scaffold are a key design goal.[26] Mechanical properties are important because the material is expected to fulfill the

mechanical function of the tissue while cells regenerate the injury.[35, 36] Even if the organ does not bear the patient's weight, a scaffold should still mimic the stiffness and elasticity of the native tissue. This is because adherent cells exert forces and organize their cytoskeleton differently depending on substrate stiffness, and therefore it is likely that these interactions are part of cellular decision making.[37] For MSCs in particular, it has been shown that matrix elasticity (in 2D) will direct their differentiation with softer surfaces leading to neurogenesis and stiffer surfaces resulting in osteogenesis.[38]

In the past, bone and other hard tissues such as cartilage have been acceptably replaced by metal or stiff polymers, represented by the success of the hip implant.[39] Soft tissue is better replaced with hydrogel materials whose stiffness can be tuned by modulating the network mesh size and chain composition. In particular, hydrogels are different from metals and ceramics in that they can be "viscoelastic" meaning that they exhibit the elastic-like and viscous-like behaviors found in natural tissue.

2.1.4 Diffusion

Diffusion is a key consideration for cell-containing scaffolds because cells require constant oxygen delivery and removal of waste products to remain viable. In the body, this is achieved through a robust circulatory system with a branching structure to bring blood for nutrient/waste transport within tens of microns of almost every cell.[26, 31] While some tissues operate under hypoxic conditions, for example cartilage, the majority of TE solutions will need to account for this interconnected network.[5] Current solutions generally either design scaffolds that explicitly incorporate such networks during fabrication[40, 41] or include cells that can be encouraged to form new networks[42, 43].

Additionally, diffusion controls the rate at which other signals such as proteins or small molecules will reach a cell. For larger molecules such as proteins, the mesh size of the network may be small enough to impede transport. ECM components such as glycosaminoglycans can also specifically bind to growth factors,[35] which may impede their transport to a cell but could also be used to preload a biomaterial with deliverable protein.

2.1.5 Degradation

Currently, many groups are working to produce transient implants which induce organ regeneration as a superior long-term solution to implanting a permanent synthetic organ. The idea is that the material can instruct resident cells to regenerate the tissue as the scaffold slowly degrades away. This solution avoids many of the issues seen with long-term implants such as stress-shielding-related bone loss and the need for revision surgeries in younger patients.[39] However, the degradation of the material must be programmed to closely match the recovery of the injured tissue so that the tissue functions mechanically throughout the recovery process.[28] In particular, synthetic polymers for TE generally degrade via hydrolysis, which is a time-dependent process that would need to be optimized.[5, 35] Natural ECM materials can be specifically degraded by the human body and these same proteases could be harnessed to degrade a tissue implant.[35] Additionally, any byproducts of the degradation reaction must be biocompatible to avoid poisoning the patient.[5]

2.1.6 Processing, Handling, and Sterilization

Infection of implanted biomaterials is a major issue with 60-70% of all hospital-acquired infections associated with implanted medical devices.[44] Implant infection is estimated at

0.5-5% for total joint replacements and is one of the primary reasons for device failure.[45] Depending on the material used, various strategies can be applied to mitigate the contamination of devices before implantation. Polymers are more fragile than ceramics and so may be more difficult to sterilize compared to some ceramic bone tissue engineering materials.[36] High heat in particular may degrade polymers which would result in changed properties.[2] Ethylene oxide gas is a commonly used sterilization strategy because it will not harm many biologics[27] that would be destroyed, degraded, or denatured by high heat or harsh solvents.

However, none of the described sterilization methods are compatible with the material-cell constructs that are envisioned here because of the fragile nature of cells.[2] Currently, sterility is maintained by processing all components in a GMP-certified environment (Good Manufacturing Practices). Polymers and culture reagents are treated with traditional sterilization methods as appropriate and all cells must be extensively lot tested before use. This is a current major limitation due to the time and money involved with testing cells for a wide range of possible contaminants.

One advantage of polymeric biomaterials, both natural and synthetic, is that they can be processed with relatively mild experimental conditions before end use. Unlike ceramics or metals which may be difficult to process[5], polymers are often handled in a liquid state before conversion to a solid-like final form. This conversion can be a function of time, pH, temperature, or shear stress and this flexibility enables more patient-specific fitting of implanted biomaterials. Especially, some polymer formulations are attractive because they have the potential to be delivered directly to the injury site and crosslinked *in situ* to better conform to the patient's geometry.[46]

2.2 My Previous Work in the Roy Laboratory on Biomaterial-based Chondrogenic Differentiation of Mesenchymal Stem Cells[1]

This dissertation was motivated by previous studies in the Roy Lab focused on selecting materials that induce zone-specific chondrogenic phenotypes in differentiating mesenchymal stem cells. The process of selecting a material involves identification, culture, and analysis, which can take weeks to months depending on the culture period, and analyses performed. This process also presumes that the researcher is starting with materials that have previously shown promise and is looking to optimize around that point. Otherwise, this method would be much too slow and expensive to test novel materials for suitability. While such studies will always be necessary before *in vivo* implementation, the goal of this thesis was to develop a method that could winnow the number of potential materials entering the pipeline. Ideally, only particularly promising materials would be tested to accelerate clinical translation and reduce costs and time.

2.2.1 Introduction

In order to produce polymeric biomimetic constructs for tissue regeneration, it is critical to consider the spatial organization of the chosen tissue, and to do so across multiple length scales as form should dictate function.[47-49] Articular cartilage is a model engineering target due to its spatially-varying structure. It consists of distinct biochemical layers which transmit loads from the articulating surface to the underlying bone with

---

[1] Adapted from: Parratt, K; Smerchansky, M.; Stiggers, Q.; Roy, K. Effect of Hydrogel Material Composition on hBMSC Differentiation into Zone-specific Neo-cartilage: Engineering Human Articular Cartilage with Spatially Varying Properties. *Journal of Materials Chemistry B*, 2017, 5, 6237-6248.

minimal friction, as well as the absence of confounding nerves, blood vessels, or lymphatics. Additionally, cell content in articular cartilage is low, such that tissue mechanical properties are dictated by the surrounding encapsulating proteins and polysaccharides. Native cartilage layers are uniquely characterized by this ECM which constitutes the bulk of their volume. The composition of the ECM gives each layer distinct biochemical and mechanical properties, and imparts a specific phenotype to constituent chondrocytes.[50-52]

Cartilage ECM has two crucial components: collagens (II and X) which help give cartilage its structure, and sulfated glycosaminoglycans (sGAGs) which contribute to mechanical strength. The superficial layer of hyaline cartilage is the "top" layer which forms an articulating surface. As such, the surface has low friction, little compressive strength, and a high degree of fiber and cell alignment.[50] Moving below the surface, there is a gradual shift to the transitional layer with decreasing collagen II, individual cells encased in well-organized pericellular ECM, and sGAGs organized into aggrecan chains for more mechanical strength and water retention.[50] Closer to the bone, in the middle layer, collagen X and sGAGs increase further, and cells are oriented in columns.[50] Finally there is a calcified layer with less active chondrocytes.[50] The ability of material scaffolds to direct stem and progenitor cells towards generating zone-specific levels (relative abundance) of these three parameters, collagen II, X and sGAGs, can therefore be used to identify material compositions conducive of engineering spatially organized human neo-cartilage tissues.

Selected biomaterials must have the appropriate biochemical and mechanical cues to direct encapsulated cells to differentiate into cartilage tissue and adopt different functional phenotypes such that the cells produce an ECM composition specific to each

layer.[53, 54] Although chondrocytes have also been studied extensively for cartilage tissue engineering, clinically this is less tenable than stem cells because harvested autologous (patient-specific) chondrocytes are few in number, expand poorly, and isolation can lead to increased morbidity at the site of removal.[53] Recent work has focused on using autologous stromal cell sources such as human bone marrow-derived stromal cells (hBMSCs) or human adipose-derived stromal cells both with and without biomaterial matrices.[55-59]

Additionally, external culture conditions such as hypoxia or mechanical stimulation[50] can be used to mimic important *in vivo* characteristics that contribute to differentiation and further improve the final phenotype. These variables have been tested on both differentiating hBMSCs and primary, isolated chondrocytes.[60-65] In vivo, cartilage tissue experiences a much lower level of oxygen than the 21% that constitutes normoxic in vitro culture, generally closer to 2-9% in tissues.[66] As such, the differentiation profile of hBMSCs can be expected to change if the oxygen profile were altered. Specifically, hypoxia is thought to maintain a more "stem-like" cell state in which differentiation potential is reduced.[66] However, studies of hypoxia often are conducted on cells cultured on 2D flasks rather than in the context of a 3D hydrogel network. This is important because past studies have shown that 2D and 3D systems can give different results[67, 68] with 3D culture often yielding results more similar to those observed *in vivo*.

Most previous studies have looked to optimize chondrogenesis in a homogeneous tissue structure either by varying material properties or culture conditions. However, cartilage

being a spatially-varying tissue, it is critical to develop spatially-patterned scaffolds constructed of multiple materials and understand the interactions between each layer and how that effects the overall 3D tissue structure.[15] Based on the native tissue, constructs should recapitulate the key characteristics of each spatial "zone" such that the materials can restore function to the tissue and give the cells necessary cues to differentiate into chondrocytes representative of each layer. Therefore, the superficial layer should aim for high collagen II expression, low collagen X expression and low sGAG secretion; the middle layer should aim for the inverse with relatively low collagen II, high collagen X expression, and high sGAG secretion; and the transitional layer should aim to have medium amounts of the ECM components. Together, these biochemical considerations should also lead to mechanically distinct layers that replicate the compressive moduli of the native tissue. Our group has previously evaluated multilayer constructs of similar materials used here; however, that work was done using a mouse progenitor cell line.[14, 15] There have been no reports of constructing a zonally-organized human articular cartilage-like tissue from donor-specific hBMSCs using spatially patterned material scaffolds.

Here we investigated nine different composite, photopolymerizable, interpenetrating hydrogel networks (IPNs), comprised of synthetic PEG-based materials and methacrylated cartilage ECM biopolymers to optimize zone-specific chondrogenic differentiation as a function of material compositions and culture conditions; such that a multi-layered, biomimetic construct can be engineered to generate spatially-organized tissue. Relative chondrogenesis was evaluated via four relevant metrics of differentiation and biomaterial performance: gene expression of collagen I, II, and X, accumulation of sGAGs, compressive modulus, and histological staining. Collagen I is found alongside

fibrocartilage, which was not the goal of this study.[69] These metrics were measured for the biomaterials of interest across two widely used culture conditions: normoxia (21% oxygen) and hypoxia (defined here as 5% oxygen). Based on differences observed in single layers, a multi-layered structure was designed around distinct gradients in collagen expression and sGAG secretion. Chondrogenesis was then similarly evaluated to determine to what extent single material studies could predict performance in a complex, spatially-patterned construct.

2.2.2 Hydrogel Crosslinking

Several test material compositions were crosslinked to generate nine different hydrogel IPNs as detailed in **Table 1**. The compressive moduli of these IPNs were calculated from stress-strain curves (**Figure 2A**) and are shown to have a dependence on both overall polymer content and GAG amounts. **Figure 2B** shows the relative increase in volume of each composition after swelling in water; here the trend is more dependent on the overall amount of included polymer than a specific composition. Higher degrees of methacrylation can be expected to lead to higher moduli as can the inclusion of higher masses of GAG in the prepolymer.[70, 71] In addition to PEGDA, material compositions B and C include low levels of hyaluronic acid methacrylate (HAMA), and D includes a low level of a short peptide, all of which lowered the average modulus by a larger degree than expected. However, gels E, F, G, and I contain 5-10% of chondroitin sulfate methacrylate (CSMA) which resulted in higher moduli. Sample H has a lower level of overall polymer which explains its lower modulus.

These values are below the expected values for native cartilage tissue, which ranges from 0.08 MPa in the superficial layer, to 2.1 MPa in the middle layer, and 320 MPa in the calcified layer (note an almost two orders of magnitude difference from the top to the

bottom layer of the same cartilage tissue).[56, 72] Here, only the highest modulus IPNs tested approached the modulus seen in the superficial layer. However, in synthetic tissue systems based on PEGDA, higher modulus is generally achieved by increasing the crosslink density via higher polymer mass which can result in pore sizes too small to allow for transport between cells and through hydrogel constructs. Therefore, this work did not design material compositions to target mechanical properties and instead kept overall polymer content constant while changing the relative amounts, with an expectation that eventually as these neo-tissues lays down their own matrices, the moduli will increase.

The same trends are not reflected in the relative increases in volume that were observed with swelling. These changes were proportionally smaller than those of the moduli and gels with a higher proportion of PEGDA swelled more. Based on the theoretical calculated degrees of methacrylation, the CSMA has a crosslink on every 4th disaccharide unit whereas the HAMA has a crosslink on every 5th to 6th unit. This means that CSMA gels will have a higher crosslink density which would result in reduced swelling and higher modulus, as observed. Especially in cases of lower degrees of methacrylation, as seen in our HAMA, the network may be heterogeneous with defects that lower overall modulus.[70]

Table 1 Material Compositions Tested for Inducing Chondrogenic Phenotype
Materials were a combination of poly(ethylene glycol) diacrylate, chondroitin sulfate methacrylate, hyaluronic acid methacrylate, and an MMP-degradable peptide.

Sample	PEGDA (%)	CSMA (%)	HAMA (%)	MMP-pep (%)
A	20	-	-	-
B	19	-	1	-
C	18	-	2	-
D	18	-	-	2
E	15	5	-	-
F	14	5	1	-
G	10	10	-	-
H	10	-	2	-
I	9	10	1	-

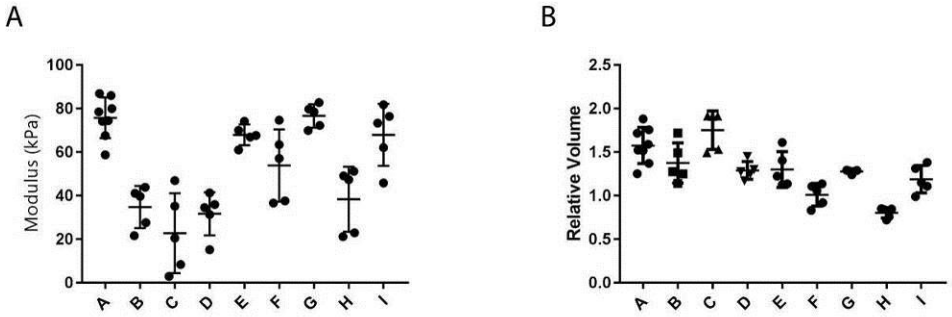

Figure 2 Mechanical Testing of Cell-Free Bulk Hydrogels
Compressive moduli were measured for each of the materials of interest (A). The relative volume of the swollen cell-free hydrogels were also compared with the initial volume of the construct (B).

2.2.3 Characterization of Response

2.2.3.1 Polymerase Chain Reaction

Different hydrogel material compositions were shown to impact the subsequent differentiation of hBMSCs within each experimental condition. **Figure 3** shows the relative gene expression of collagen I, II, and X in each condition as a fold change ratio scaled to the expression of each in the starting hMSC population. These were measured by quantitative Real Time Polymerase Chain Reaction (qRT-PCR). Most replicates were

from separate polymerizations and cell expansions, and so biological variability was high in this measurement.

To better understand relative amounts of collagens rather than overall magnitude, a critical aspect of zonal organization in articular cartilage, gene expression can be expressed as a ratio of the desirable collagen II expression relative to the undesirable collagen I and X expression to control across samples (**Figure 4**). With this new metric, favorable zone-specific material combinations are readily identifiable. It is important to keep in mind that high collagen X levels are characteristic of the middle layer of articular cartilage and so a material with a lower ratio will be more favorable for this layer of the complex construct.

From this data, material compositions can be compared to the widely used pellet culture condition that serves as a positive control. **Figure 3** shows that pellet culture had the highest absolute collagen I and II production, but not collagen X, implying that some materials were creating more hypertrophic tissue. However, from the ratios in **Figure 4** it can be seen that some materials did have more collagen II production relative to the pellet, which is favorable for the superficial and transitional layers of the biomimetic construct. While this data suggests that chondrogenic potential was improved in these gels, future studies should include true chondrocytes as an additional positive control as well as longer timepoints to check for increased hypertrophy. We note also that the trends seen in the compressive modulus data does not predict the resulting collagen ratios, suggesting that biochemical composition of the materials plays a major role. Interestingly, all of the conditions that contained HAMA and had a high modulus (excluding H) had a high collagen ratio, suggesting that this may be a principal factor at this design step.

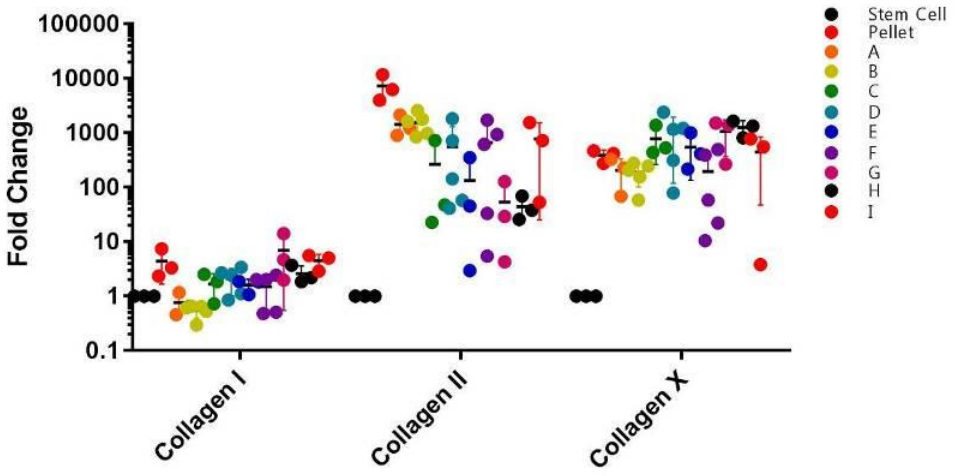

Figure 3 Fold Change of Collagens
qRT-PCR was used to measure the fold change of cells in each material relative to the stem cell population.

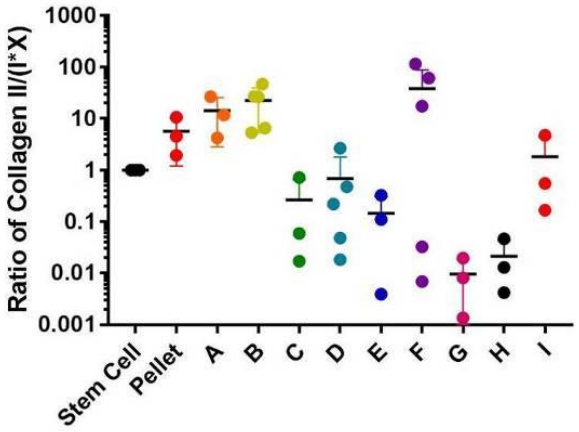

Figure 4 Ratio of Collagen Fold Changes
Fold changes could instead be expressed as a ratio of collagen 2 relative to collagen 1 and 10 to determine the characteristic phenotype.

2.2.3.2 Dimethylmethylene Blue (DMMB) Absorbance

Collagen gene expression represents only part of the ECM regeneration that is of interest in an engineered cartilage; the sGAG content is crucial for water retention in functional cartilage. The DMMB assay quantifies the amount of sGAGs in a hydrogel construct by

dye absorbance of the digested constructs. Experimental hydrogels showed an increase in sGAG production on a per cell basis over the differentiation period. Additionally, many material compositions had high starting CSMA concentrations that would absorb as well. In order to use both the collagen ratio data and the sGAG data as a multivariate discriminator, an sGAG vs collagen ratio plot (**Figure 5**) was constructed which allowed us to readily identify zone-specific "chondrogenic" materials.

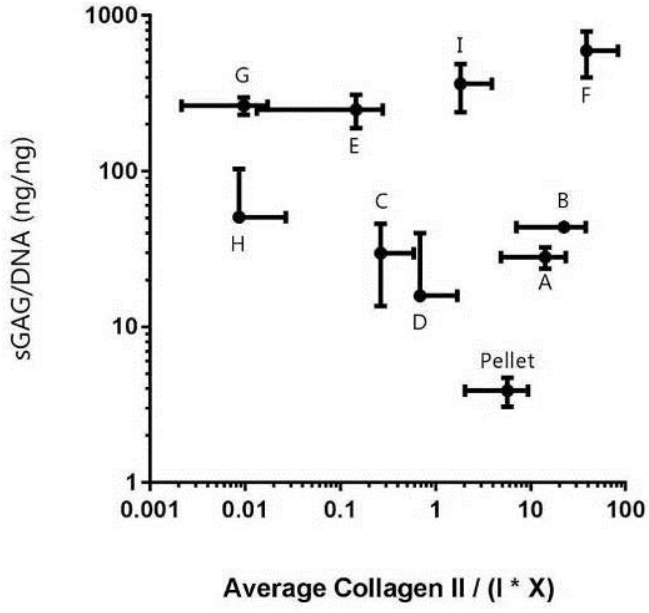

Figure 5 Determining Collagen Ratios and sGAG Production
By plotting the collagen ratio against the sGAG production per cell, it is possible to define the phenotype of the differentiating cells for the multilayered construct.

2.2.3.3 Compression Testing

Figure 6 shows the calculated compressive modulus for the hydrogels after three weeks of culture. Two samples with low moduli had either lower overall polymer content (10% PEGDA + 2% HAMA) or matrix metalloproteinase (MMP)-degradable linkages for the cells to digest the surrounding matrix (18% PEGDA + 2% MMP-pep). The materials

containing only PEGDA and HAMA (A-C) showed a slight increase in compressive moduli over time, possibly because these materials had higher collagen ratios and therefore more chondrogenic ECM was produced. In two of the materials that contained CSMA (G, I), there was a decrease in compressive modulus compared to the blank condition. Because the modulus was not measured immediately after encapsulation; it is possible that decreases in the moduli relative to the blank condition are due to the high cell concentration disrupting the polymer network.

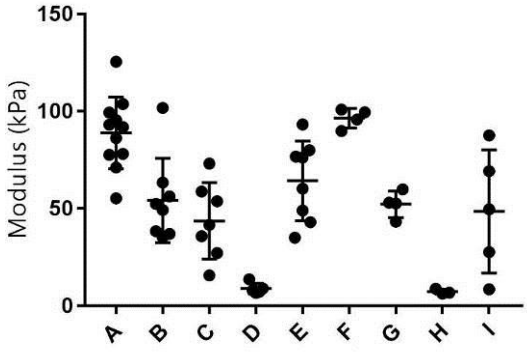

Figure 6 Compressive Moduli of Cell-Containing Hydrogels
Compressive moduli were measured for constructs after three weeks of culture in chondrogenic differentiation media.

2.2.3.4 Histology

Histological staining provides an idea of how the composite engineered tissue will function, rather than a snapshot of cellular phenotype, by revealing the organization of secreted ECM components in the construct. **Figure 7** shows representative tissue sections for each material condition cultured in static normoxia that have been stained with Masson's Trichrome and **Figure 8** shows the same for Safranin-O. In each case, a section of mouse articular cartilage is included as a positive control. In these gels, the staining does not approach that seen in the cartilage, which suggests that these cells may have less

favorable chondrogenesis overall. However, differences were observed between material compositions, suggesting that the material composition was contributing to the eventual cell phenotype.

The Safranin-O staining was less informative because many of the prepolymer conditions contained a substantial proportion of CSMA, a natural sGAG, which caused the entire section to stain. Masson's Trichrome staining for collagens did not show this additional background staining and revealed that the pericellular regions had accumulated collagen, especially in the hydrogels with a higher proportion of PEGDA. Sections with both stains also showed that proliferation varied between the conditions. In particular, the 10%PEGDA and 10%PEGDA + 2%HAMA constructs showed cell number increased but this was not observed when 9 or 10% CSMA was added as well. Given the low cellularity in native cartilage, cell proliferation was not considered in the final complex construct.

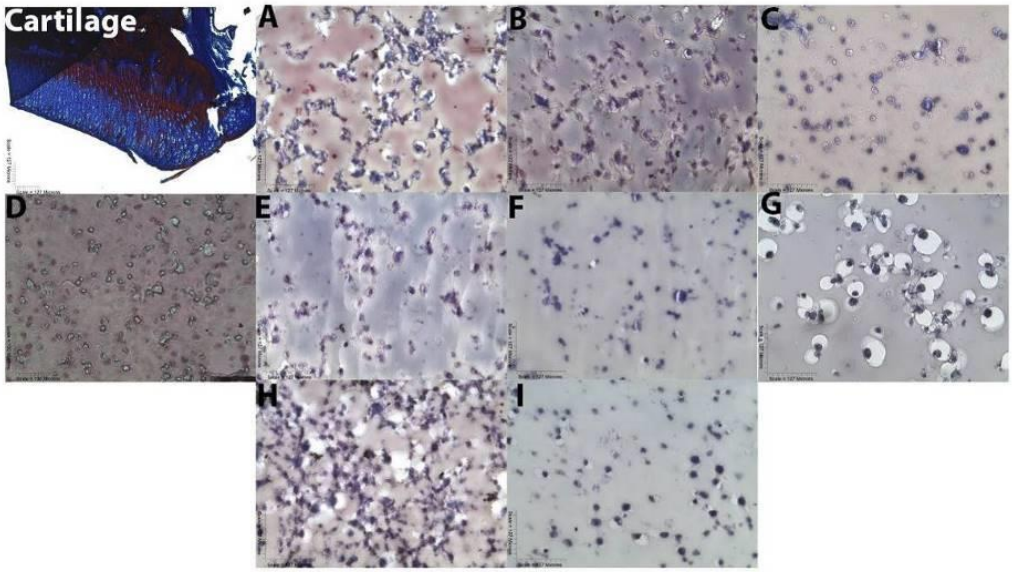

Figure 7 Masson's Trichrome Staining

Masson's trichrome stains collagens blue. Scale bars are 127 μm.

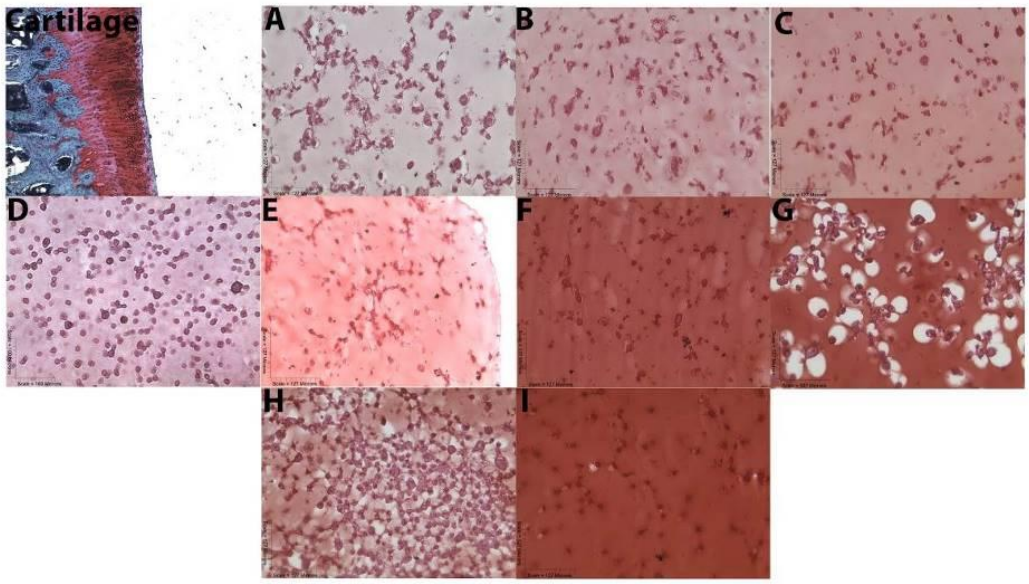

Figure 8 Safranin-O Staining

Safranin-O stains sulfated glycosaminoglycans red. Scale bars are 127 μm.

2.2.4 Hypoxic Culture

Before proceeding to the multi-layered construct, hypoxic conditions were tested for four specific material compositions to determine if more native culture conditions would yield different phenotypes in the same materials. Based on the biomaterial combinations of interest from normoxia, a similar qRT-PCR + DMMB graph then was drawn for hypoxic culture.

Figure 9 shows that this changed the phenotype of the cells in all four materials, but did not necessarily produce more desirable phenotypes. The 10% PEGDA + 2% HAMA and 18% PEGDA + 2% MMPpep hydrogels initially had among the lowest ratio of collagen II expression out of all the tested materials and it was hypothesized that hypoxia may better mimic the *in vivo* environment. These two materials showed that hypoxic culture

increased the average ratio by one to two orders of magnitude, but this increase was offset by a decrease in secreted sGAGs.

The two materials that had initially shown the highest collagen II ratios, 19% PEGDA + 1% HAMA and 14% PEGDA + 5% CSMA + 1% HAMA, were also tested under hypoxia. These materials instead showed a decrease in collagen II ratio of about one order of magnitude and between one and two orders of magnitude reduction in total sGAGs present at the end of culture. The reduction in sGAG in composition F (which has a high starting CSMA concentration) is concerning as it suggests the cells are actively degrading the ECM (catabolic cells) rather than secreting new material. Therefore, all the hypoxic cultures tended towards a specific cell phenotype regardless of the material microenvironment. While this phenotype is "chondrogenic" under the criteria used here, the goal is spatially-patterned cartilage with layer-specific phenotypes, and so hypoxia culture is not suitable for this purpose and was not further investigated.

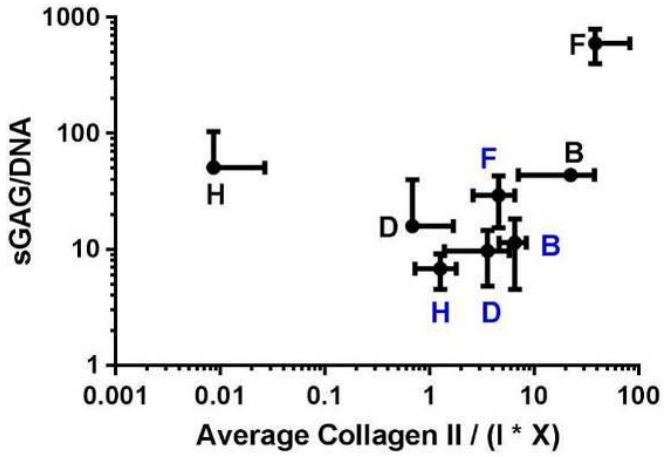

Figure 9 Differentiation Under Hypoxic Conditions
Hypoxia resulted in a convergent phenotype between materials, close to the phenotype of an undifferentiated stem cell. (Black – normoxia, blue – hypoxia)

2.2.5 Multi-layered Construct

Based on the normoxia data, three biomaterial combinations were selected for a multi-layered structure and further study. 19% PEGDA + 1% HAMA had the most favorable collagen II ratio without high sGAG, and so represents the superficial layer. 9% PEGDA + 10% CSMA + 1% HAMA also had a high collagen II ratio along with higher sGAG concentration and so represents the transitional layer. Lastly, the 10% PEGDA + 10% CSMA combination had substantial collagen X and much more sGAG which makes it well-suited for the middle layer of articular cartilage. Our statistical analysis confirmed that layers B and G had different collagen ratios ($p=0.038$) and different sGAG/DNA (sulfated glycosaminoglycan / deoxyribonucleic acid) measurements with a 90% confidence interval ($p=0.065$). Similar to our previous work, layers were partially polymerized in order to form a complete structure.[15] A multi-layered construct with spatially varying material composition was made where the three materials were layered on top of one another in a mold. The middle-mimetic layer was added and exposed to UV for 1 minute at a further distance from the lightsource. This process was repeated for the transitional-mimetic layer. After adding the superficial-mimetic layer, the entire mold was exposed to form a single unit (**Figure 10**). No constructs delaminated after UV exposure or swelling, however, two samples showed incomplete polymerization of the top layer after culture and were excluded from analysis. After three weeks of culture gene expression, sGAG accumulation, and histology were compared.

Relative to the normoxia cases, the multi-layered structure showed the same trends in both collagen expression and sGAG content (**Figure 11**). This was promising as it suggested that materials tested independently could be layered together in the desired order and would maintain the relative phenotypic and zonally-relevant characteristics of that specific layer of cartilage tissue. These trends are reflected in the histological

staining for the multi-layered constructs (**Figure 12A**, **Figure 12B**). The Masson's Trichrome staining is strongest throughout the transitional and middle layers; this could be because Masson's Trichrome stains all collagens and these layers have high collagen I and X expression. Similar to the single layer materials, the Safranin-O staining is strongest for the transitional and middle layers due to their starting sGAG content. Mechanical testing was performed on the intact multi-layered constructs (**Figure 13**). By comparing with the previous data (from **Figure 6**), all the values appear similar and the multilayered structure has a modulus near the individual layer average.

Figure 10 Design of Multilayer
Based on the phenotypes observed in **Figure 5**, three materials were selected.

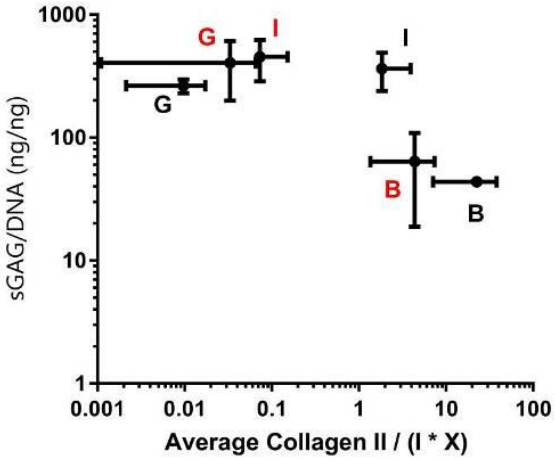

Figure 11 Phenotypes from Multilayer Culture
Phenotypes were evaluated for each layer after being cultured in a multilayer structure for three weeks. Black – Individual materials, red – multilayered construct.

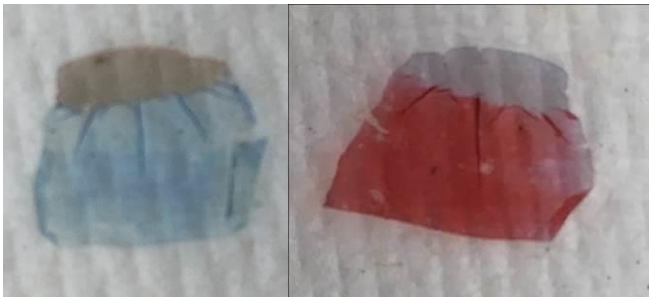

Figure 12 Staining on Multilayer
Masson's Trichrome (left) and Safranin-O (right) stains were collected for the multilayered constructs.

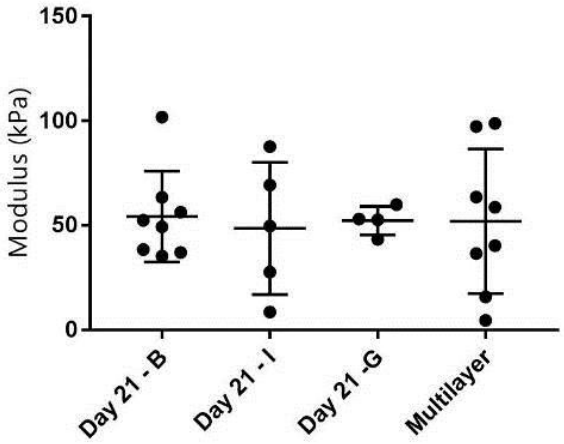

Figure 13 Multilayer Compressive Moduli
Compressive moduli were measured for the individual layers of the multilayered construct and found to be similar.

2.2.6 Conclusion

The purpose of this study was to identify hydrogel materials that direct hMSCs towards three different zone-specific neo-cartilage phenotypes and construct a complex, spatially-patterned cartilage-like tissue. Nine different hydrogel IPN combinations were tested in normoxic culture and compared against differentiation in hypoxia and multi-layered normoxia culture. Of the materials tested here, three combinations were identified as promising for zone-specific differentiation. Multi-layered structures demonstrated that composite hydrogel constructs with spatially varying material compositions can direct a single hMSC population to form a composite tissue with zone-specific, spatially-varying properties, although the resulting zonal properties in single vs composite tissue structures were somewhat different. Specifically, the multi-layered construct was shown to lower the relative amount of collagen II, an important consideration for clinical translation.

Our choices of PEG-based and cartilage-ECM based materials were driven by the polymers' prominence in the field and use in pre-clinical and clinical studies. In the

future, the number of materials investigated should be further increased and tested in composite constructs since this work has shown that single layer optimizations do not necessarily predict how multi-layer constructs will perform. Additionally, researchers should consider whether a material can be 3D-printed to form patient-specific constructs that could be cultured externally before implantation.[73, 74] Based on the studies performed here, future constructs should incorporate hypoxia during expansion to increase collagen ratios since these were lowered in the multi-layered construct. Engineering the zone-specific materials to have a higher initial modulus may also improve the chondrogenic phenotype of the transitional- and middle-mimetic layers. As the field moves toward patient-specific biomaterial implants, it is important to understand better how spatially-patterned, multi-material constructs will function.

2.3 Biomaterial-based Osteogenic Differentiation of Mesenchymal Stem Cells

Tissue engineering aims to replace or rebuild damaged tissue using a combination of biomaterial scaffolds and cells.[30, 35, 36] A wide range of materials, both naturally derived and synthetic, have been tested *in vitro* and *in vivo* to evaluate their chemical and mechanical suitability as a replacement for a variety of tissues. In particular, hydrogel scaffolds are often selected for soft tissue regeneration due to their tissue-like mechanical compliance, high water content, and the ease with which they can be manipulated for implantation.

2.3.1 Key Variables for Cell-Interacting Hydrogels

In addition to their mechanical properties, hydrogels are promising TE materials because such scaffolds can support encapsulated cells. Once swollen in aqueous media, a hydrogel can be largely water by volume which provides cells with a native-like

environment and provides transport through the construct.[75] Research has also shown that cells behave differently in 2D and 3D culture, and testing in 3D conditions may be more representative of *in vivo* responses.[76-78]

Another important property of a TE material is how that material will handle long-term implantation in the body. In addition to the concerns regarding degradation products, implanted biomaterials need to contend with the patient's foreign body response. The human immune system has evolved to resist invasion and unfortunately is one of the greatest challenges to the biomaterials engineer. Any implanted material will immediately be investigated by immune cells in the periphery. The innate immune system will respond first with neutrophils and macrophages attempting to destroy the foreign material.[2]

The body will often construct a fibrous capsule to wall off the implant from the rest of the body thus impeding its function.[2] In cases where this does not occur, the adaptive immune system builds a targeted response specific for antigens on the foreign material thus enabling the body to attack the material precisely.[79] These immune responses can cause dramatic damage to the patient and implants, often requiring removal of the material. This second response is also to be expected when the implant contains allogenic cells as cells are potent antigens.[79]

2.3.2 Human Mesenchymal Stem/Stromal Cells

2.3.2.1 Defining an MSC

All humans start as a collection of embryonic stem cells which are capable of differentiating into all of the cell types found in the body and self-replication. Then these

pluripotent stem cells give way to less plastic multipotent stem cells which are specific for certain types of cells or lineages. Particularly for the osteochondral tissue engineering discussed in this dissertation, the cell type with the highest clinical interest is mesenchymal stem cells (MSCs).

Adult MSCs are a hotly debated cell type, often referred to instead as mesenchymal stromal cells[80] or medicinal signaling cells[81], which are found throughout tissues and in bone marrow, and can differentiate into a range of final cell types.[82] In 2006, the International Society for Cellular Therapy issued a white paper[83] which defined the cells as (1) plastic adherent in culture, (2) expressing CD73, CD90, and CD105, and lacking CD45, CD34, CD14 or CD11b, CD79α or CD19 and HLA-DR, and (3) capable of differentiation into osteoblasts, chondroblasts, and adipocytes *in vitro*. Since this dissertation only focuses on osteochondral differentiation, this is the definition used here. The reader is referred to Caplan[81] for more discussion of these cells.

2.3.2.2 Mesenchymal Lineages and Differentiation

The three defining differentiation pathways for an MSC are adipogenesis, chondrogenesis, and osteogenesis. Adipocytes are found throughout the body and show clear, round fat globules within the boundaries of the cell membrane. Chondrocytes are found in cartilage tissue and show poor expansion in 2D culture, dedifferentiating when removed from 3D culture. Osteoblasts are the cells responsible for creating new bone and deposit mineralized material around the cell membrane.

2.3.2.3 Measuring Differentiation

To evaluate differentiation, there are several assay types that can be performed. The first is a visual inspection; adipogenesis and osteogenesis can be distinguished in 2D culture by the formation of fat globules and mineralization respectively. These can be made more apparent by histological staining, Oil Red or Alizarin Red (AR), which will specifically color the fat or mineral to enhance imaging. Differentiating cells can also be identified through changes in their surface-bound or intracellular markers. Specific antibodies tagged with fluorophores used in immunohistochemistry or flow cytometry allow researchers to precisely label newly expressed proteins or transcription factors that are indicative of differentiation. Finally, many of these same markers can be measured through polymerase chain reaction assays which measure RNA transcript number.

2.3.2.4 Stem Cell Manufacturing Considerations

MSCs are a promising for cellular therapies because they have the potential to differentiate into many tissue types, secrete immunomodulatory signals, and have relatively low immunogenicity.[84] This last trait in particular means that allogenic therapies may be possible, rather than autologous therapies that have thus far dominated. Autologous therapies use patient cells to regenerate a tissue, however, necessary cells are often few in number or diseased. Allogenic therapies, in which a donor provides cells, are already clinically used for treatments such as bone marrow transplant. If allogenic therapies could be developed using MSCs, cell manufacturing technologies such as cell banking could solve the problem of collecting enough cells for transplant, reduce the time to treatment, and increase quality control.[85]

After the successes of the protein manufacturing field, there currently is a push for cellular manufacturing. The idea is that cells are a product like any other and can be

produced in large quantities with reproducible quality control (QC) measurements using similar techniques developed for other products. However, substantial challenges remain to be solved before cells can be shipped and used in the desired off-the-shelf manner. The primary biological challenge is how to obtain consistent results between different batches. Cells will need to be QC-ed at each stage to ensure they have expected performance markers, but often the characteristics most predictive of success are not known. This is particularly an issue for stem cells because the product will be changing through each step of the process and will be sensitive to any stimuli or lack thereof from the outside environment.

The expansion or manufacturing of patient-specific cells come with its own set of challenges in addition to those described above. Specifically, the manufacturing process may need to be adjusted for each cell type/donor depending on the starting characteristics of the cells. Depending on disease state, this may make the expansion impossible or the characteristics more difficult to achieve. But from an immunological standpoint, the patient-specific cells offer fewer challenges because the clinician does not have to contend with any clash between patient and donor cells. Patient-specific cells are likely to need screening for each biomaterials-related application. While a base material might be promising, each patient may respond differently to certain ligands or mechanical properties. The described 3DMaC method has the potential to quickly screen patient-specific cells in the context of a large number of different biomaterials.

2.3.3 Osteogenesis

Osteogenic differentiation of MSCs is well-established *in vitro* and *in vivo*, but there is still great need to regenerate bone tissue in case of injury or disease.[86] Above a critical size, bone cannot bridge the gap to regenerate itself and so instead an autograft is often

used; however, this method has drawbacks relating to the need to surgically procure bone from another site.[46] TE scaffolds are a promising alternative to fill the gap, restore mechanical function, and direct regeneration of the bone. Native bone tissue is complex with anisotropic stiffness[2], but with soft and productive bone marrow on the inside.[87] Unlike many organs, bone has a substantial inorganic component in the form of mineralized material such as hydroxyapatite (HA, calcium phosphate)[27] which gives the tissue substantial strength. On the cellular level, bone is constantly changing with osteoblasts laying down new material and osteoclasts removing unnecessary material.[86] If autologous cells are intended to be used in the scaffold, it is important to remember that the regenerative potential of stem cells can decline with age and injury.[88] Additionally, the implant site may contain scar tissue or show signs of inflammation[35], which could reduce the regenerative capabilities of bone.[89, 90]

2.3.3.1 Mechanical Considerations

Ideally, a scaffold for bone tissue will meet several functional goals. The scaffold will support cells and deliver necessary cues for osteogenic differentiation. The engineered scaffold would ideally model the structure of native bone as well. Bone is divided into cortical and trabecular bone which give the tissue mechanical strength and provide a space for bone marrow respectively.[86] However, bone is challenging to replicate because it is hierarchically organized with specific patterning across several length scales and is highly anisotropic.[91] Similarly, it can be difficult to incorporate biological components with their native architecture, such as fibrillar collagen, without relying on self-assembly.[30]

Mechanical properties of scaffolds for bone tissue engineering are more important than for other tissues for two main reasons. The first is that the patient would ideally like to be

able to mechanically load the bone during the healing process and the second is to avoid the phenomena of stress-shielding where bone tissue is lost because stresses are borne by a stiffer implanted device.[36] The mechanical properties of a biomaterial are also important for directing differentiation. In particular, the modulus[38, 92] and stress relaxation rate[93] have been shown to impact differentiation. The compressive strength of cancellous bone is 5-10 MPa and cortical bone is 130-220 MPa, and the tensile strength is 5-10 MPa and 80-150 MPa respectively.[36, 94] Cells can sense the stiffness of a material via collections of adhesive transmembrane proteins called integrins which are organized into focal adhesions.[95] These assemblies are one route by which cells respond to applied forces; this process is called mechanotransduction.[96]

For most of the crosslinked systems described here, network mesh sizes are likely small because mesh size is inversely correlated with stiffness in synthetic polymer systems. However, bone regeneration scaffolds would ideally have large pore sizes (>50 μm) to allow for cell migration and growth.[10] Therefore, bone tissue scaffolds will likely need a degradation rate matched to the production of ECM by encapsulated cells so that the necessary stiffness is maintained.[86]

2.3.3.2 The Process of Mineralization

During the differentiation process, osteoblasts remodel their environment by encouraging calcification or mineralization of the surrounding ECM. Differentiation media is supplemented with β-glycerophosphate as a source of phosphate groups[35] and this is combined with calcium to produce the inorganic component of bone. This mineralization is called hydroxyapatite though other minerals can also be involved and form different crystal structures.[97] HA nanocrystals form within the organic component of bone (mostly collagen I) at specific nucleation sites with help from acidic proteins.[97]

2.3.3.3 Scaffolds and Biological Molecules for Inducing Osteogenic Differentiation

One of the most potent inducers of osteogenic differentiation is bone morphogenic protein-2 (BMP-2) which was identified by screening the products of bone demineralization.[27] Eventually, a family of similar proteins was identified and found to have sequence similarities to Transforming Growth Factor-beta proteins (TGF-β) which are used to induce chondrogenesis among other uses.[27] Currently, a leading commercially available bone tissue engineering product is INFUSE, a BMP2-soaked collagen sponge that is implanted directly at the injury site.[98, 99] Mechanical strength is a key failing as a collagen sponge does not support compressive forces during the mineralization process.[99]

The source of the biomaterial also determines how the cells or body will respond; natural biomaterials derived from plant sources, ex alginate, lack moieties that human cells will recognize. While there are a massive number of synthetic polymers that can be used to create hydrogel scaffolds, PEG-based polymers are one of the most prevalent. PEG chains can hydrogen bond to water and these hydrophilic chains are commonly coupled to surfaces ("pegylation") to yield a corona of water that repels cells and proteins. This lack of recognizable groups means that cell-instructive chemical groups may need to be added. For osteogenesis in particular, even small molecules have been added to hydrogels to increase mineralization.[100] Synthetic polymers generally also lack biologically relevant functional groups; however, appropriate functionalization chemistries are often experimentally easier because synthetics can be designed with sites for functionalization.

Functionalizing a hydrogel surface with a protein may yield more benefits than supplying free proteins as the immobilized version cannot be consumed by a cell and so remains available to signal to many cells.[35] Peptides are an attractive alternative to including entire proteins. If a short sequence is known to recapitulate the functionality of the

protein, as is true with many integrin binding proteins[29], it can be easier and less expensive to work only with the sequence. In particular, it has been shown that free peptide does not always deliver the same benefits as fixed peptides for maintaining viability of hMSCs (human mesenchymal stem cells).[101] Peptide sequences also limit concerns about denaturation or aggregation, are more stable than a full protein, and can be more homogeneously distributed within the gel.[30, 102] If the ideal conditions are not known at the time of fabrication, peptides sequences can include sites that are cut by cells[103] or by the researcher[104].[30] Peptides can also be added covalently to the matrix later.[105, 106] For all such peptides, it can be important to include a spacer arm when coupling a peptide to a surface to attain full functionality.[102]

To achieve osteogenic differentiation in PEG-based hydrogels in particular, biological functionality needs to be incorporated in the system. Peptides with a cysteine group at the non-functional end of the sequence can participate in free-radical crosslinking via the thiol to become covalently linked into the network. Then the other end of the peptide is available to bind to groups on the surface of cells and direct differentiation. Two commonly used peptides for MSC differentiation contain the sequences RGD and HAVDI. RGD is a functional motif of several proteins including fibronectin, laminin, and collagen IV,[35] which serves as an adhesion site for transmembrane integrins on MSCs. This peptide serves to replicate cell-ECM interactions that would be expected by a cell in the body. As mentioned previously, MSCs are partially defined by their adherent quality and so RGD-containing hydrogels enhance differentiation down all pathways by promoting cell survival in hydrogels. N-cadherin is a transmembrane protein that binds cadherins on adjacent cells and the HAVDI peptide can be used to mimic these cell-cell interactions.[107] HAVDI has been used more recently to help single cells to differentiate as though there are surrounding cells.[59] In particular this is important for chondrogenesis as

the *in vivo* condensation process begins with an aggregate of cells that are eventually separated as they lay down ECM.[107, 108]

Osteogenesis in PEG gels also is dependent on the number of attachment sites for cells. Burdick and Anseth found that increasing concentrations of covalently incorporated RGD resulted in increased number of adhered osteoblasts and increased spreading in 2D culture.[46] When converting to 3D culture where the osteoblasts were incorporated into the hydrogels during polymerization, higher concentrations of macromer were shown to correlate with decreased cell viability over the culture period.[46] However, the viability could be partially rescued by including RGD in the crosslinked network.[46] Importantly, they also found that higher concentrations of RGD peptide resulted in greater mineralization within the 3D matrix.[46]

Cosgrove *et al.* used hyaluronic acid-based hydrogels as a 2D substrate to which they coupled RGD and HAVDI peptide sequences.[107] As a polymer found in native tissue, hyaluronic acid is also biologically active with the ability to bind to cell receptors CD44 and CD168.[109] They found that the HAVDI peptide presentation caused the cells to exert lower contractile forces on the surrounding matrix and consequently the nuclear localization of key transcription factors for osteogenesis was reduced. The authors also concluded that, as the HAVDI sequence mimics cell-cell interactions, this peptide may shield cells from sensing the stiffness of the surrounding matrix. Based on this paper, this dissertation hypothesized that MSCs encapsulated in PEG-based microhydrogels and cultured in osteogenic media will produce more mineralization when RGD peptide is incorporated into microhydrogels and less when HAVDI peptide is included. However, this is in disagreement with another paper in which Zhu *et al.* similarly used hyaluronic acid as a 2D substrate for osteogenic differentiation of hMSCs and found that the addition

of HAVDI resulted in higher expression of a key transcription factor and more Von Kossa staining for mineralized material.[109] Therefore, it is possible that the cell source may be important for determining mineralization or there may be other factors that differ between the two studies.

2.3.4 Screening Platforms

Studies of cell behavior in 3D are inherently more difficult than assays in 2D due to the difficulties accessing the cells for staining or extracting a clear signal through the gel material.[30] Many cell-biomaterial studies are conducted in "chip" format[110-113], which can give good *in vitro* data but is not high-throughput as defined in this dissertation. Currently there exist multiple methods to generate high replicate numbers of cells in a single material or multiple materials; however, there is a need for high-throughput analysis techniques to collect multiplexed data from the 3D cell-material constructs.

While many groups have microfabricated cell-material constructs, unlike for biosensing applications, most of these studies are not designed around multiplexed particles to compare cell-material interactions across materials. Nam *et al.* used shape-barcoded microparticles to indicate cell type; however, cells were cultured in 2D on the particle surfaces and intended for drug screening applications.[114] The Khademhosseini group has developed a range of microhydrogel fabrication techniques and these often involve shape-specific microhydrogels; however the overall goal has been to generate larger tissue constructs via assembly of the microparticles.[115, 116] Some examples of their work includes stop-flow lithography[117], poly(dimethylsiloxane) (PDMS) molding,[118, 119] and temperature-sensitive poly(N-isopropyl-acrylamide) molding of cell aggregates[120].

Currently, printed microarrays dominate high-throughput screening of biomaterial-cell interactions in 2D[121-124] and 3D[125-128]. With the invention of printers capable of depositing biomaterials, engineers could automate the deposition of micron-scale drops of biomaterials such that a large number of conditions could be assayed in a small sample space. This greatly accelerates the testing of many different biomaterials and reduces the associated costs. In such systems, biomaterials are laid out in arrays on glass slides and the position designates the composition of each biomaterial. These printers can be modified to include viable cells and are compatible with many of the biomaterials and crosslinking chemistries described previously.

However, there are a few downsides to these systems. Due to their planar nature, these assays still essentially occupy a 2D space which is an eventual concern for cellular manufacturing applications that use bioreactors to fill a 3D space. There are also experimental considerations as the biomaterial droplets must remain adhered to a slide over long culture periods and they can be prone to delamination. Slide-based arrays also require printers to make, must have randomized placement to eliminate artifacts, and are difficult to assay. Even with an automated microscope to collect data on all the individual droplets and an automated program to process the images, the data collection of a large number of different experimental conditions and necessary number of technical replicates is daunting. Additionally, a portion of samples cannot be removed during culture for testing.

Other groups have used microscopic analysis to obtain image data on a larger than average number of biological replicates within a biomaterials context. This includes work from the Burdick group, where single cell or multi-cell units were imaged and masked to analyze the impact of N-cadherin-mimetic peptide on hMSCs[129], and work from the

Gartner group using DNA-programmed assembly of cells to build specific cellular microenvironments which were analyzed in a 3D bulk hydrogel array[130]. While all of the cells or cell clusters are treated independently in these methods, only a single material is tested at once which was not the goal of this dissertation.

Another highly multiplexed technology is mass cytometry (commercially known as CyTOF, Cytometry by Time-of-Flight).[131, 132] In this method, cell samples are labelled with antibodies that have been tagged with metal instead of fluorescence markers.[132] Next, a cell is sprayed into plasma, which ionizes the sample.[132] This material is then fed into a time-of-flight mass spectrometer that separates out the signals of each of the ions.[132] Compared to flow cytometry this method has lower throughput and is mainly applied to tissue sections or individual cells; however, it generates a large amount of high resolution, multiplexed data. It has been shown to collect as many as 34 variables and could be increased to 100.[132] One interesting modification called imaging mass cytometry that ionizes the sample as a laser moves across the surface thus linking the acquired signal with a specific location.[133] However, mass cytometry is necessarily a destructive process and flow cytometry is not.

2.4 Biomaterials as Detection Platforms

In addition to all of the TE applications of biomaterials described until this point, biomaterials are also widely used for sensing or detection applications. The reader is referred to Le Goff *et al.* for an excellent review of the topic.[134] Biomaterial microparticles are a popular substrate for sensing due to their small size, proportionally large surface area, ease of handling, and generally gentle fabrication chemistries. Hydrogels in particular have been used in many different sensing applications. Some of these applications involve measurement of a physical change in the hydrogel to detect an

environmental condition. For example, the Peppas lab has developed molecular imprinted hydrogels that are designed with a binding pocket specific for an analyte of interest.[135] Upon binding, these materials can undergo a noticeable volume change. pH-sensitive hydrogels have also been developed, similarly these can swell or shrink to indicate pH.[136, 137] A slightly different principle is at play in some temperature-sensitive hydrogels. For example, PNIPAAm gels have a lower critical solution temperature above which they crash out of solution.[120] However, all of these examples are still a single reaction in response to a single analyte or stimuli. For such a method to be able to report on a large number of conditions, the different test substrates need to have a distinguishing barcode.

2.4.1 Barcoding Methods

Several methods have been used to barcode particles for HTS and many are compatible with 3DMaC analysis. Ideally, all of the barcoding variables will be orthogonal such that they can be combined to give high multiplexing and the barcode should not interfere with the detection mechanism. Size is a common detection variable. As described above, a microhydrogel could either grow or shrink in response to an analyte.

Fluorescence can also be used to barcode microhydrogels. The ISX can have four to six lasers that can create signals across ten fluorescence detection channels collected on two different cameras. Using single colors, this gives ten possible barcodes. In order to scale up that number, each channel can be considered “on” or “off” to dramatically increase the number of combinations. For fluorescence barcoding, a key consideration is the degree of overlap in emission spectra that might lead to false positive responses. Because the spectra are additive, the overlap can be computationally accounted for using compensation protocols. Spectra are collected for each of the single-color barcodes and the overlap into each detection channel is calculated. Then when analyzing samples,

compensation is applied to each signal such that only the signal above background is reported. Shape barcoding gives potentially the greatest multiplexing but is the most difficult analysis to automate. While this dissertation only uses the overall shape of a microhydrogel to barcode the composition or analyte, shape more broadly includes any patterning that can be detected in the ISX image. For example, a line-based barcode,[138, 139] as is seen on packaged food, or a dot-based barcode,[140] similar to a QR code, both have been used for microparticles. The number of barcodes that can be designed is limited only by the creativity of the engineer and the ability of the detector to read the barcode.

The detector used in this dissertation is a CCD camera that produces an image of each microhydrogel, therefore resolving different barcodes is an image recognition problem. The primary analysis method in this dissertation is feature-based, meaning that the software has key measurements or features that are used to classify an image. However, potential exists to implement more advanced image processing techniques such as deep learning algorithms.[141, 142] In this case, a large number of training images are fed into the algorithm to develop a classifier, but this classifier is opaque to the user. Depending on the desired multiplexing, SSF barcoding methods can be combined to achieve the desired number of barcodes while maximizing accuracy and throughput.

2.4.2 Fabrication of Barcoded Hydrogel Particles

To achieve the desired barcoding of microhydrogels, many fabrication techniques were considered. These can be broadly characterized as: molded, microfluidic, and spun-cast techniques. The reader is referred to Merkel *et al.*[143] for a review of nanofabrication methods, this dissertation will focus on microfabricated particles that can be visualized by the ISX.

The molding-based methods primarily use PDMS molds to hold the macromer solution in a desired geometry during crosslinking. Generally the patterned features around which the PDMS itself is first molded are made of photoresist; however, it is possible to pattern wafers outside a cleanroom with more accessible materials such as PEGDA.[144] PDMS is a convenient molding material because it is commercially available and frequently used in conjunction with cells. All of the microhydrogels in this dissertation are PEG-based, but PDMS molding has also been used to make PVA (poly(vinyl alcohol))[145], alginate[115], hyaluronic acid[118, 146], and chitosan-PEG[147, 148] microhydrogels. One interesting variation on this method is from Choi *et al*. who used *n*-hexadecane to first coat the PDMS mold such that complex 3D structures could be generated via surface tension.[149] There are also other materials used as molds including perfluoropolyethers in the DeSimone group's PRINT particles,[150, 151] superhydrophobic/hydrophilic micropatterns in the Mano group,[152] and PVA and gelatin in the Park group.[153, 154]

In microfluidic-based methods, a channel is created in a microfluidic device and the macromer solution is flowed through. Then the solution is exposed to light through a mask to crosslink microhydrogels. Extensive work has been done by the Doyle group to optimize microfluidic-based fabrication of microhydrogels, only a few key papers as related to this dissertation are discussed here.[138, 139, 155-160] Generally the microfluidic chip is made of PDMS though Bong *et al.* gives an example of oxygen-free flow lithography achieved with NOA81 resin.[156] The advantage of a PDMS channel when using a free radical polymerization is that there will be a small (~2.5 μm) inhibition layer at each interface which keeps the microhydrogels suspended.[155] Fluid flow simultaneously moves crosslinked constructs to the collection point while also introducing new monomer solution to the crosslinking site. This method was also used by Lee *et al.* for M-ink

microhydrogels[140], Lewis *et al*. for PEG microhydrogels[161], Bong *et al* for complex 3D features,[157] among others. The Doyle group has also built microscope stage-mounted microfluidic devices that will align[158] and then assay[138] their microhydrogels in lieu of a flow cytometer.[139]

The last major category of microhydrogel fabrication methods are those that involve macromer solution cast onto a substrate before crosslinking through a photomask. This primarily involves spincoating the monomer, though the Ghosh group has also loaded HybriWell™ chambers[19]. The advantage of these methods is that a large surface area can be exposed at once to scale up the production of microhydrogels. Both the Ghosh group and Koh groups have focused specifically on using shape-barcoded particles for multiplexed detection. The Ghosh group developed a specific porous hydrogel formulation using microspheres[162] and then fabricated three different shaped hydrogels for protein detection.[19] The Koh group have fabricated shape-barcoded microparticles out of photoresist[114] and PEGDA[163, 164] using this method.

2.4.3 Capture Assays

The hydrogels used in this dissertation are intended as multiplexing substrates and rely on antibodies for their detection ability. Antibodies are bifunctional proteins used by the immune system to patrol the body. One end of the antibody is called the "F_{ab}" portion and this end has two arms which target pathogens or pathogenic components using specialized recognition sites specific to the intended target. Antibodies can have variable affinity depending on the sequence used, many commercially available antibodies have high affinities. The other end of the antibody, called the "F_c" portion, signals to immune cells as to how the pathogen should be processed. In the case of microhydrogel-based detection, the F_c is anchored to the microhydrogel such that the F_{ab} ends are available to

bind analyte in solution. Once an analyte is bound to the microhydrogel (or "captured") by this first antibody, another antibody is then used to "detect" the analyte. Either this detection antibody or a subsequent "reporter" antibody will also be linked to either a colorimetric or fluorescent reporter molecule such that the binding events can be quantified. The exact setup described here is a "sandwich" capture assay because the analyte of interest is sandwiched between two antibodies.

This method of analyte detection is widely used in cell studies and several systems are commercially available. State of the art 2D systems are ELISA or ELIspot kits, and for 3D the Luminex system. The ELISA analysis method uses well-plates that have been functionalized with antibodies to bind protein to the surface and then report on the protein using reporters that can be quantified in a plate reader.[20] ELISA systems look to maximize the number of samples that can be measured in a single study, executed in a plate this could reach 96 or 384 samples at once. The goal of the ELISpot assay is to capture analyte secreted by cells such that the assay shows analyte production on a single cell basis.[22] This method is not highly multiplexed and cannot be easily scaled to high replicate numbers because there is a minimum size needed to accommodate the cell. The Luminex system[165] is different than these systems because the assay is performed on the surface of metallic or polymeric microparticles, intended to provide high multiplexing, and uses flow cytometry as its read-out. The method does require specialized instrumentation, but can measure analyte in smaller volumes and can theoretically assay as many 500 analytes at once.[21] However, this multiplexing is still below what is theoretically possible using SSF barcoding.

Many groups described in the previous subsection have functionalized hydrogel particles to capture and report analyte binding. This is achieved via different chemistries; for

example, capture antibodies can be directly encapsulated in the hydrogel matrix[162] or the F_c end of an antibody can be covalently conjugated to the particle[19, 139] or acrylated probes can be covalently incorporated into the network[166]. Lee *et al.* used color and graphically encoded microhydrogels to achieve theoretical multiplexing of up to 2^{30} barcodes and showed how a DNA hybridization assay could be performed on the microhydrogels.[140] Park *et al.* incorporated acrylic acid into microparticles in order to bind proteins using EDC-NHS chemistry and demonstrated detection of two analytes.[164] Lee et al. also showed how enzymes could be encapsulated in shape-coded microhydrogels to assay two different reactions.[163] This dissertation uses a multistage non-covalent system to attach antibodies to the surface of microhydrogels to maximize experimental flexibility.

2.5 Flow Cytometry: Methods, Advantages, and Disadvantages

Flow cytometry is a widely used cellular analysis method that collects single cell data from hundreds to millions of cells in suspension to characterize the cell population. Depending on the system, cells can be analyzed at a rate of thousands of cells per second which makes it a high-throughput analysis method. Additionally, the technique is also multiplexed because it can record up to 18 measurements on these thousands of events per second.[167] Flow-based techniques have been applied to biomaterials in on-a-chip formats, but to our knowledge commercial flow cytometers have not yet been used to study intact biomaterial constructs.

2.5.1 Operating Principle

The general premise of the technology[168] is that single cells can be collected in suspension and processed using microfluidics. In the fluidics system a steady laminar

flow is maintained to keep the cell suspension in the center of the channel surrounded by sheath fluid. Cells are then passed directly through an interrogation point where one or more lasers of different wavelengths will excite fluorescent labels on or in the cell. While some cell types are auto-fluorescent, most protocols depend on fluorescently-tagged antibodies that will bind with high affinity to components of interest. These protocols can be performed on either live or fixed cells, the latter allowing for intracellular labeling. The emitted light from these fluorophores is measured with photomultiplier tubes (PMTs) and translated into intensity measurements. The data processing also happens in real-time which allows the researcher to draw gates and define the data as events are being collected. This on-line gating is useful to either restrict data collection to populations of interest or to enable a FACS machine (fluorescence activated cell sorting) to divert specific cells from the central channel to collect in individual tubes for further use.

2.5.2 Statistical Considerations

In addition to assaying a range of different materials and culture conditions, it is also important to have a large number of technical replicates within each condition. This is because cells in a population display heterogeneous characteristics[8] and these cannot easily be controlled by the researcher. As a result, testing a hydrogel material containing a single cell or cell cluster may not give a representative result for what might occur *in vivo*. Cell research therefore requires that a large number of replicates be measured within each experimental condition.

The question then becomes how many replicates will be needed to capture this variability effectively in the data. At issue is the statistical power of the study; the higher the statistical power, the more likely that data are an accurate representation. Unfortunately, the true statistical power cannot be known since the entire dataset is not known. Instead,

approximations are made to conservatively estimate what the power might be for a given experiment. In the case of experimental data, increasing the number of samples that are randomly selected from the population can increase the statistical power of the data. As the sample size grows, especially with cellular analysis, it becomes possible to distinguish true outliers (such as might occur due to debris in a flow cytometer) from rare subpopulations.

2.5.3 Big Data Analysis for Flow Cytometry Experiments

Due to its high-throughput and multiplexed nature, flow cytometry successfully collects a large replicate number within only a few minutes. This has been instrumental in defining closely related cellular populations that share many cell surface markers and defining rare subpopulations that could be missed without repeated identification of rare cells. The amount of data collected is in excess of most other cellular studies and more multivariate, and so the field developed a unified ".fsc" format that can be processed using a variety of free or commercial software packages.

Most software packages are based on the same analysis format and there are best practices to process the data. Generally, the strength of the fluorescent signal between samples will vary over several orders of magnitude and so logarithmic or logicle plots are used. A series of scatterplots or heat maps or density maps will be drawn in 2D space and gates (regions of interest) will be manually or computationally drawn around certain portions of the graph. This gate then defines a sub-region which can then be graphed on additional plots with all of the ungated data excluded. Researchers build gating trees in which sub-regions are repeatedly refined by gating on all the measured parameters. This allows the researcher to visualize the relative expression of all the fluorescence markers

and compare subpopulations of interest. Many software packages are also capable of performing more complicated Boolean expressions on the gates as well.

Many gating trees start with a Forward Scatter (FSC) vs Side Scatter (SSC) plot which are two measures of scattered, rather than emitted, light collected at two different angles. The FSC measurement is a rough approximation for the size of a cell whereas the SSC quantifies the internal complexity. Cell types often have distinctive FSC vs SSC profiles and so provide additional delineation between groups. This gating can also remove debris which is smaller than most cells.

The analysis software can perform a variety of statistics on the populations. For example, the total number of data points will be counted as will the number of points in each sub-gate. From these numbers, the software will automatically calculate the percentage of events in each gate overall and in reference to the current plot. The mean, median, and standard deviation can be calculated for each expression level; often the median fluorescence intensity is presented alongside the percentage of cells expressing a certain fluorescent signal to give a more complete understanding of the data. For example, this would reveal if fluorescent signal was relatively even across a population or if there were a few highly stained outliers which brought the average up.

2.5.4 State-of-the-art Imaging Cytometry

More recently, imaging flow cytometers have become available.[169] With increased processing power, these cytometers can collect full brightfield and fluorescent images of every cell which passes through the interrogation point. This addition of a spatial dimension increases the amount of data that can be extracted from each cell because now the distribution of staining can be quantified. For example, it can be determined if a

signal is primarily on the cell membrane or in the nucleus, or if two signals are co-localized. An added benefit is the peace-of-mind that comes from imaging the event; all images can be confirmed not to contain debris that may affect the analysis.

To complement this increase in data, there are changes to be made to data analysis to accommodate the image-based dataset. The first is the application of image analysis methods such as masking or thresholding, in which the user computationally defines rules for the software to analyze regions or signals of interest. Once defined, an analysis template can be automatically applied to extract key measurements such as signal intensity and distribution, but also the previously unknown diameter, circularity, or co-localization. The second improvement involves using analytical techniques such as machine or deep learning which apply large libraries of labeled images to accurately label new images.

CHAPTER 3 Aim 1[2]

Develop and characterize a high-throughput, flow cytometry-based screening assay for shape, size, and fluorescence barcoded microhydrogels.

The goal of the first Aim was to develop a new method for high replicate, high-throughput, highly multiplexed analysis of microhydrogels using imaging flow cytometry. As microhydrogels have not been previously evaluated in a flow cytometer (to our knowledge), this Aim consisted of proof-of-concept experiments to evaluate the extent to which the capabilities of the flow cytometer to measure key cellular variables can be extended to measure microhydrogels. The primary challenges overcome in this Aim were fabricating microhydrogels of the desired dimensions using a cell-compatible crosslinking chemistry, maximizing the throughput of the flow cytometer, and developing an analysis template in IDEAS that could accurately determine the SSF barcodes.

In vitro 3D systems of synthetic or ECM-derived biomaterials containing cells or organoids have become essential for understanding of cell physiology and pathology, unravelling complex disease processes, and developing new biomedical materials to restore function in diseased tissues or deliver therapeutic cells[125, 126, 170-175]. However,

---

[2] Partially adapted from: Parratt, K.; Jeong, J.; Qiu, P.; Roy, K. 3D Material Cytometry (3DMaC): A Very High-replicate, High-throughput Analytical Method using Microfabricated, Shape-specific, Cell-material Niches. *Lab on a Chip*, 2017, 17, 2861-2872.

such approaches suffer from the lack of high-throughput analytical methods that allow rapid measurement of many cell parameters inside 3D niches in a non-destructive manner. Biological assays also inherently suffer from high "noise" that limits experimental reproducibility, and current analytical methods have low statistical power and confidence. Together, these limitations result in incomplete and often poorly reproducible data, and potentially skewed results. Cells, in particular, are highly sensitive to manipulations and changes to their microenvironment. Thus, measurements of their properties and behavior require high replicate numbers to generate high statistical power, reduce false positives, and identify subtle, yet critical differences. Unfortunately, existing methods are time-intensive, low-throughput, destructive, or limit further sample manipulation[122, 124-126, 128, 133, 176-178].

Despite the tremendous impact that flow cytometry has had on biological assays, the technique has been primarily restricted to population-based analyses of cells in isolation and its application to biomaterials has not been realized. Here, we adapt imaging flow cytometry to analyze 3D cell-biomaterial niches. This Aim details how an ImageStreamX (ISX[169]) imaging flow cytometer can be used for HTS of microhydrogels. The ISX takes a picture in each fluorescent channel of every one of the hundreds of particles that pass through the interrogation point each second. This ability to see the sample removes uncertainty surrounding how samples are interrogated by the lasers and adds a spatial dimension to analysis. Microhydrogels were fabricated based on previous work by Khademhosseini[115, 118, 119, 146], Doyle[117, 179], and Koh[163, 180, 181]. Such methods can produce microscale structures with tens of thousands of replicates with high fidelity and low variability, and protocols have been established for rapid harvesting of microparticles containing viable cells.

Based on the sensitivity of the ISX the number of "barcodes" that could be used to designate different material compositions was estimated (**Table 2**). A barcode consists of a chosen size, shape, and fluorescence. The "tested" row describes what was demonstrated and published, "estimated" describes what might reasonably be done based on this dissertation and previous data from the Luminex system, and "theoretical" is the limiting value that might be achieved with complete optimization. As shown in **Figure 14**, this multiplexing is especially useful because the variables are orthogonal and so can be combined into a large number of final barcodes.

Table 2 Proposed Multiplexing
Proposed multiplexing that can be achieved on the ISX based on sensitivities to shape, size, available fluorescent channels, and physical restrictions based on tubing diameters.

	Barcoding Variable			Total Multiplexing
	Shape	Size	Fluorescence	
Tested	4	3	6	72
Estimated	10	4	500	2 e 4
Theoretical	20	6	10!	4 e 8

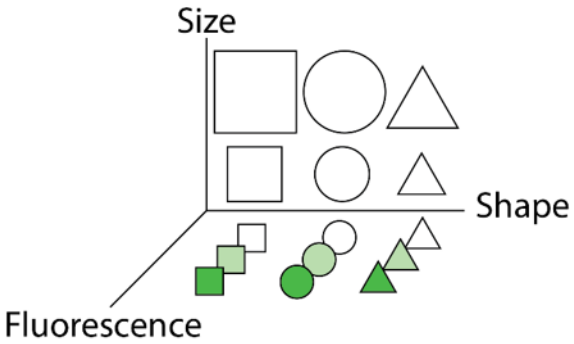

Figure 14 Shape, Size, and Fluorescence Barcoding
Demonstration of how the barcodes can be used orthogonally to achieve potentially huge multiplexing.

3.1 Methods

3.1.1 Materials

Poly(ethylene glycol) diacrylate (PEGDA) was purchased from Sigma (MW 575 or 700) and Laysan Bio (MW 3400). Lithium phenyl-2,4,6-trimethylbenzoylphosphinate (LAP) was purchased from TCI and used as the primary photoinitiator due to its high activation efficiency in the UV range.[34] Phosphate buffered saline (PBS) was used as a buffer. 2% fluorescein o-acrylate or fluorescent nano/microparticles (FluoroSphere) were added for fluorescent barcoding. SU-8 2010, SU-8 2050, and SU-8 developer (MicroChem) were used for wafer patterning. Glycerol was purchased from Fisher Scientific. Poly(vinyl alcohol) (PVA, MW 25kDa) was purchased from Sigma Aldrich. Poly(dimethylsiloxane) (PDMS) was mixed at a 10:1 volumetric ratio of base to crosslinker before use. PNIPAAm-PEG (copolymer of poly(N-isopropylacrylamide) and PEG) was purchased from Mebiol^{R} and stored dehydrated at room temperature until use.

3.1.2 Soft lithography for patterning master wafers and molds

AutoCAD was used to design arrays of desired shapes. In this aim there were twelve tested populations consisting of three different cross-sectional sizes (20, 40, and 60 μm lengths) and four different shapes (square, circle, equilateral triangle, and right triangle). Photomasks were made of chrome-plated soda-lime or printed transparencies (CAD/Art Services). Silicon wafers were spincoated with SU-8 2010 (thicknesses of 5-20 μm) and SU-8 2050 (thicknesses > 20 μm) according to the manufacturer's instructions. The wafers were exposed through a quartz photomask to 365 nm light and excess unexposed photoresist was removed with developer. A 10:1 mixture of PDMS prepolymer and crosslinker was degassed, poured over the wafers, and cured at 65^{o}C for at least 2 hours. Cured PDMS was removed from the wafers using ethanol and dried. The mold face was

protected with tape to prevent dust accumulation and the unmolded side placed on glass slides for handling. This process is shown in **Figure 15**.

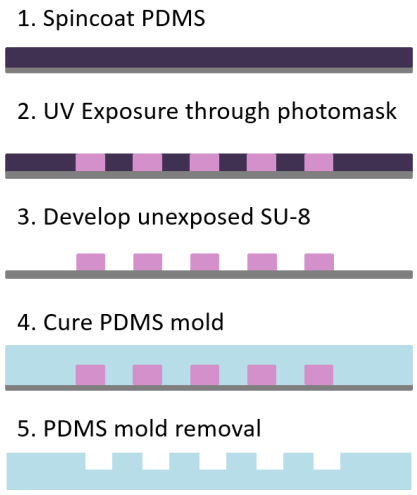

Figure 15 Soft Lithography Process
Steps describing how photoresist is patterned onto a silicon wafer and PDMS molds are produced.

3.1.3 Microhydrogel fabrication and collection

3.1.3.1 Prepolymer

Prepolymer formulations were based poly(ethylene glycol), and fabricated using methods adapted from Khademhosseini et al[115, 118, 119, 146]. PEGDA-based prepolymer consisted of 5-30%(wt/v) PEGDA, 0-0.3%(wt/v) 1-vinyl-2-pyrrolidinone (NVP), and 0.1-1%(wt/v) LAP in PBS. Photoinitiator concentration was chosen to balance between the time required to crosslink under UV light exposure and expected cell viability.

3.1.3.2 Molded Microparticles

Each PDMS mold was treated with oxygen plasma for at least five minutes to reduce the water contact angle and 10-20 µL of prepolymer was immediately spread on the surface.

A pipette tip was used to brush any bubbles from the surface then the mold was sealed with a block of hydrophobic PDMS. This prevents a residual layer from forming between mold wells, thus eliminating any subsequent need for etching. PEGDA-based microgels were cured by exposure to 365 nm light through the top PDMS layer and released by pipetting in PBS. Microparticles were collected in low-adhesion Eppendorf tubes and centrifuged.

3.1.3.3 Spincoated Microparticles

The fabrication throughput can be scaled up by instead spincoating the prepolymer onto a silicon wafer and then exposing selected areas through a photomask. A 2% poly(acrylic acid) solution was spun at 3000 rpm for 30 seconds and baked for 1 minute at 200^{o}C. The entire wafer was submerged in 0.5 M calcium chloride for 5 minutes, rinsed with 0.05 M calcium chloride, and rinsed with deionized water. The wafer was then baked again to dry. PEGDA prepolymer was spincoated on top of the poly(acrylic acid) layer at 1600 rpm for 30 seconds to produce thin layers or decreased to 250 rpm to form thicker layers comparable to those achieved by molding. Microgels were fabricated on spincoated wafers by exposing the wafers to 365 nm light through a photomask using a mask aligner. Wafers were then washed with 50 mM sodium chloride/55 mM sodium citrate to release the poly(acrylic acid) layer and collect the microgels in solution by pipetting. Microgels were centrifuged and suspended in PBS. Unlike the PDMS method, spincoating the prepolymer eliminates the need for molding and plasma treatment steps, and therefore speeds the fabrication process. Additionally, whereas the PDMS molds have a fixed height and so require a separate master wafer for each height, spincoating directly onto a wafer allows the height to be varied while keeping the mask constant.

3.1.4 Alternative Fabrication Chemistries

Microhydrogel fabrication was attempted from additional materials as well to test the suitability of a variety of biomaterials commonly used in TE studies. Tested materials were collagen, gelatin, alginate, and poly(vinyl alcohol). Several materials were also tested for their suitability to replace PDMS as a molding material. These materials were agar, agarose, PEGDA, PNIPAAm-PEG, alginate, and gelatin. In all cases these molds were hydrogel materials and so molds were stored at 4^{o}C in a humidified environment.

3.1.4.1 Collagen

Collagen was prepared from a liquid solution of 3 mg/mL, diluted to 2.4 mg/mL, neutralized with NaOH, sealed into the mold, and allowed to gel at 37^{o}C in an incubator.

3.1.4.1 Gelatin

Gelatin was dissolved at 20%(wt/v) in distilled water using heat to fully dissolve the polymer. This same solution was used for molds and microhydrogels (in separate experiments). For microhydrogels, the gelatin was added to PDMS molds, sealed and cooled to room temperature. For molds, the gelatin was poured over silicon wafers and cooled to room temperature.

3.1.4.2 Alginate

Alginate was dissolved in 150 mM NaCl at 1.2-4.0%(wt/v) concentration and spread across the surface of the PDMS molds. A straight edge was then used to remove excess polymer solution before the microhydrogels were cured using an agar block containing 0.5 M $CaCl_2$.

3.1.4.3 Poly(vinyl alcohol)

PVA was dissolved at 12%(wt/v) in distilled water using a stir plate and heating . Once the polymer was fully dissolved, it was cooled to approximately 50^{o}C and added to PDMS mold surfaces. The mold was sealed with an untreated glass coverslip and a weight was put on top to maintain pressure. This was allowed to sit at room temperature for 36 hours. Coverslips were removed, placed in petri dishes, and placed on an agitation plate. Na_2SO_4 was dissolved at a concentration of 0.5 M and added to the petri dish. The agitation plate was then set to 70 rpm.

3.1.4.4 Mold materials

Agar was dissolved at 10%(wt/v) in distilled water with heating as necessary and poured over silicon wafers. Agarose was dissolved at 10%(wt/v) in distilled water, heated to dissolve, poured over wafers, and allowed to cool. PEGDA (MW575) was mixed with distilled water at a high concentration with photoinitiator, pipetted over wafers, and crosslinked using UV light. A PNIPAAm-PEG flask was purchased from Mebiol and rehydrated with 5 mL distilled water (50% the recommended volume), refrigerated until use, and gelled at 37^{o}C in an incubator. Alginate was dissolved at 4%(wt/v) in 150 mM NaCl, poured over silicon wafers, and cured using an agar block containing 0.5 M $CaCl_2$ that was suspended with spacers to set the thickness of the mold.

3.1.5 ISX experimental conditions

Microgels were suspended in 200 µL of PBS in 1.5 mL Eppendorf tubes, this volume could be increased or decreased depending on the number of microhydrogels. Samples were run on an ISX flow cytometer at the slowest fluidics setting to minimize tumbling and blurred edges, and different magnifications were tested. The three sizes (20, 40, and

60 μm - length of the longest side) are distinguishable with the 20x magnification on the ISX. The smallest shapes tested here (20 μm maximum length in cross-section) were best viewed on the 60x magnification however, the tubing allowed for microparticles as wide as 100 μm to be imaged using the 20x magnification. The ISX confirms that there is not excessive shear force on the microparticles and that the microparticles arrive at the interrogation point intact. Given the relatively high stiffness of the microparticles analyzed in this study, this should be checked for each subsequent material.

3.1.6 IDEAS analysis and sorting protocol

Images with desirable orientation relative to the camera were gated by graphing Area vs. Aspect Ratio and collecting the events with sufficient size (>100 A.U.) for a microhydrogel and a high aspect ratio (> 0.5). Microparticles tilted relative to the camera would not be distinguishable by shape and were discarded during collection based on low aspect ratio. There were few images showing more than one shape passing the interrogation point at the same time ("doublets"), these occurred primarily in the beginning of the analysis period and were eliminated during analysis. Some cross-contamination was detected between sample runs (slightly decreasing the calculated accuracies for the test dataset) and is estimated by the manufacturer at <0.5% carryover during use of the AutoSampler.

To determine the total number of possible multiplexed barcodes, shape, size, and fluorescence were considered separately in the context of the ImageStreamX. A training population of at minimum 25 images was defined by eye for each of the twelve tested SSF barcodes (20, 40, and 60 μm lengths for square, circle, equilateral triangle, and right triangle). Gating parameters were chosen based on the "Find Features" wizard in IDEAS (Image Data Exploration and Analysis Software) which compares two true populations

and reports the image features which give the greatest separation between the two groups. Similar to traditional gating in a non-imaging flow cytometer, data could be plotted according to these parameters and gated in order to apply another set of parameters that further define the data. Based on feature comparisons, six features defined by IDEAS (Aspect Ratio, LobeCount, Symmetry2, Symmetry3, Symmetry4, and Circularity) were selected as the most effective at distinguishing shape. A seventh feature, Area, was selected to separate sizes within a shape population.

3.2 Results

3.2.1 PDMS Molding is high-throughput and microhydrogels have low size dispersity

3.2.1.1 Molding enables high-throughput fabrication and collection of microhydrogels

High "n" was achieved by using arrays of $>10^4$ molds per 2 µL of precursor; tens of thousands of replicate microgels were produced and harvested. Macromer solution was optimized by tweaking polymer weight percentage, photoinitiator concentration, UV intensity and exposure time, and accelerator concentration (**Figure 16**). For each starting volume of 2 µL of prepolymer, the average number of collected microgels was ~3,500. When scaled to a 20 µL starting volume, this number of microgels jumped to ~49,200, showing that collection efficiency was slightly higher with higher areas since mold edges were left empty to prevent film formation. It is important that the replicate number be far in excess of the stated goal of 1000 due to expected losses during fluid handling as well as the proportion of microhydrogels that are appropriately rotated during ISX testing. This number could be increased further still by using standard sized silicon wafers as substrates for crosslinking spincoated macromer solution (**Figure 17**). The estimated number of microhydrogels that could be made for a range of sizes are compared for glass

slides and wafers in **Table 3**. Microhydrogels were filtered through 100 µm cell strainers before ISX analysis for all conditions in this dissertation to remove any microhydrogels linked by a layer of polymer.

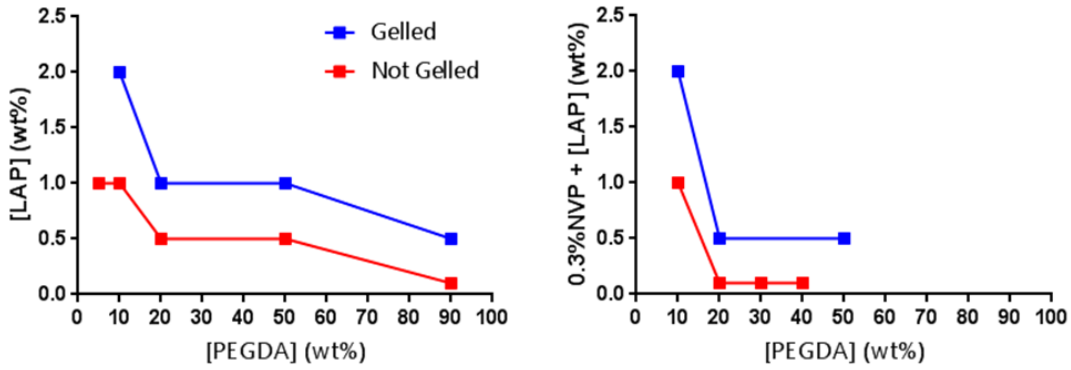

Figure 16 Dependence of Polymerization on Macromer Concentration
As macromer concentration and photoinitiator concentration increases, microhydrogels form more easily (left). Adding accelerant will lead to polymerization at lower concentrations of both (right).

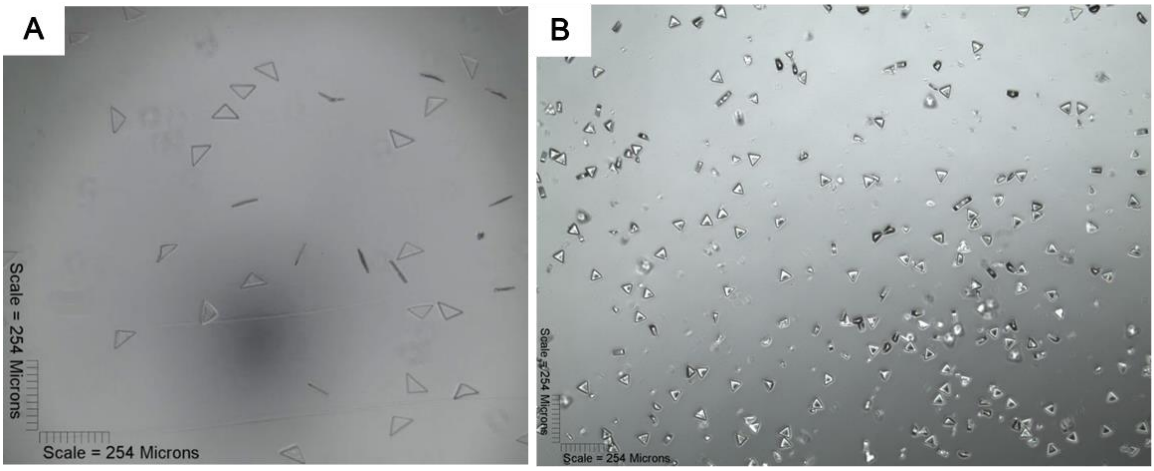

Figure 17 Spincoated Microhydrogels
Microhydrogels could be generated via spincoating with the speed of the spin (A – fast, B – slow) controlling the thickness of the resulting microhydrogels. Scale bars are 254 µm.

Table 3 Potential Microhydrogel Numbers
The number of microhydrogels that can be obtained from a mold depends on both feature and substrate size.

Mold Type	Array Area (μm²)	Microhydrogel Unit Dimension (μm)	Microhydrogel Mold Area (μm²)	Replicate Number
Test 1.5 cm Array	$2.25*10^8$	20	900	250,000
		40	2500	90,000
		60	4900	45,918
10 cm Wafer	$78.54*10^8$	20	900	8,726,666
		40	2500	3,141,600
		60	4900	1,602,857

3.2.1.2 Molding leads to low size dispersity in microhydrogels

Molds were filled with 10-20 μL of prepolymer depending on the size of the array and crosslinked. A mold was hydrated and imaged using a phase-contrast microscope (**Figure 18**). This shows how the aqueous media swells the hydrogel matrix. In this mold, the height of the microhydrogel is greatly exceeded by the cross-sectional area dimensions, causing the swelling action to release the microhydrogels from the mold. Some formulations with either lower swelling ratio or deeper mold faces require gentle agitation with a pipette tip or spatula to collect the microhydrogels in suspension.

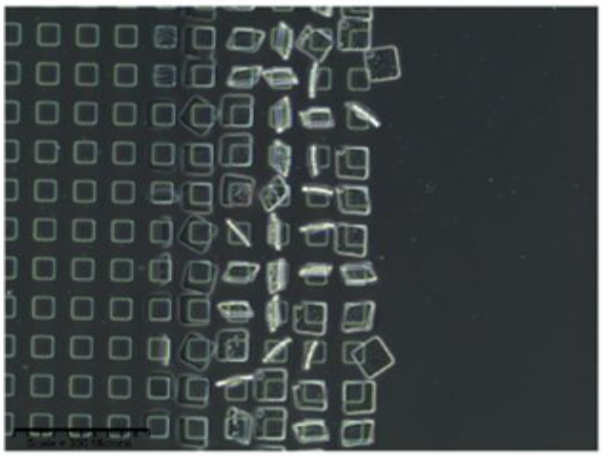

Figure 18 Molded Microhydrogels
Microhydrogels will swell upon exposure to aqueous media and this swelling action enables collection of suspended microhydrogels using pipettes. Scale bar is 300 μm.

3.2.2 Alternative Fabrication Chemistries

Microhydrogels were successfully fabricated from alginate, gelatin, and PVA. Collagen was unsuccessful because even at high concentrations the material was too weak and sticky to form cohesive microhydrogels that could be collected in solution (not shown). Gelatin was then tested as an alternative and found to form microhydrogels that could be collected, however, this material had a higher swelling ratio than the PEGDA used previously. As a result, the gelatin microhydrogels were larger than feasible for ISX analysis and also had low contrast ratio that makes them difficult to image (**Figure 19**). The alginate was the most successful as the microhydrogels had high shape fidelity (**Figure 20**); however over long time periods these microhydrogels seemed to aggregate irreversibly. The PVA required a fabrication process that is not compatible with cells and so was not considered (**Figure 21**).

Molds could also be fabricated from different biomaterials (not shown). However, none of these chemistries were as favorable as the PDMS molding material. Primarily this was because the tested materials are also hydrogels with relatively high swelling ratios compared to the tested PEGDA microhydrogel material. The non-PDMS materials were attractive because they are naturally hydrophilic and would not need plasma activation before use. However, this also meant that the molds had a mesh size on the order of the monomer and so the monomer could diffuse from the cavities in the mold into the surrounding material. Then after crosslinking, the system had formed an interpenetrating network rather than individual microhydrogels. Additionally, the swelling ratio of the hydrogel molding materials caused the mold to deform such that the cavities in the mold were distorted compared to the photoresist design. Finally, as these molds were hydrogel materials, storage was more difficult as they required a humidified atmosphere and were not as mechanically robust.

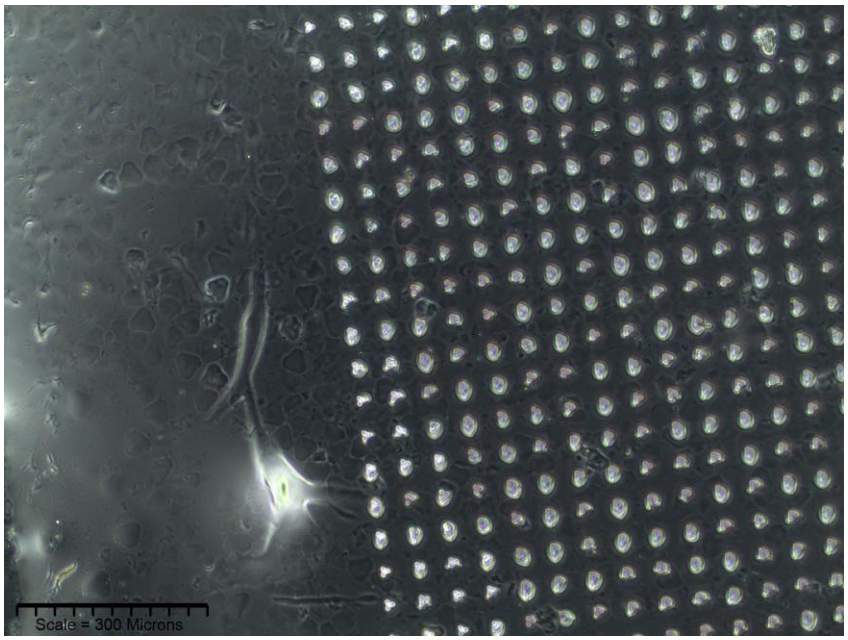

Figure 19 Gelatin Microhydrogels
Gelatin microhydrogels swell significantly when hydrated. Here, a molded surface of small equilateral triangles is shown on the right-hand half of the image and the microhydrogels have floated off to the left. These microhydrogels are much larger than the mold area and have low contrast. Scale bar is 300 μm.

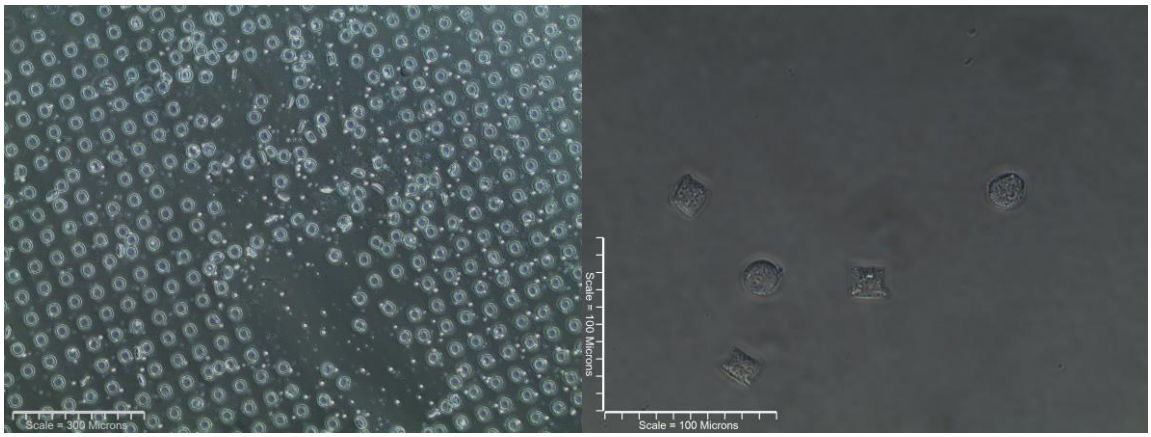

Figure 20 Alginate Microhydrogels
Microhydrogels (left image, large circles) were fabricated from 4%(wt/v) alginate that was cured in the mold and collected with PVA on a coverslip. These microhydrogels were fabricated with fluorescent microparticles to aid with visualization (small circles). In a separate experiment, 3%(wt/v) alginate microhydrogels were fabricated with fluorescent nanoparticles (right image). Scale bar is 300 μm (left) and 100 μm (right).

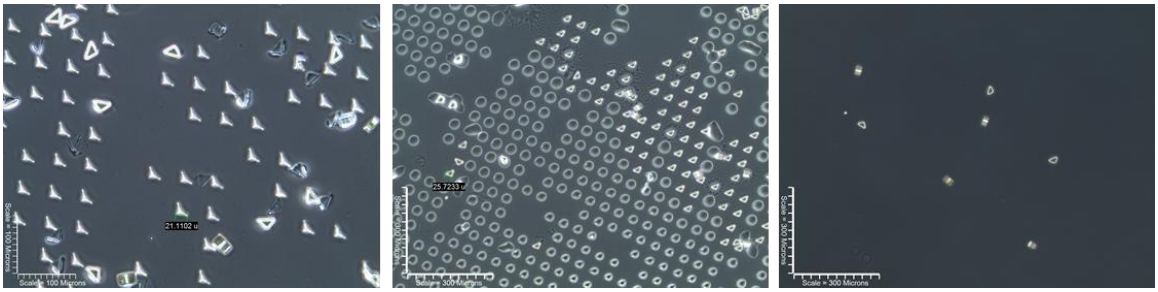

Figure 21 Poly(vinyl alcohol) Microhydrogels
Microhydrogels were imaged on the surface of the coverslips before the salt solution was added (left) and after they had been incubated in the salt solution for 24 hours (middle). These microhydrogels could also be scraped off the surface of the coverslip and handled in solution (right). Scale bars are 100 µm (left) and 300 µm (middle, right).

3.2.3 Microhydrogel analysis flowrate can be maximized

Samples in PBS were run for approximately five minutes each; longer time periods were less productive because the microparticles began to settle. This reduces the throughput of the system and also biases the collected images towards constructs with lower density. To increase the settling time of the microhydrogels, solutions of varying amounts of PBS and glycerol were tested. The glycerol is added to increase the solution density. However, the density could not be increased to the point where microhydrogels would not settle for three reasons: it may affect flow in the ISX, image quality is reduced if the refractive index of the sample and sheath fluid are too disparate, and centrifugation is used for all microhydrogel handling steps. A mixture of 50% PBS and 50% glycerol by volume was selected based on the settling time which increased to greater than 15 minutes.

The concentration of microhydrogels was varied to determine the maximum flowrate that could be imaged by the ISX. While the manufacturer states a maximum image collection rate of up to 5,000 events/second, this assumes that the machine is run on the highest fluidics setting and that the events consist of cells. Instead, it was found that microhydrogels could be imaged at a maximum rate of ~70 microhydrogels/second, most

likely due to their larger volume. This maximum was reached at a starting microhydrogel concentration of ~3500 microhydrogels/µL (**Figure 22**). After this maximum was reached, the flowrate quickly dropped to minimal levels, possibly at the higher concentration it was difficult for the sip to collect microhydrogels for analysis.

However, use of this glycerol solution was discontinued because it resulted in high microhydrogel carry-over between samples. This was likely due to settling in the flow cytometer sample chamber or poor ability to rinse the chamber completely. Instead, PVA was used as an alternative density-increasing agent and dissolved at 2%(wt/v) into distilled water containing 0.1%(v/v) Tween-20. This solution has a higher density than water and the surfactant reduced microhydrogel adhesion to plastics at all stages of handling. The ISX was pulsed at high speed to maintain a high rate of microhydrogels while imaging at the low flow speed. The combination of the lower density and the surfactant resulted in few microhydrogels seen in rinse buffer between samples.

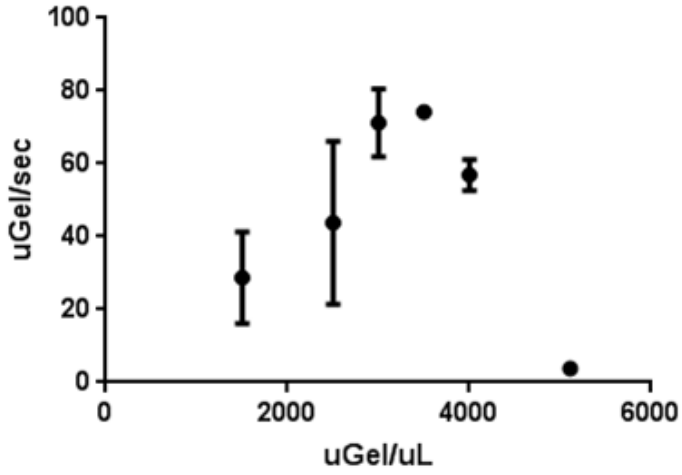

Figure 22 Flow Rates of Glycerol-suspended Microhydrogels
The number of microhydrogels that could be assayed per second in the flow cytometer increases with concentration until the microhydrogels begin to clog at the inlet of the flow cytometer.

3.2.4 Size, shape, and fluorescence barcodes are feasible

3.2.4.1 Size, shape, and fluorescence barcodes are discernable by ISX

Representative brightfield images collected by the ISX for each of the test barcodes are shown (**Figure 23**). The pre-defined shape and size barcodes are clearly identifiable in collected images and undesirable images were discarded based on area and aspect ratio. To quantify the barcodes computationally, masks were drawn on the brightfield images and greater than 75 features calculated for each image (**Figure 24**). To further increase the degree of multiplexing, fluorescent dyes visible in up to ten different channels (the maximum of the ISX) were added to the prepolymer (**Figure 25**). Microhydrogels were tagged in various fluorescent combinations to demonstrate, as proof of concept, six possible codes that could be layered with the shape/size barcode.

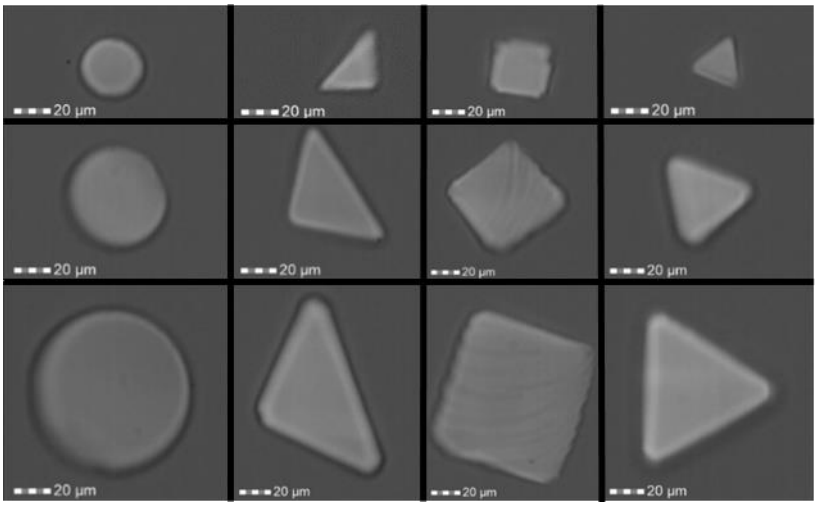

Figure 23 Ideal Examples of Oriented Microhydrogels
When microhydrogels are oriented ideally relative to the camera, clear images can be collected and the barcode is discernable by eye.

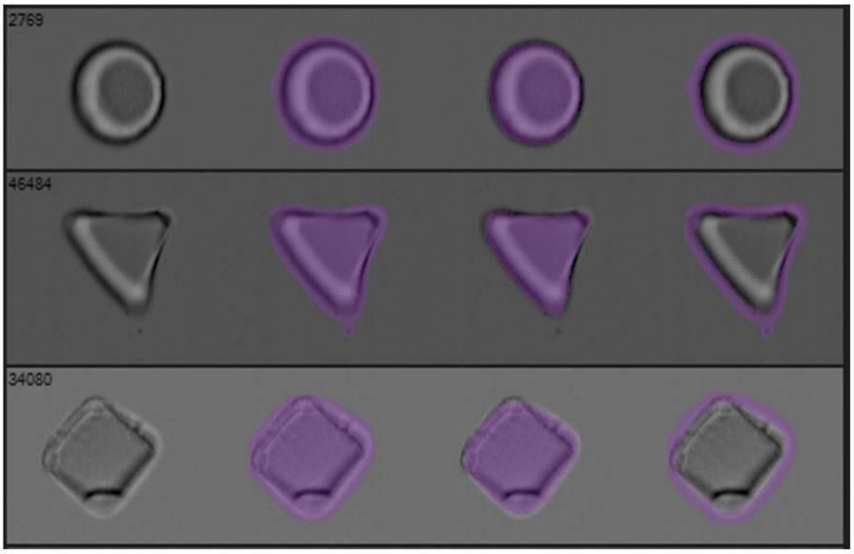

Figure 24 Masking in IDEAS
IDEAS allows user-designed masks to define images in order to better capture key features. From left to right: Brightfield, Object Mask, user-defined Object Mask, user-defined Perimeter Mask.

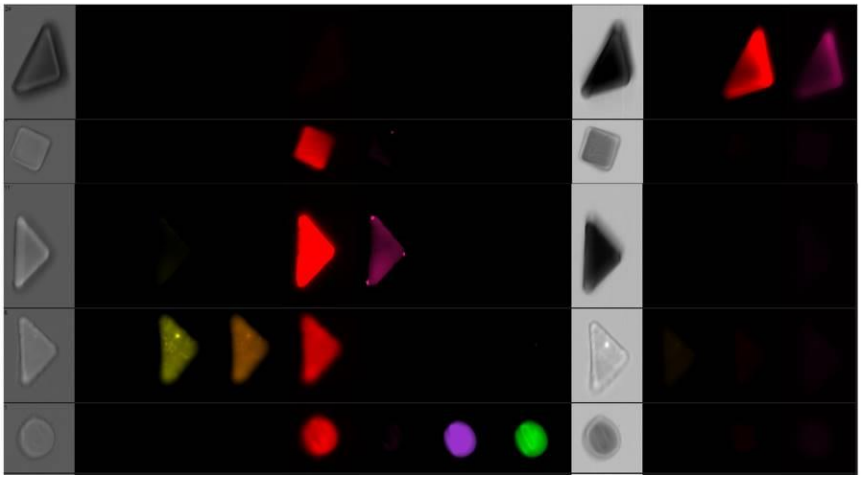

Figure 25 Fluorescence Barcodes
Fluorescent molecules were incorporated into the microhydrogels to show how shape, size, and fluorescence barcodes can be used orthogonally to achieve a large multiplexing.

3.2.4.2 Imaging parameters can be used to automate data analysis and distinguish barcodes with high accuracies

Data were analyzed using the IDEAS software (EMD Millipore) that is designed to analyze ImageStreamX data. An analysis template was defined based on microgels of known SSF barcode ("truth populations") and data collection rates were shown to be similar. Similar to traditional gating methods, data could be plotted according to user-chosen parameters, subpopulations identified, and the data further defined. For each shape, true subpopulations were compared to extract features which give the greatest separation between groups. Similar to the shape and size gating, fluorescence signatures could be quantified using several of the IDEAS values. From these measurements, the Area and Max Pixel Intensity variables were selected for the highest accuracy separation of the fluorescent barcodes.

An example comparison of two populations (squares and circles) is shown in **Figure 26** and gating of ideal images is shown in **Figure 27**. The identified features from all comparisons were then used to design a gating tree (**Figure 28**) to separate the populations and the marked ideal population was shown on scatterplots in order to draw manual gates around the regions of interest. The final gated populations are shown in **Figure 29**. This gating tree yielded twelve distinct populations as shown by the true images. The tree was then applied to the entire dataset and the percent accuracy was calculated for each true population by comparing the number of events sorted into the correct gate with the total number of events in any of the final gates. These accuracies are listed in **Table 4**. This template was applied to a test dataset of over 85,000 events and graphed. For each shape subpopulation, an area histogram shows three distinctly sized subpopulations gated such that the twelve barcodes are defined in the dataset. Using the described sorting scheme, ~9000 of the images were gated into one of the twelve final

populations. The IDEAS gating achieves an average accuracy of 82% for all twelve populations and an average of 88% for the 40 and 60 µm population.

Features	RD Mean (Sq,Cir)
Lobe Count_Morphology(M01,Ch01)_Ch01	2.44
Symmetry 4_Object(M01,Ch01,Tight)_Ch01	1.75
Circularity_Morphology(M01,Ch01)	1.37
Minor Axis_Object(M01,Ch01,Tight)	1.31
Major Axis_Object(M01,Ch01,Tight)	1.24
Diameter_Object(M01,Ch01,Tight)	1.21
H Variance Std_Morphology(M01,Ch01)_Ch01_5	1.14
H Correlation Std_Object(M01,Ch01,Tight)_Ch01_5	0.96
Median Pixel_M01_Ch01	0.83
Modulation_Object(M01,Ch01,Tight)_Ch01	0.81
Intensity_MC_Ch01	0.76
Mean Pixel_M01_Ch01	0.68
Delta Centroid XY_M01_Ch01_M01_Ch01_IntensityWeighte	0.01

Figure 26 Example Feature Identification
When comparing ideal circles and squares, IDEAS produced a list of potential features to separate the populations. Features are listed in order of declining utility.

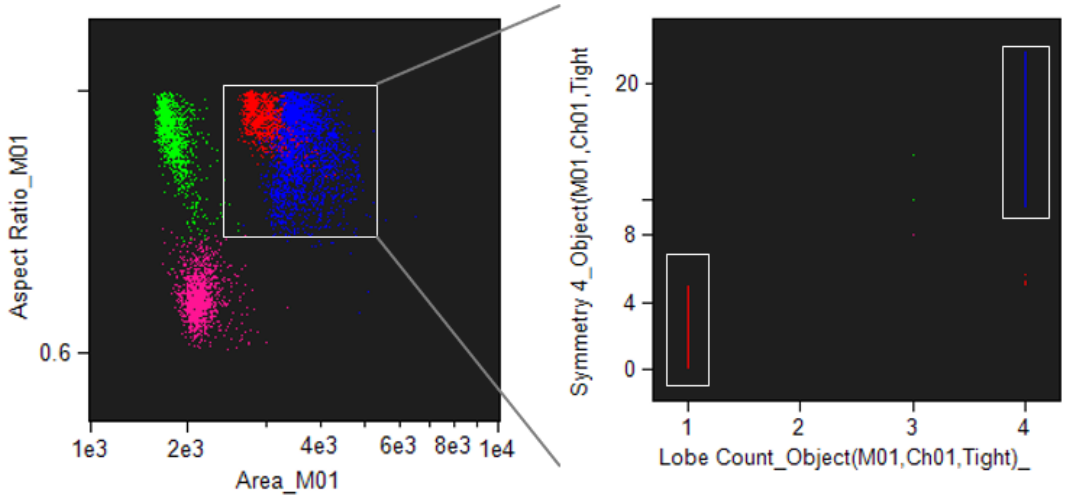

Figure 27 Example Gating Based on Identified Features
The left graph shows color-coded ideal populations of shapes where the circles (red) and squares (blue) overlap. By gating on these shapes and applying new axes of the identified features, clear separation could be achieved.

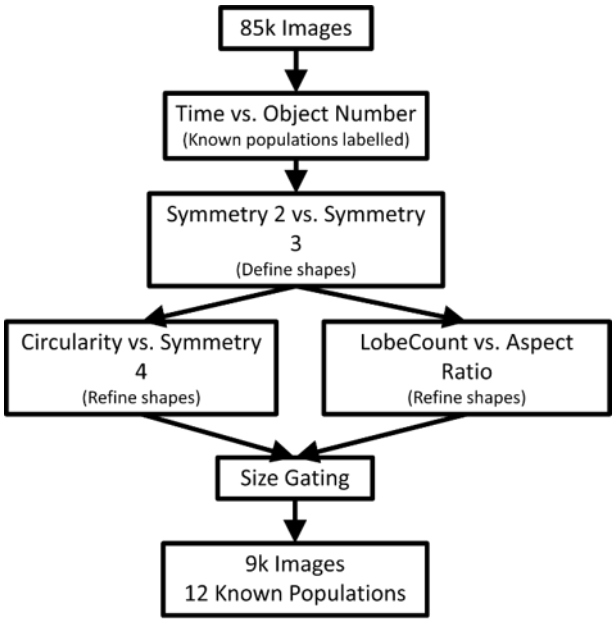

Figure 28 Gating Tree in IDEAS
Features were identified and applied in the described order to obtain final populations corresponding to the starting barcodes.

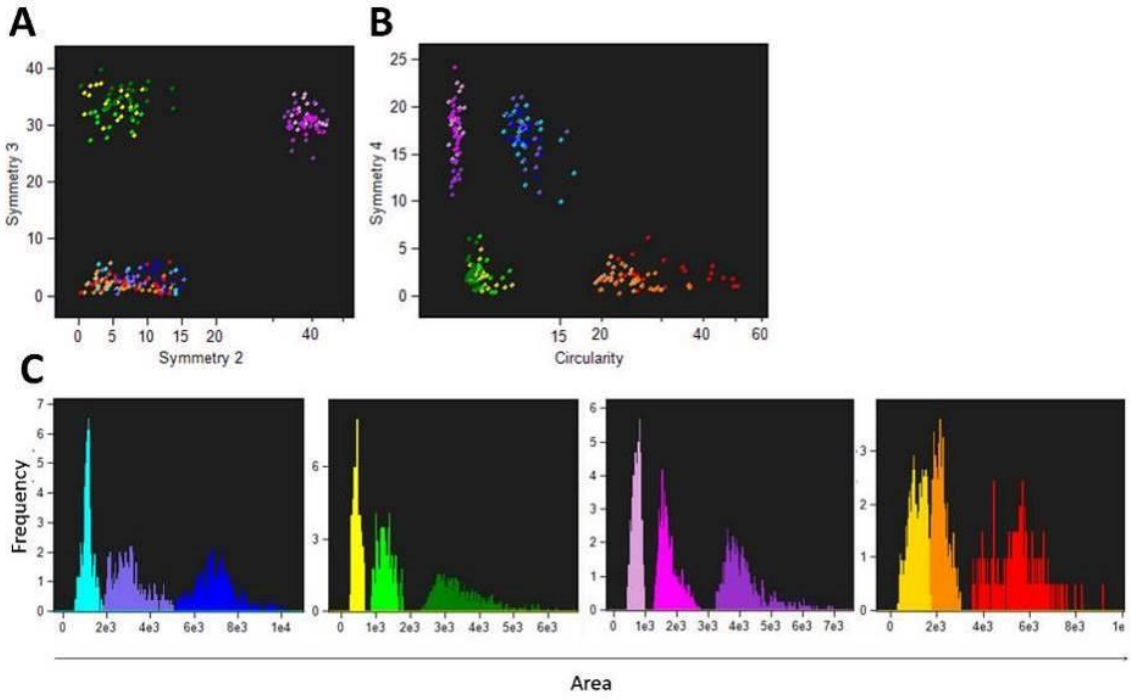

Figure 29 Final Populations
Two additional plots of identified features further separated the microhydrogels based on shape (A, B). The twelve final populations were then obtained (C). Blue – squares, green

– equilateral triangles, purple – right triangles, red – circles, sizes were color-coded with increasing size corresponding to darker colors.

Table 4 Accuracies from IDEAS
Each final gate was evaluated and the percentage of microhydrogels that constituted the true population compared to the number that were incorrectly sorted was reported as the accuracy.

Size (μm)	Circle	Right Triangle	Square	Triangle
20	41.38%	62.67%	86.97%	92.05%
40	80.88%	84.60%	75.91%	80.92%
60	94.61%	88.38%	97.89%	99.05%

3.3 Discussion

In 3DMaC, very high "n" is achieved by using thousands of cell-biomaterial micro-niches, fabricated using simple lithographic techniques, as input to the analysis method. Specifically, shape- and size-specific micro-hydrogels are created to mimic specific cellular microenvironments, e.g. to probe niche-dependent stem cell differentiation or tumor biology within the immune-microenvironment. We used microgel shape, size and fluorescence to uniquely barcode each cell-biomaterial niche. This barcoding is a unique aspect of 3DMaC and the use of niche-shape as a novel barcoding variable increases the multiplexing capability of this method many times higher than current analytical approaches. Although the micro-niches in this study are demonstrated using poly(ethylene glycol)-based materials, many other materials have been used in similar microhydrogel schemes and could be used with 3DMaC. Some of these potential materials were tested in this Aim, in particular the alginate microhydrogels seemed promising. In addition, rapid and high-throughput analyses of barcoded cell-biomaterial

microgels is enabled in 3DMaC through the use of imaging flow cytometry and multi-parametric data analytics which dramatically increases the quantity and quality of data collection compared to existing methods of analyzing 3D cell-material constructs.

Using the 3DMaC barcoding and analysis method, greater than 85,000 events were collected and gated with high accuracies into the constituent twelve test barcodes of shape and size. Based on the sensitivity of the ISX to SSF barcoding, the estimated number of barcodes available would be greater than 300 (**Table 2**). By using the 10 fluorescent channels in combination, a theoretical 2^{10} fluorescent barcoding indices are possible with the application of established compensation protocols[182], which would potentially expand the number of barcodes significantly. However, a more reasonable estimate is the 500 combinations already demonstrated by the commercially-available Luminex system.

As in traditional flow cytometry gating schemes, a balance is struck between accuracy and throughput; generally, one route is chosen depending on the needs of the experiment. Given that protocols exist for the fabrication of microhydrogels, the feasibility of our new method hinges on 3DMaC's ability to co-opt the flow cytometers to biomaterial studies. The ISX presents the additional challenge of learning to gate populations on spatial variables as opposed to traditional flow cytometry gating schemes based on fluorescence. The nature of the data collected by the ISX requires specialized analysis software (IDEAS) that can marry the gating most users are familiar with to the new range of parameters being calculated from the images taken in each fluorescent channel. While IDEAS offers a myriad of variables with which to sort as well as assistance selecting parameters that do not intuitively seem useful, the software was designed around cellular analysis and not the detection of sharp corners or overall shape.

By combining all samples into a pooled population, both material- and cell-based variables should be better standardized to reduce variation between experimental conditions. Already this Aim has shown that 3DMaC collects enough individual replicates to produce data with high statistical power for each biomaterial of interest. Once designed, this sorting template can be applied directly to new datasets for automated identification of barcoded populations similar to traditional flow cytometry. Therefore, IDEAS-based analysis is scalable with regards to dataset size, and a single experiment could be performed and analyzed within a single day.

Most excitingly, existing non-imaging flow cytometers have the ability to physically sort microparticles (FACS, fluorescence activated cell sorting) based on user-designed gating schemes such that individual events are separated out of the population and collected for further manipulation and analysis. Notably, the same SSF barcoding could be expanded further[183, 184] to non-imaging flow cytometers which are more widely available, have more fluorescent color channels, and can physically sort populations of interest. Biomaterials screening could then be applied to translational work as encapsulated cells are cultured, analyzed, and then only the highest performing constructs selected for implantation. As imaging flow cytometer technology continues to improve[185] and as imaging flow cytometers enter wider circulation, the 3DMaC method could help answer many questions of interest in the biomaterials community.

In its current iteration, there are still areas of this technology that would benefit from future work; these include the sorting accuracy, sorting throughput, and gating flexibility. Currently the accuracy of the sorting template developed for ISX analysis is predominantly limited by the fabrication process, not the IDEAS software. While the molding scheme for microhydrogel generation described in this aim produces particles

with low dimensional variability, there are inevitably some particles which are not perfectly formed. This generally means that the corners are not sharply defined and that the selected shapes (triangles and squares) appear more rounded. This causes the images to instead be sorted into gates intended for circles and is reflected in the data for supposedly circular objects. In future, this can be ameliorated by eliminating circles from the tested barcodes such that all such images can easily be removed from analysis.

This is related to the problem of sorting throughput, or the number of analyzed images which are gated into a final population for analysis. The majority of images are currently discarded because the shape has rotated in the θ direction and so the edges appeared blurred. Some of these images are easily classified by human eyes; however, this is more difficult for a computer. In the current analysis scheme, the accuracy of the gates has been valued over the throughput and so these images go ungated.

Two possible solutions are envisioned. First, an alternative form of image analysis could be used to classify a higher percentage of imperfect images. One such avenue is deep learning algorithms which could be trained on hundreds of thousands of true images and therefore "learn" how to classify a tilted shape with blurred edges. Current work by Dr Peng Qiu's group addresses this possibility. Alternatively, shape barcodes can be redesigned to favor image parameters that are easily calculated by IDEAS and less susceptible to rotation. For example, rectangular prisms (rods) with a square cross-section would likely align themselves parallel to the laminar flow to reduce tumbling and the square cross-section would ensure a relatively constant width measurement regardless of the θ orientation. Shape barcodes instead would depend on the length of the rod which trades multiplexing for increased accuracy.

Finally, there is the issue of "gating flexibility", meaning the ease by which new shape/size barcodes can be incorporated into the overall gating scheme. In the current scheme, the incorporation of new shapes involves: (1) identification of >25 ideal images of the new shape, (2) pairwise evaluation of principal components against all existing shapes, (3) alteration of the gating tree to include new variables, and (4) drawing of additional gates. These steps are lengthy and rely on the researcher to optimize. Fortunately, existing flow cytometry analysis techniques offer promising ways forward. Currently, there is a push towards computational gating, meaning that algorithms define the gating boundaries to collect statistically different subpopulations.[186] These methods rely on clustering techniques that evaluate all of the parameters for a certain event and draw scatterplots in which highly similar events are collocated in 2D space (See the work of Dr Peng Qiu and Jenny Jeong as to how this can be coupled to 3DMaC). These methods are computationally tasking but provides additional clarity to the user, are less subject to bias, and allows for easy addition of new shape barcodes.[186]

CHAPTER 4 Aim 2[3]

Demonstrate how 3DMaC can measure the differentiation of encapsulated cells in response to barcoded material compositions

This Aim has two broad goals: (1) to demonstrate how 3DMaC can measure mineralization in microhydrogels on the basis of material composition and (2) to differentiate MSCs into osteoblasts in microhydrogels with specific peptides covalently incorporated into the matrix. Whereas the first Aim established the basis of the SSF barcoding technique and outlined its technical strengths and limitations, this Aim details how to use 3DMaC to measure cell differentiation when encapsulated in a biomaterial. Key challenges overcome in this Aim included fabricating microhydrogels with high cell viability, avoiding spontaneous mineral deposition, and maintaining flow conditions for microhydrogels containing high density mineralized material.

MSCs were selected as the model cell type due to their widespread use in current clinical trials and osteogenic differentiation studies. The particular model system of osteogenic differentiation was chosen because osteogenic differentiation of MSCs is robust, can be induced by known media components, and results in detectable mineralized material. In this Aim, the potential of adipogenic differentiation was also explored, but osteogenesis

---

[3] Partially adapted from: Parratt, K.; Jeong, J.; Qiu, P.; Roy, K. 3D Material Cytometry (3DMaC): A Very High-replicate, High-throughput Analytical Method using Microfabricated, Shape-specific, Cell-material Niches. *Lab on a Chip*, 2017, 17, 2861-2872.

was selected. PEG remains the polymer base for the microhydrogel constructs however; short peptides were covalently incorporated to introduce biologically relevant signals to induce stem cell differentiation.

4.1 Methods

4.1.1 Materials

All cell research was performed according to institutional review board guidelines. The A20 B lymphoma cell line (A20s), human mesenchymal stem cells (hMSCs, RoosterBio), and mouse mesenchymal stem cells (D1) were used as model cell types. These hMSCs are a commercial product, deidentified before use, and therefore experiments are exempt from institutional review. hMSCs were cultured according to manufacturer's instructions and expanded twice before use. D1 cells were expanded in DMEM (Dulbecco's Modified Eagle Medium) supplemented with 10% FBS (fetal bovine serum) and 1% penicillin-streptomycin (Pen-Strep). Dendritic cells (DCs) were differentiated from bone marrow progenitor cells isolated from C57BL/6 mouse tibias and femurs then cultured for 7 days in RPMI media supplemented with 10% FBS, 1% penicillin-streptomycin, 100 mM sodium pyruvate, 1% non-essential amino acids, 0.1% 2-mercaptoethanol, 20 ng/mL GM-CSF, and 10 ng/mL IL-4. T cells were isolated from C57BL/6 mouse spleens using the MACS Pan T cell kit and used immediately. A20 cell-containing microhydrogels were cultured in RPMI media and stem cell-containing microhydrogels in DMEM media, both supplemented with 10% fetal bovine serum and 1% penicillin-streptomycin. Media was changed every two days. Cell-microgel constructs were maintained in a humidified incubator at 37^{o}C in 5% CO_2.

Cell-containing microgels consisted of 0-30% poly(ethylene glycol) diacrylate (MW 3400, Laysan Bio) and/or 0-10% 4-armed poly(ethylene glycol) thiol (PEG-4SH, MW 10kDa, Laysan Bio) and/or 0-30% 4-armed PEG norbornene (PEG-4NB, MW 10kDa, Sigma Aldrich) and/or 0-0.9%(wt/v) dithiothreitol (DTT, Molecular Probes). LAP was dissolved at 0.5-1%(wt/v) in DMEM with 0-0.3%(wt/v) NVP, aliquoted, frozen at -20^{o}C, and thawed before use. HEPES buffer was also included in some formulations (4-(2-hydroxyethyl)-1-piperazineethanesulfonic acid).

RGD peptide (H-CGGGGGGGGRGDSG-OH[101]) was purchased from CHI Scientific. HAVDI peptide (H-HAVDIGGGC-OH[107]) was purchased from GenScript. These were aliquoted for storage at -20^{o}C and dissolved directly in the photoinitiator solution and pH adjusted before use. Osteogenic media consisted of basal media supplemented with 100 nM dexamethasone, 50 mg/L ascorbic acid, and 10 mM beta glycerophosphate. Fixation buffer (PFA) consisted of 16% paraformaldehyde solution that was diluted to 4% in PBS and used within two weeks. DAPI (4′,6-diamidino-2-phenylindole) was aliquoted at 5 mg/mL, frozen at -20^{o}C, thawed before use, and used at a concentration of 5 µg/mL. ISX running buffer consisted of distilled water supplemented with up to 0.1% Tween-20 and 2% PVA. Alizarin Red (AR) was dissolved at 2% in distilled water, the pH was adjusted to ~4.2, and the solution was filtered before use. Hydroxyapatite (Sigma Aldrich) had an average particle diameter of 5 µm.

4.1.2 Mineralization Masking via ISX

To develop a quantitative measure of mineralized area, hydroxyapatite was used as a proxy. These microparticles had an average diameter of 5 µm and would not dissolve in macromer solution. A high concentration of HA was suspended in 20% (wt/v) PEG-4NB + 0.6% (wt/v) DTT + 1% (wt/v) LAP in PBS and pipetted onto activated molds. The

solution was crosslinked with UV light for 10 seconds and microhydrogels were collected in distilled water supplemented with Tween-20. Centrifugation was used between all washing steps to collect the microhydrogels at the bottom of the tube. Cell-friendly centrifugation speeds were used (up to 700xg, generally for 5-10 minutes). The supernatant was then tested by removing 100 µL of water from the well and adding it to a 500 µL Eppendorf tube containing 100 µL of Alizarin Red solution. The tube was vortexed and checked under bright light to confirm that no particulate formed. Additional washing was performed as necessary until no particulate was seen. The microhydrogels were divided into two tubes; one tube remained unstained and the second tube was stained using AR. In the tube to be stained, the water was removed and Alizarin Red solution was added to cover the microhydrogel pellet. Microhydrogels were incubated at room temperature for 5 minutes then rinsed repeatedly with distilled water until supernatant was clear. Microscopic images were collected to confirm successful encapsulation and staining. These microhydrogels were then analyzed by the ISX and the brightfield channel was collected.

To develop a standard curve of mineralization, HA was suspended in macromer solution at the following concentrations: 0, 0.1, 1, 5, 20, and 50 mg/mL. Microhydrogels were then fabricated from each concentration, rinsed, stained, and rinsed repeatedly. The same shape of microhydrogel was used for all concentrations to standardize areas across the populations. Samples were suspended in 2% poly(vinyl alcohol) (MW 25kDa) with 0.1% Tween-20 in distilled water and images collected on the ISX. Images were masked with the developed template and absolute mineralization area was recorded. This was then divided by the area of the "system" mask to obtain the percentage mineralized area. The average and standard deviation were calculated for each population, and a linear fit was calculated. These are reported with an R-squared value for the average.

4.1.3 Cell viability and loading measurements

4.1.3.1 Cell Viability

Live/Dead staining was performed with a solution of 4 µM calcein AM and 4 µM ethidium homodimer III in PBS. Adherent cells were used as a live control and cells treated with 0.1% Saponin-O for 30 minutes were used as a dead control. ImageJ was used for cell viability and loading calculations. Constructs were cultured in 6-wellplates until free-floating cells adhered to the well and then microhydrogels were transferred to non-tissue culture-treated petri dishes.

4.1.3.2 Cell Loading

The number of cells incorporated into each microhydrogel depends on the initial cell concentration in the prepolymer, microparticle size, and cell size. Cell concentration ranged from high (10^7) and low (10^6) in the microhydrogels with a 60 µm diameter. Cell encapsulation was analyzed using a fluorescence confocal microscope and quantified using ImageJ.

4.1.3.3 Cell Labeling

Reactive oxygen species (ROS) staining was performed on hMSC-containing microhydrogels immediately after crosslinking. Microgels were rinsed with PBS and stained with 5 µM dihydrorhodamine 1,2,3 dye (DHR) for 30 minutes. This dye is oxidized in the cell and indicates the presence of ROS by green fluorescence in the mitochondria. A LionheartFX automated microscope was used to image microgels which had been formed as an array. Microhydrogels were also collected in suspension, stored on ice, and analysed using the ISX. The DHR was clearly visible in the second channel with a 488 nm laser setting of 20 mW. To measure the ROS activity quantitatively, two

additional features calculated by IDEAS ("Modulation" and "H Homogeneity Mean") were used to identify stained cells. A new gate was created to separate empty constructs from cell-containing constructs.

Antibody staining was performed on hMSC-containing microhydrogels which were fixed for 30 minutes with 4% paraformaldehyde immediately after crosslinking. Microgels were blocked with 0.5% BSA in PBS overnight, incubated overnight with DAPI and anti-humanCD105-PE in 0.5% BSA + 0.1% Triton-100, and rinsed for two hours in blocking buffer again. A Zeiss 700 laser scanning confocal fluorescence microscope was used to image microgels which had been formed as an array. Similar microhydrogels not formed as an array were then suspended in PBS and imaged using the ISX to confirm cell labeling could be seen in flow cytometry.

4.1.4 Osteogenic Differentiation of MSCs in 2D Culture

To validate the osteogenic differentiation of the hMSCs in 2D culture, cells were plated in four 6-well plates at a seeding density of 3000 cells per cm^2 in basal media. After cells reached 80% confluency, media was exchanged and half the wells remained in basal media and half were switched to osteogenic media. Cells were cultured for four weeks with media fully exchanged every 2-3 days. At the end of each week, a plate was removed from culture, washed 3x with PBS, and fixed in PFA for three hours at room temperature. Cells were washed again 3x with PBS then 2x with distilled water. The supernatant was then tested by removing 100 µL of water from the well and adding it to a 500 µL Eppendorf tube containing 100 µL of Alizarin Red solution. The tube was vortexed for 5 seconds and checked under bright light to confirm that no particulate formed. If necessary, additional washing was performed until no particulate was seen. Next, the water was removed from the wells and Alizarin Red solution was added to

cover the cells. Cells were incubated at room temperature for 5 minutes then rinsed repeatedly with distilled water until supernatant was clear. Microscope images were immediately collected.

4.1.5 Fabrication of Osteogenesis-inducing Microhydrogels

Macromer solution consisted of (1) 20%(wt/v) PEGDA3400 + 5%(wt/v) PEG-4NB + 5%(wt/v) PEG-4SH or (2) 30%(wt/v) PEG-4NB and 0.9%(wt/v) DTT or (3) 20%(wt/v) PEG-4NB and 0.6%(wt/v) DTT. Non-cell-containing microhydrogels were fabricated to determine crosslinking times (between 1 and 30 seconds). Cells were encapsulated in the microhydrogels at a low concentration, split into two equal portions, and cultured in basal or osteogenic media. RGD peptide was included in microhydrogels at 0 or 5 mM concentration. HAVDI peptide was included in microhydrogels at 0 or 1 mM concentration.

4.1.6 Measuring Mineralization in Cell-containing Microhydrogels

Microhydrogels were fabricated and cultured as described on pg. 88. At the end of culture, microhydrogels were collected, rinsed with PBS, and fixed with 4% PFA in PBS. After fixation, microhydrogels were rinsed multiple times with distilled water containing Tween-20 and stained with AR as described on pg. 87. Microhydrogels were then run on the ISX in PVA-supplemented wash buffer and mineralized area was calculated using the mask developed on pg. 84. Shape barcodes were determined using the sorting tree developed in pg. 72.

4.1.7 Alternative MSC Differentiation - Adipogenesis

Adipogenic differentiation was also tested as a potential model system. Cells were plated at high concentration (> 5000 cell/cm^2) and cultured in adipogenic media for two weeks. Media consisted of alpha MEM with 10% FBS, 1% Pen-strep, 500 nM dexamethasone, 0.5 µM isobutyl-methylxanthine, 1 µM insulin, and 60 µM indomethacin. After culture, cells were fixed with 4% PFA and stained with either Oil Red or anti-FABP antibody (R&D systems, AF3150). Some cells were also trypsinized before fixation and then fixed as a cell suspension instead. Half of this suspension was stained with Oil Red. These stained and unstained suspension cells were then assayed in a FlowSight imaging flow cytometer (this is a similar system to the ISX but with a smaller field of view, the Platt Lab at Georgia Institute of Technology kindly allowed use of this machine).

4.2 Results

4.2.1 Peptide sequences do not impact microhydrogel fabrication

For each of the peptide additions described on pg. 88, microhydrogels (without cells) were fabricated using the same processing conditions optimized for cell encapsulation. Images show that microhydrogels formed with different peptides did not negatively impact fabrication at the chosen concentrations (**Figure 30**). However, there is a small visual difference between the peptide-free microhydrogels and those containing peptide; the addition of a peptide seems to reduce the sharpness of the corners. This makes sense as the peptides will be occupying sites that could otherwise be used for crosslinking. There are also small differences between the sizes of the microhydrogels. It would be expected that adding peptide would result in less crosslinking and therefore higher swelling, but this was not directly measured (**Figure 31**). In the future, macromer

solution could be modified such that each condition has approximately the same crosslinking.

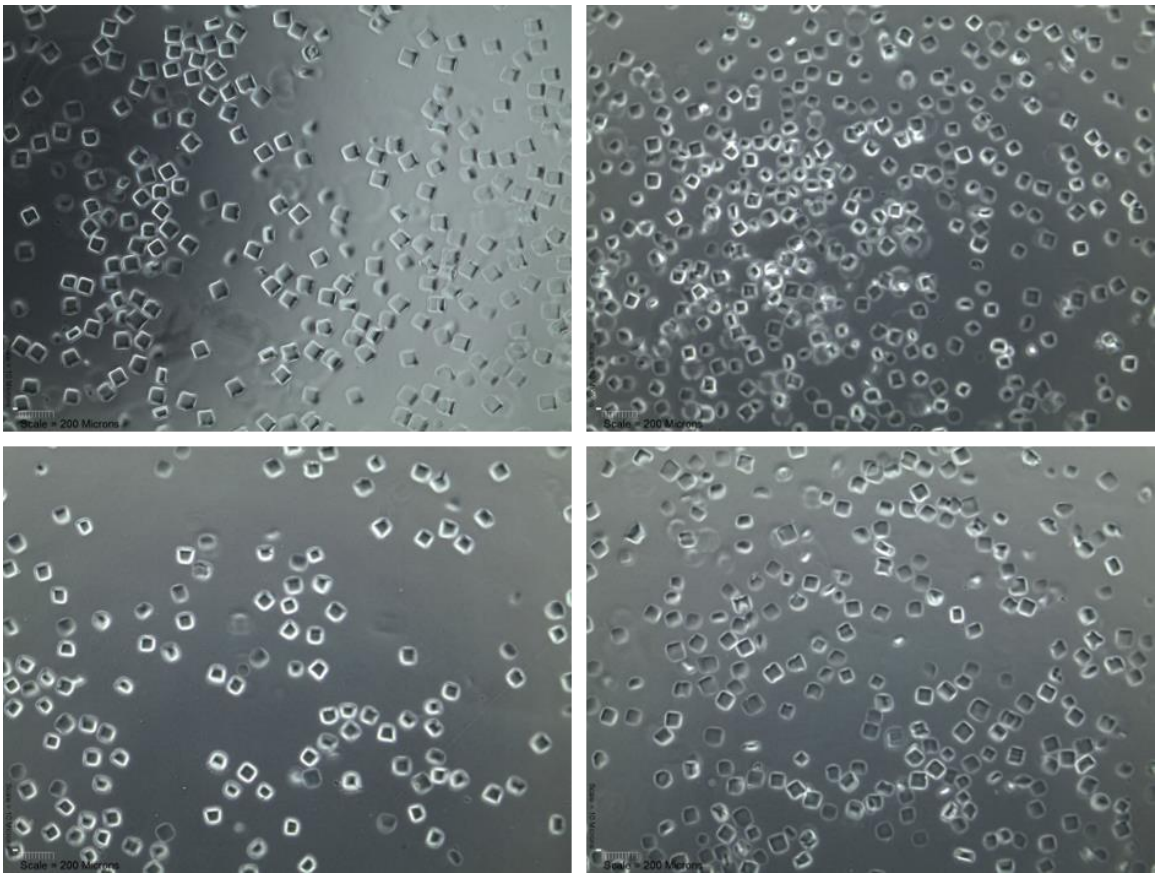

Figure 30 Comparison of Microhydrogels with Different Peptide Inclusions
The same barcode was fabricated from 20%(wt/v) 4-PEG-NB and 0.6%(wt/v) DTT containing no peptide (top left), 5 mM RGD (top right), 1 mM HAVDI (bottom left), and 5 mM RGD + 1 mM HAVDI (bottom right). The three images showing peptide-containing microhydrogels were modified with a 20% increase in brightness to standardize the images. Scale bars are 200 μm.

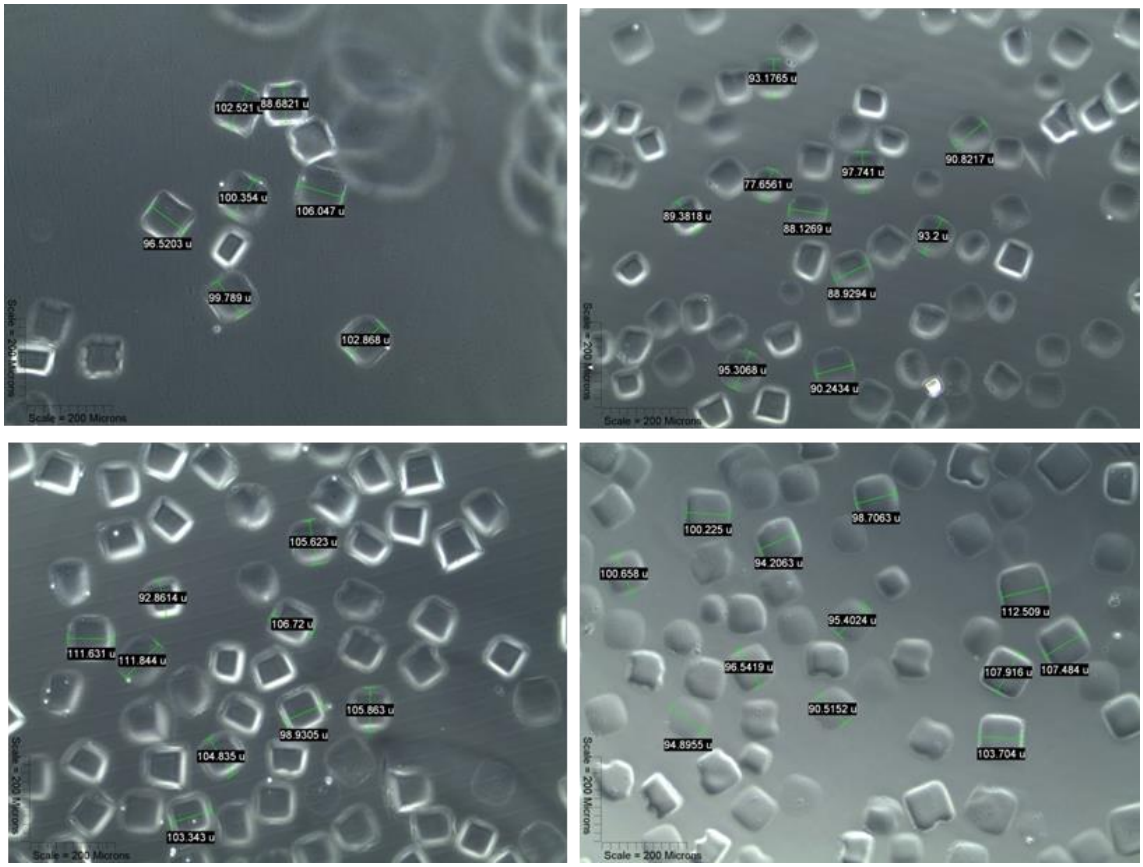

Figure 31 Quantified Comparison of Peptide-containing Microhydrogels
Peptide-containing microhydrogels were imaged on 10x magnification and measurements were taken of representative microhydrogels. Scale bars are 200 µm. From upper left moving clockwise, average sizes are 99.5, 90.5, 100.2, and 104.6 µm.

4.2.2 Quantification of mineralization in microhydrogels

Using hydroxyapatite as a proxy for mineralization, an IDEAS template was designed to measure mineralization in microhydrogels. In hydrogel scaffolds, mineralization is expected to be visible as nodules surrounding encapsulated cells and so hydroxyapatite microparticles are a model material. **Figure 32A** shows the microhydrogels immediately after fabrication. Inclusions of hydroxyapatite were easily distinguishable by eye. **Figure 32B** shows that these calcium-containing microparticles also stained strongly with AR as would be expected for deposited mineralization.

Using the ISX this mineralization was also visible. **Figure 33** shows representative bright-field images of microhydrogels that were unstained (left) and AR stained (right). Based on images collected from unstained microhydrogels, an analysis template was designed in IDEAS to mask the HA particles. Due to the "Intensity" value being very different for the clear regions and the hydroxyapatite inclusions, a mask was designed to measure the HA visible in Channel 1 by setting a minimum intensity of 830 for unstained microhydrogels. In the stained microhydrogels, the mineralized areas instead are visible as dark regions. This area was measured via an Intensity mask with a maximum value of 520.

Using the test dataset, the measured Intensity-masked areas were graphed (**Figure 34**). The Intensity mask on the brightfield channel gave the greatest separation between HA particles and blank hydrogel and was therefore chosen to measure mineralization. The mask was also refined to exclude any staining on the perimeter of the microhydrogel to eliminate artifacts derived from contrast, this was done using the AdaptiveErode tool in IDEAS set to 90% (**Figure 35**, **Figure 36**). The effect of this area reduction was quantified in **Figure 37**. A standard curve was developed to correlate the measured masked area with a quantitative measurement of mineralized material. Using microhydrogels from populations of known HA concentration (**Figure 38**), the following areas were masked for each population (**Figure 39**) and scaled by the area of the microhydrogel (**Figure 40**). These points could be quantified and fit to a standard curve (**Figure 41**).

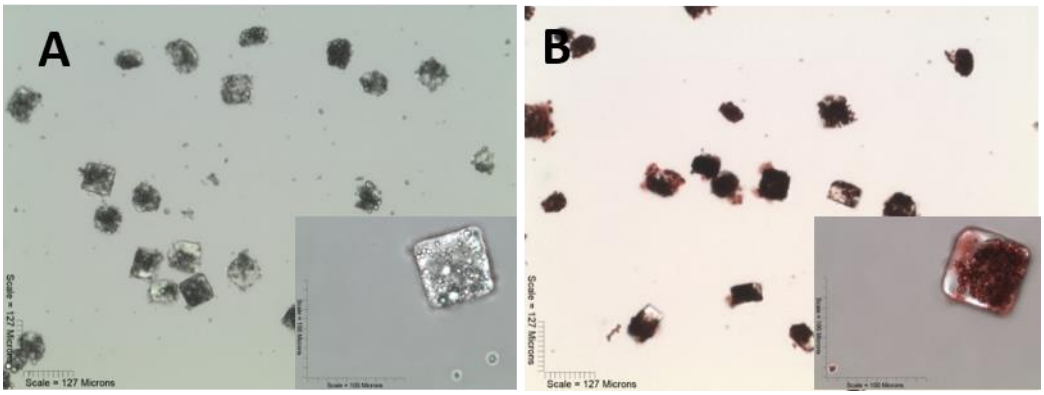

Figure 32 HA Particles as a Proxy for Mineralization
Hydroxyapatite was added to macromer solution and polymerized to show that inclusion does not reduce polymerization or interrupt shape barcoding. Unstained (A) and stained (B) samples are shown at 4x magnification and insets were taken at higher magnification. Scale bars are 127 µm (large images) and 100 µm (inset images).

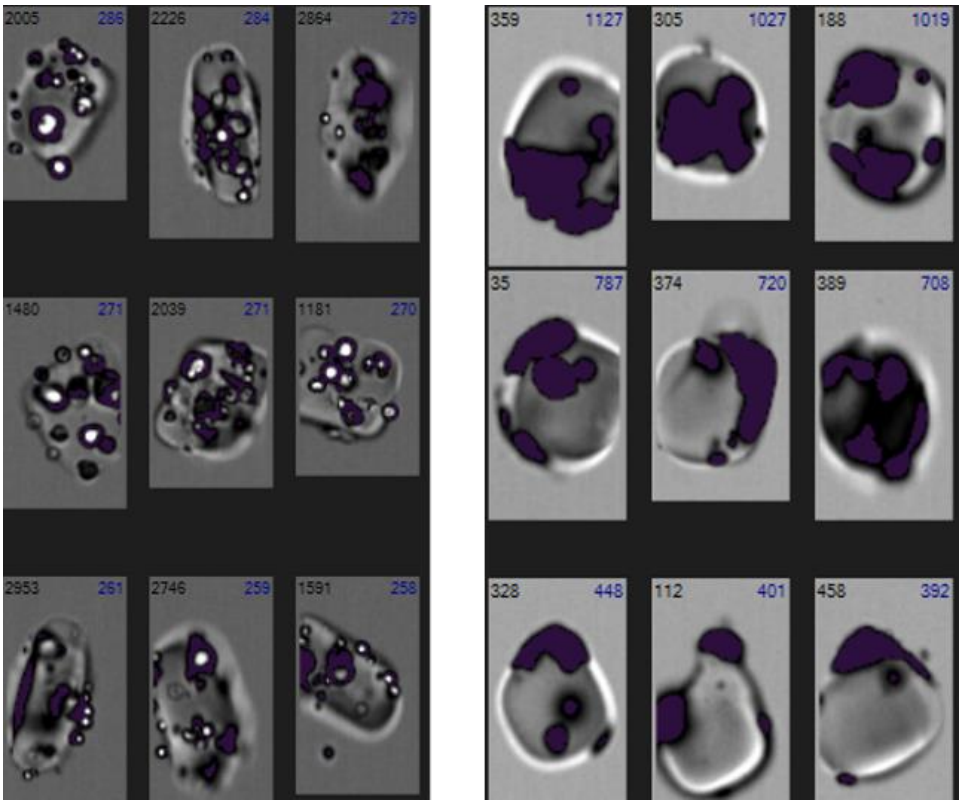

Figure 33 ISX Images of HA-containing Microhydrogels
Hydroxyapatite-containing microhydrogels were imaged in the brightfield channel of the ISX (left – unstained, right – stained). Masks were created for high and low intensity to mask in each channel, shown in purple, and these feature values are quantified in the upper right-hand corner of each image.

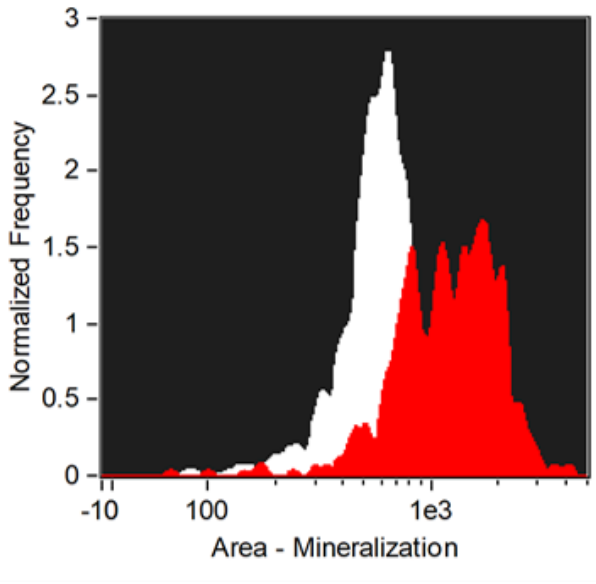

Figure 34 Masked Areas of HA in Unstained and Stained Microhydrogels
The masked area was quantified for unstained (white) and stained (red) samples and compared.

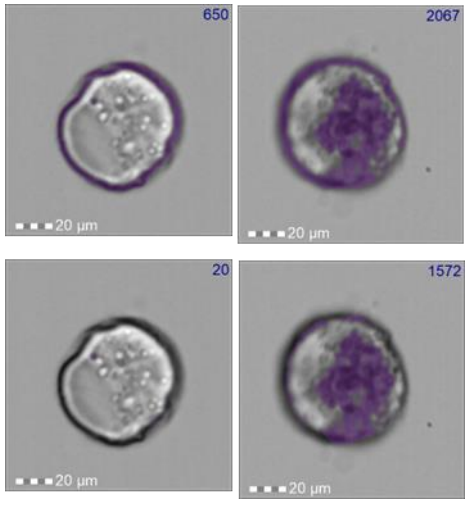

Figure 35 Demonstration of Edge Effects with Mineralization Masking
Edges of microhydrogels often have low intensity regions relative to the sheath fluid in unstained (top left) and stained (top right) microhydrogels. Once the edge is eroded from the mask, only mineralized areas are masked for both (unstained – lower left, stained – lower right). Values in images' upper righthand corner are for masked area.

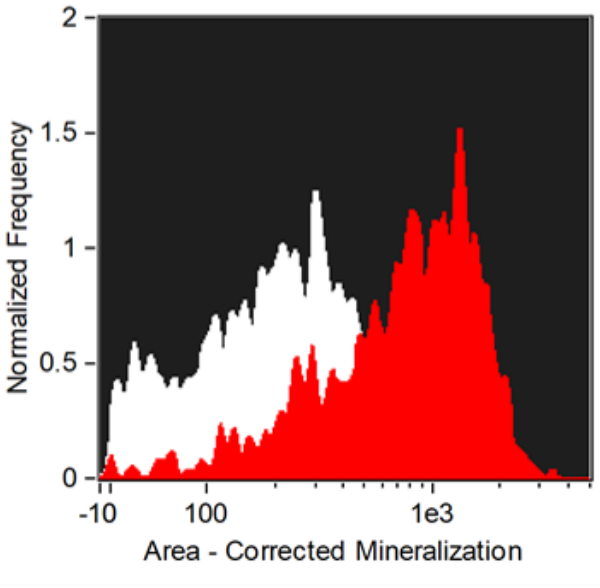

Figure 36 Quantification of Mineralization Refined to Remove Edge Effects
The mask was modified to eliminate the immediate edge of the microhydrogel from masking due to low intensity areas between the microhydrogel and sheath fluid.

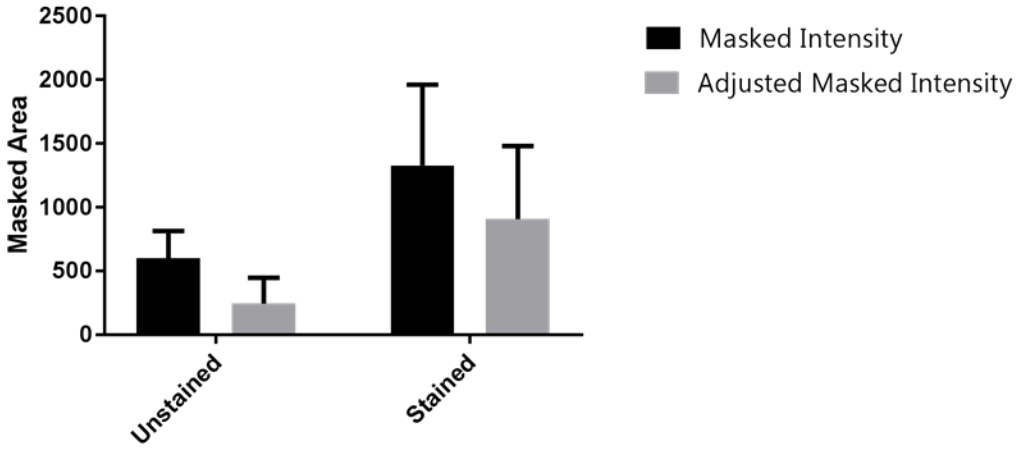

Figure 37 Graphical Comparison of Refined Masking Confirms Difference
By refining the masking of the HA-containing microhydrogels, the signal was reduced for unstained and stained populations. To test the comparison, an Ordinary two-way ANOVA was performed with Sidak's multiple comparison test. The row factor (unstained versus stained) was responsible for 37.18% of variability and the column factor (unadjusted or adjusted area) was responsible for 11.57%. The analysis was performed on 1242 unstained events and 552 stained events.

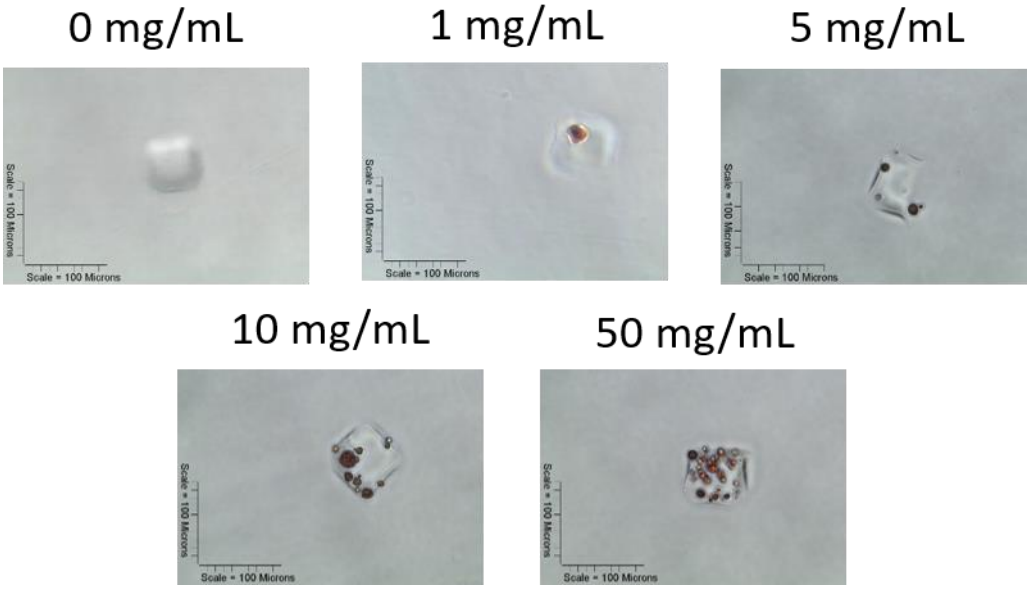

Figure 38 Hydroxyapatite Loading for Standard Curve
Representative images of microhydrogels loaded with different concentrations of hydroxyapatite. Note that some samples had brightness tuned to standardize the images but no changes were made to contrast or color. Scale bars are 100 µm.

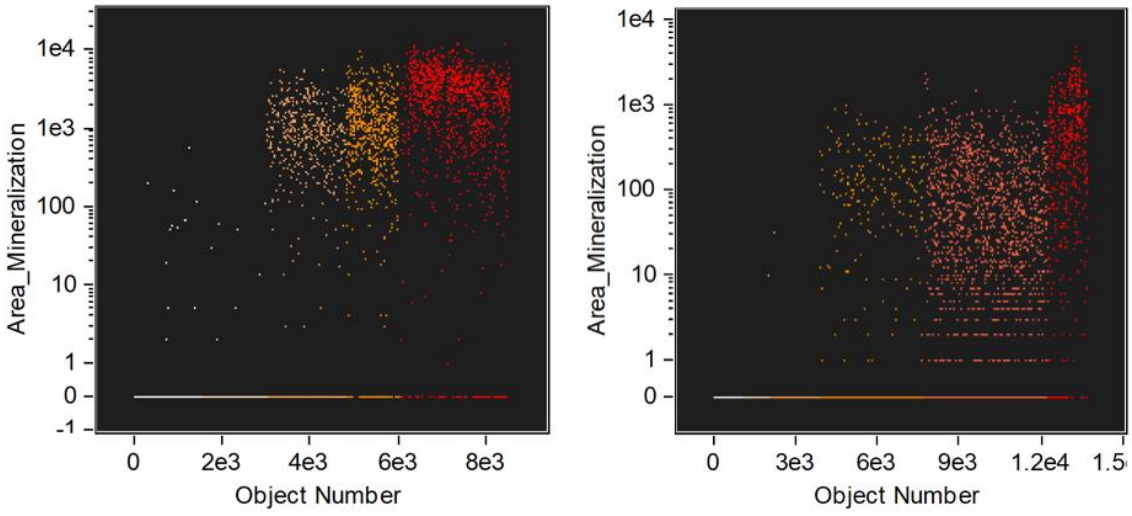

Figure 39 Area of Mineralization in HA Standard Curve
The absolute areas masked for each microhydrogel in two hydroxyapatite standard curves are shown (left – low contrast microhydrogels, right – high contrast microhydrogels).

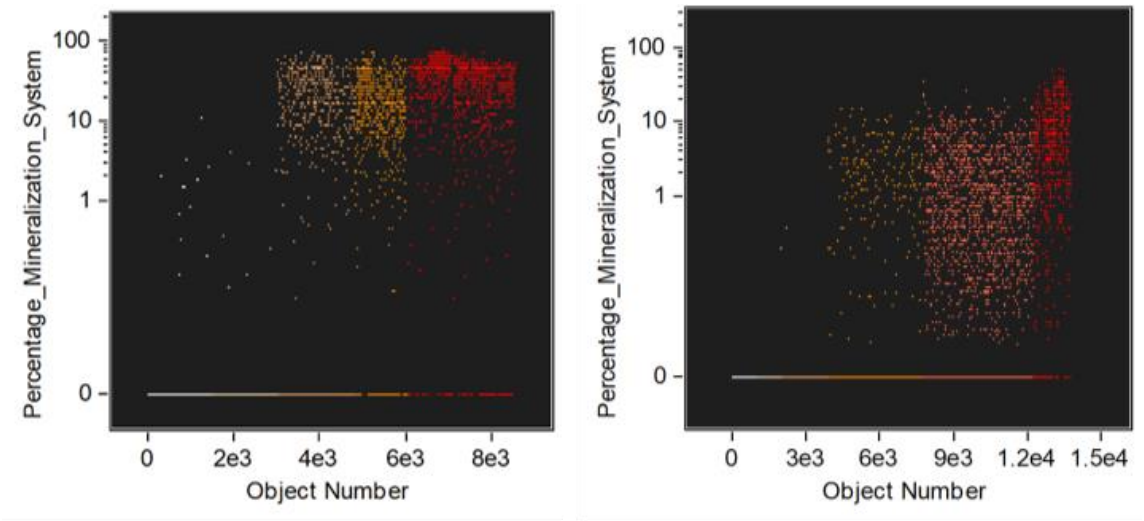

Figure 40 Percentage Mineralization in HA Standard Curve
The percentage of microhydrogel areas masked in two hydroxyapatite standard curves are shown (left – low contrast microhydrogels, right – high contrast microhydrogels).

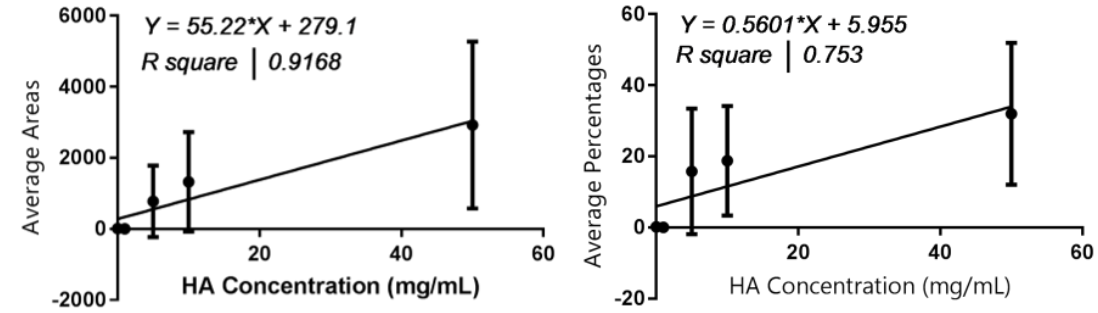

Figure 41 Lines of Best Fit for Mineralization Standard Curves
The areas shown in the above two graphs for the low contrast microhydrogels (left – absolute mineralized area, right – percentage mineralized area) were graphed and a linear fit was calculated. The equation of the line and R square values are shown.

4.2.3 Reducing Spontaneous Mineralization in Microhydrogels

Initially, a 30% (w/v) PEGDA3400 was used to encapsulate hMSCs for osteogenic differentiation. However, microhydrogels in osteogenic media rapidly (5-6 days) appeared cloudy or as though they contained fine-grained particulate (**Figure 42**). Staining with Alizarin Red (**Figure 43**) showed that this granularity was caused by

spontaneous mineralization which has been seen previously in osteogenic hydrogel materials.[187]

To reduce this mineralization, a hydrogel composition hypothesized to have a larger mesh size was tested based on literature suggesting that pore size contributes to autocalcification.[188-190] The 30% (w/v) PEGDA system with a macromer length of 3.4 kDa has a small mesh size, on the order of angstroms to nanometers. The new hydrogel formulation selected still maintains its PEG backbone but involved two key improvements. First, the mesh size was increased by using a longer PEG chain. Second, the acrylate chemistry was exchanged for a UV-activated norbornene-thiol reaction which is much quicker. Therefore, the new system is based on 20% (w/v) PEG-4NB and 0.6% (w/v) DTT (a molar equivalent of norbornene and thiol groups). High glucose DMEM was used as the solute as previous research from the Peyton group suggested it protects cell viability during maleimide-thiol crosslinking reactions that occur at lower pH.[191] HEPES buffer was included at a low concentration (0.1%(v/v)) to provide small buffering around the desired pH and NaOH was added as needed to neutralize the solution after the addition of peptides. The crosslinking time could then be reduced down to as low as one second, however, five seconds was selected to maintain shape fidelity without sacrificing high cell viability.

These microhydrogels did not auto-mineralize over the time period (two weeks) used in the following studies. **Figure 44** shows a comparison of microhydrogels fabricated from a PEGDA-based macromer (left) and a solution crosslinked by norbornene-thiol (right). Two key differences of these higher swelling microhydrogels are apparent; first that the edges and corners have swollen such that they are more difficult to discern, and second that the gels now show less contrast with the background when viewed with a phase

microscope. Over a ten day period, microhydrogels fabricated using the new and the old monomer formulations were cultured in basal or osteogenic media (**Figure 45**). The old formulation showed strong mineralization in osteogenic media and even some in basal media, whereas the new formulation showed none. In wells containing both formulations, the new PEG-4NB/DTT microhydrogels still showed no mineralization even when the PEGDA microhydrogels had strongly mineralized.

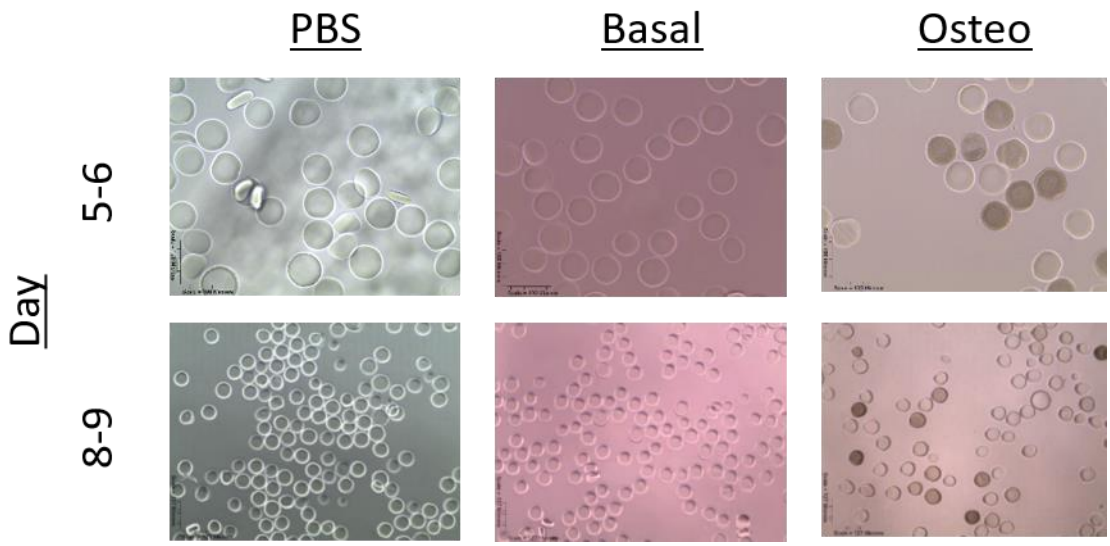

Figure 42 Spontaneous Mineralization Occurs in Osteogenic Media
Non-cell-containing microhydrogels were cultured in PBS, basal, or osteogenic media for two weeks. Even by one week, the osteogenic media had caused spontaneous mineralization in the microhydrogels. Scale bars are 200 μm.

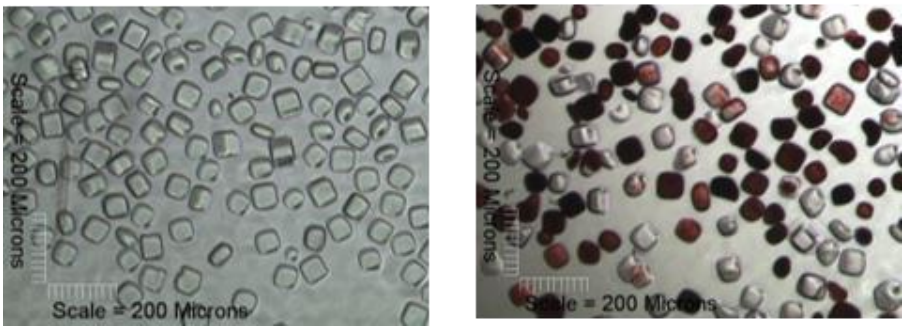

Figure 43 Staining of Automineralized Microhydrogels
These mineralized microhydrogels showed strong Alizarin Red staining as the mineralized material is labeled in a similar manner as mineralization produced by cells (Left – basal, right – osteo). Scale bars are 200 µm.

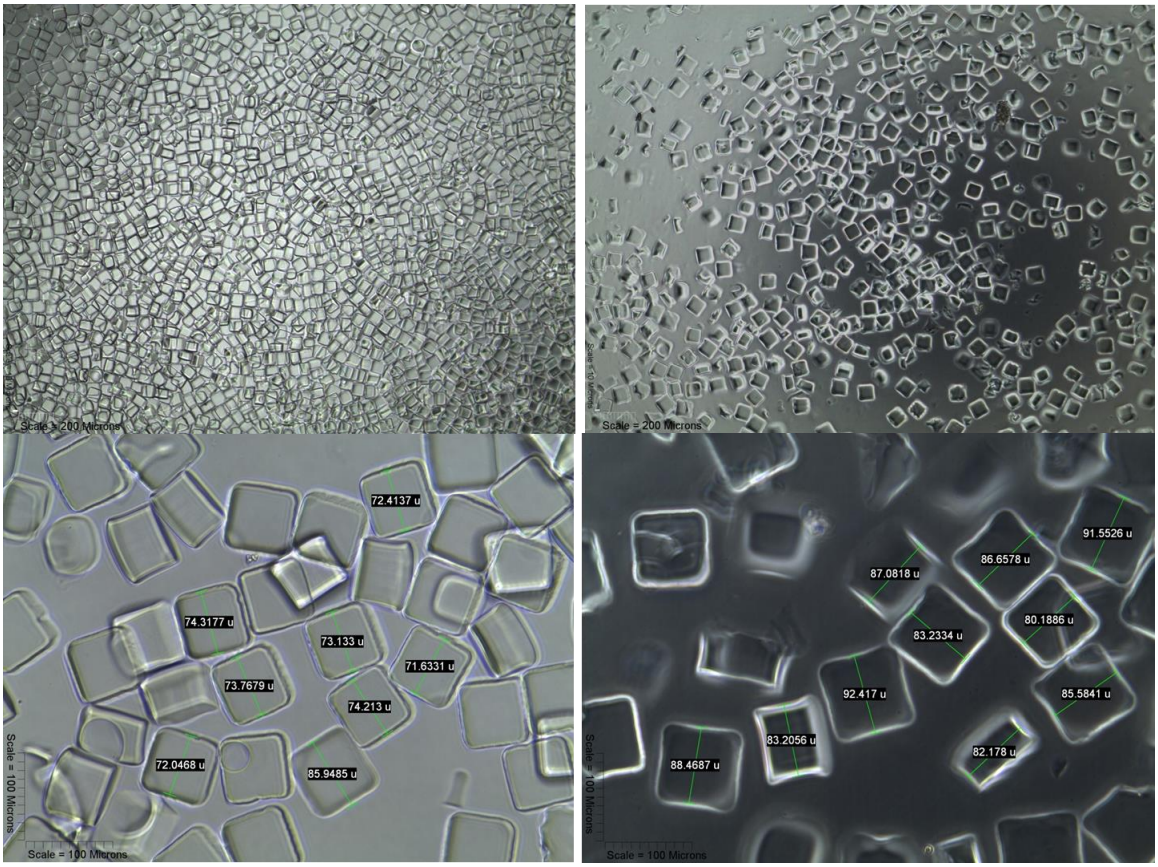

Figure 44 Comparison of Previous and Refined Microhydrogels
Microhydrogels were fabricated from 30% PEGDA3400 (left) or 4-armed monomers with thiol or norbornene functionality (example shown on right is 20% PEG-4NB + 0.6%DTT). The differences between these compositions were quantified (bottom row). Scale bars are 200 µm (top) and 100 µm (bottom). Averages are 74.65 µm (left) and 86.05 µm (right).

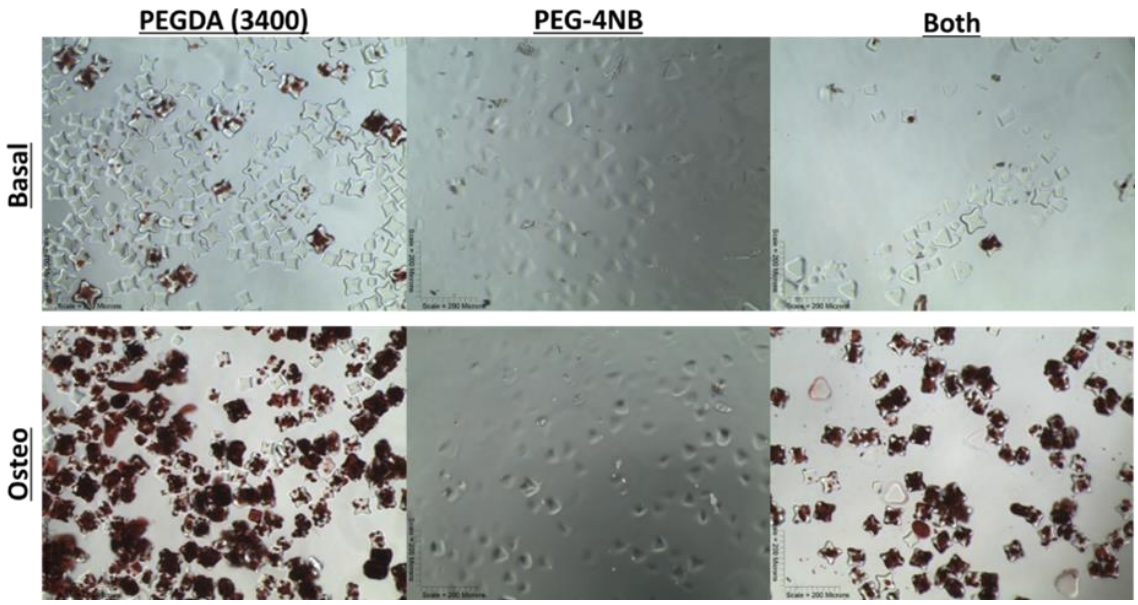

Figure 45 Minimal Mineralization is Observed Using Norbornene/Thiol Monomers Microhydrogels were fabricated using the previous monomer formulation and the new formulation and incubated for ten days. Each material was cultured (with no cells) in basal and osteogenic media conditions, alone and with the other material, for a total of four wells per material and six total wells. Scale bars are 200 µm.

4.2.4 Encapsulation of viable cells is achieved at controlled concentrations

4.2.4.1 Encapsulated cells remain viable

Fluorescent images of stained cells were collected and ImageJ used to quantify live and dead cells (for a total of more than 550 cells). This confirmed that cells remain viable post-gelation with approximately 79.9% +/- 1.1% viability 24 hours after crosslinking and no difference between viability in square and circle microhydrogels (**Figure 46**).

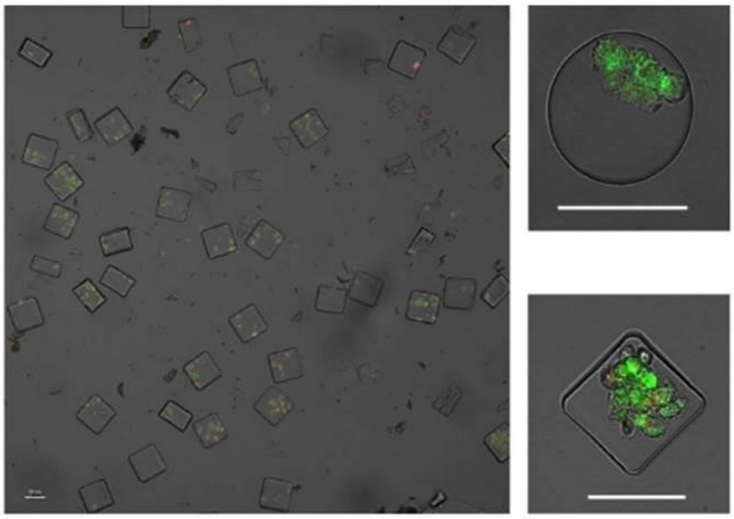

Figure 46 Cell Viability
Cell viability was measured from confocal images of encapsulated hMSCs (green – live, red – dead). Magnified images show that similar staining was seen in two different shapes. Scale bars are 100 μm.

4.2.4.2 Cell concentration in the prepolymer controls cell number in microhydrogels

A wide range of cell concentrations could be achieved in the selected microhydrogel geometries, which is an important variable in cell-niche interaction studies. Lower cell concentrations (10^5 cells/mL) mimic single cell-biomaterial interactions within a niche and higher cell concentrations (10^6-10^7 cells/mL) could be used to mimic organoids or tissue microenvironments (**Figure 47**). For each of the stated concentrations the number of cells per microhydrogel was quantified using fluorescence microscopy and ImageJ analysis of more than 185 wells. **Figure 48** (left) shows the low concentration case as a number average to demonstrate the proportion of wells with at least a single cell. In this lower concentration case, the majority of microgels contain either zero cells (which can be discarded during analysis) or a single cell in the context of the encapsulating biomaterial. For the higher concentration case, a weighted average is shown (**Figure 48**, right) instead to demonstrate the likely multi-cell community size.

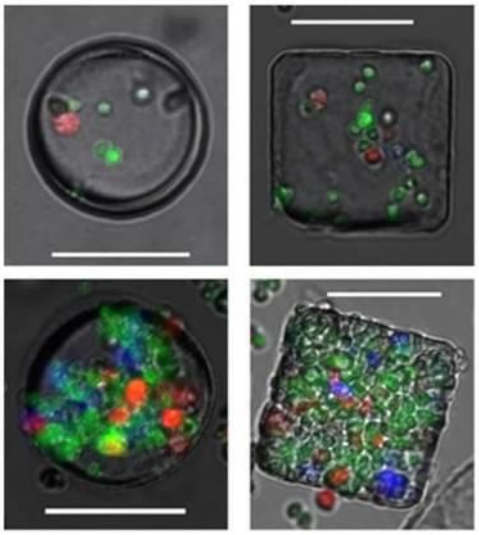

Figure 47 Cell Loading Image
Multiple cell types were encapsulated at different concentrations (top – low, bottom - high) to show the different types of microenvironments that could be constructed. (T cells – green, dendritic cells – blue, A20 cells – red) Scale bars are 50 µm.

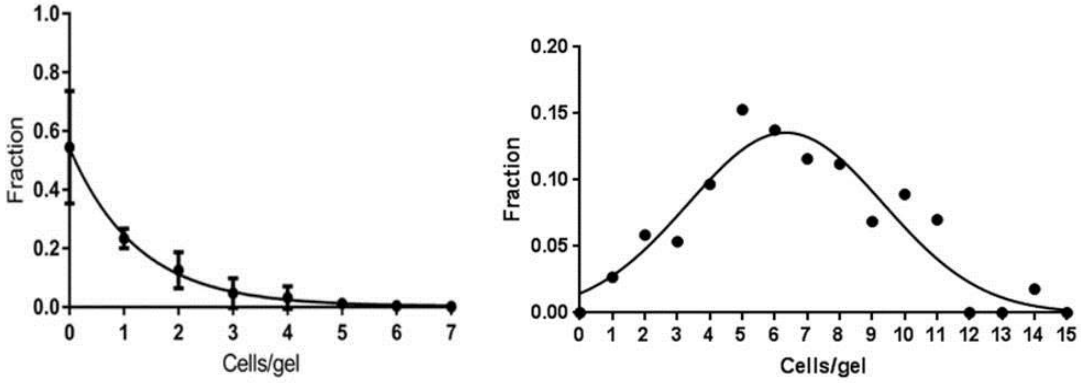

Figure 48 Cell Loading Quantification
Cell loading was quantified for each of the two loading concentrations. The low concentration case is shown as a number average and the high concentration case is shown as a weighted average.

4.2.4.3 Cell Labeling

Two example assays were performed on arrays of microhydrogels to demonstrate the versatility of the system. Similar assays have been shown by other groups and could be adapted for 3DMaC studies.[117-119, 163, 192] In this example, circle-shaped microhydrogels

consisted of 15% poly(ethylene glycol) diacrylate (Mw 3400) and 5% PEG-4SH in supplemented media. Square-shaped microhydrogels had the same starting polymer supplemented with 0.66 μM RGD peptide. Arrays were formed on PDMS via the same process described previously, however, in this case the top layer of PDMS was applied gently rather than tightly pressed. This leaves a thin layer of polymer between microhydrogels such that a large number of replicates in an array format can be easily imaged using microscopy.

Reactive oxygen species are oxygen radicals that can interfere with intracellular reactions, and a good measure of stress in the cell. In particular, ROS can be generated via free-radical crosslinking mechanisms which may impact cell viability and function. ROS activity is therefore an example of a short-term assay that could be performed on encapsulated live cells to determine (1) if different materials provide protection from ROS activity or (2) if external culture conditions such as drug concentration lead to cellular stress. The second method shows how traditional flow cytometry assays based on antibody staining are still applicable in the microhydrogel system. Microhydrogels can be fixed and permeablilized such that fluorescently-labelled antibodies can be incubated with the constructs such that they bind cell surface or intracellular markers.

To measure ROS activity, hMSC-containing microhydrogels were stained with DHR for 30 minutes immediately after crosslinking, rinsed, and imaged (**Figure 49**). These microhydrogels showed that the cells were actively converting the dye and therefore that they were experiencing ROS activity, which is to be expected after the crosslinking. A separate set of arrays were also imaged the next day (not shown) and fluorescence was reduced, indicating that the cellular stress was not a function of the encapsulating material.

To demonstrate antibody staining, hMSC-containing microhydrogels were fixed for 30 minutes immediately after crosslinking, then blocked with BSA and permeabilized with Triton-X100. Microhydrogels were incubated for one day with antibodies and DAPI to label CD105 and the cell nucleus respectively. CD105 is a constituent surface marker of hMSCs and therefore could be expected to have high expression and good staining. Previous characterization of the cells used here has been done by our group to confirm high CD105 expression (data not shown). Images of staining microhydrogel arrays were collected on a confocal scanning fluorescent microscope (**Figure 50**). The anti-CD105-PE antibody used here was designed for flow cytometry studies but can still be seen in the confocal microscope (DAPI staining not shown). These microhydrogels were imaged on the ISX to confirm that labelling would be seen in the flow cytometer. Brightfield images show that the circle and square shapes could be distinguished, and that the DAPI and PE staining were visible in fluorescence channels.

Next, this analysis template was applied to cell-containing microhydrogels. D1 cells were suspended in 30% poly(ethylene glycol) diacrylate at a concentration of ~60 million cells/mL for 60 µm circles and 60 µm squares. In this experiment, 60 µm Squares and Circles were considered as they were the most challenging shapes to separate in IDEAS. Future studies will expand the cell template to additional shapes and sizes. Here, Circles were generated with 30 seconds of UV exposure (previously selected for optimal cell viability and crosslinking); Squares were exposed for 2 minutes and therefore 4x the exposure. Given that free-radical polymerizations can generate harmful levels of ROS, DHR dye was selected to measure the resulting ROS activity in the context of the two microenvironments. Cells were stained for 60 minutes, washed with PBS, and stored on ice before analysis in the ISX.

As in the previous analysis, two truth populations were collected of only Circles (~48,000 events) and only Squares (~26,000 events). The template developed for non-cell-containing microhydrogels was applied and the Circle and Square populations were measured. The template still identified the two true populations with reasonable accuracy**.** However, the rate of mis-formed hydrogels was higher in the cell-containing prepolymer as cells disrupted edge features and so throughput was lower in the cell-containing system. There was also overlap into the Right Triangle gate which would need to be addressed in future by adding more feature gates to the template. This experiment showed that free cells, which are often included in analyzed population due to the thin layer of oxygen-inhibited prepolymer in PDMS molding, were collected in the 20 μm gates and so this barcode would need modification in the template. Therefore, the data in this assay was not gated by size, only shape. Because the amount of swelling will vary by polymer composition, size gates may need to be adjusted for each tested material.

After initial sorting, the data from the pure populations were computationally combined to analyze the difference in the two conditions. Constructs were gated into the desired populations using the above template with an additional gating layer for fluorescence signal to remove empty gels from analysis. The fluorescence intensity of each pure population was divided by the fluorescent area (to account for cell number) on a per gel basis (**Figure 51**). Feature values for those populations were then exported and averaged. Based on this example study, the Circles had an average of 309.95 +/- 169.53 and the Squares had 342.07 +/- 151.91. Therefore, there was no significant difference between the two groups either due to lowered accuracy in the sorting template or insufficient biological differences between the groups tested.

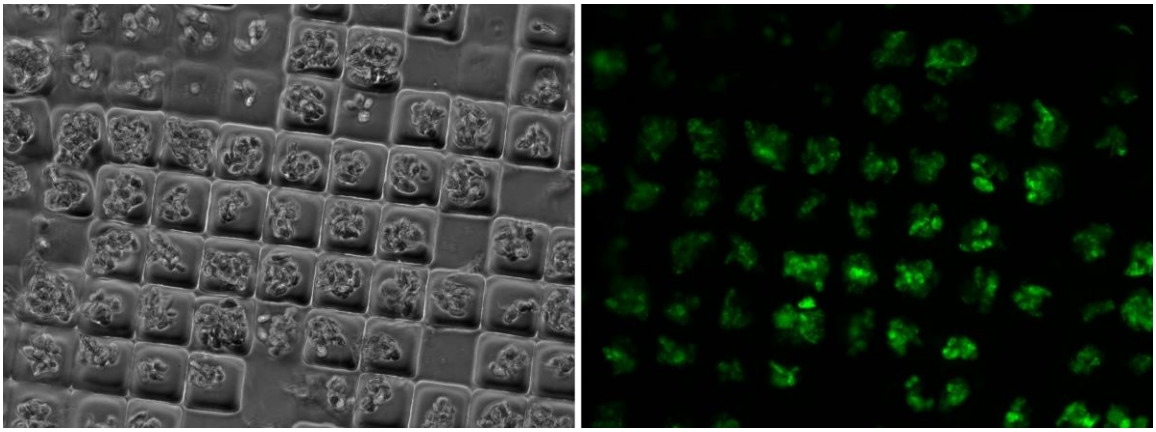

Figure 49 DHR Staining in Array-immobilized Microhydrogels
Microhydrogels were stained with DHR dye (false colored green) to show ROS activity after photopolymerization with UV light. (Left – phase contrast, right – fluorescence) Microhydrogels fabricated in 60 µm molds.

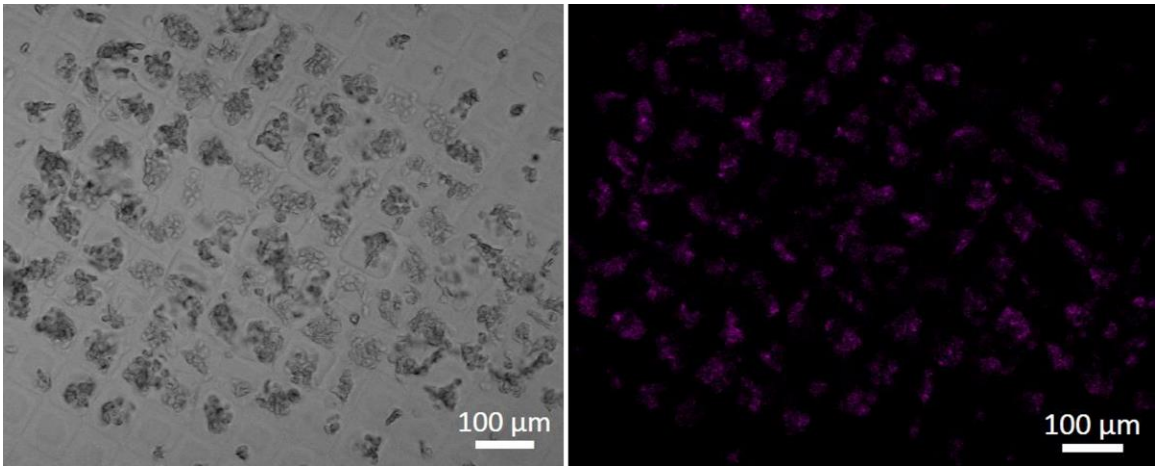

Figure 50 Antibody Staining in Array-immobilized Microhydrogels
Microhydrogels were stained with an antibody specific for a defining hMSC marker (purple). (Left – brightfield, right – fluorescence) Microhydrogels fabricated in 60 µm molds.

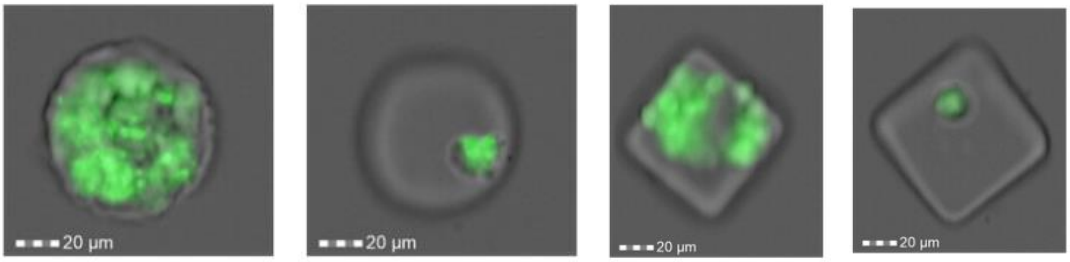

Figure 51 ISX-sorted DHR-stained Microhydrogels
Microhydrogels were exposed to varying amounts of UV light and ROS activity was measured using DHR. Circle (left two) and Square (right two) populations were gated and the fluorescence for each population was compared. The Circle gating collected 203 events and the Square gating collected 138 events.

4.2.5 Osteogenic Differentiation of hMSCs in 2D culture

hMSCs were plated on four 6-well tissue culture plates in basal and osteogenic media. Microscope images at each time point are shown in **Figure 52**. AR staining after each week of culture showed that mineralization deposition began on week 1 and increased over time. Mineralization in basal media was not seen at any time point, confirming that osteogenic media was required to induce differentiation to an osteogenic phenotype. Based on this study, microhydrogels were cultured for 10-14 days before starting evaluation of mineralization.

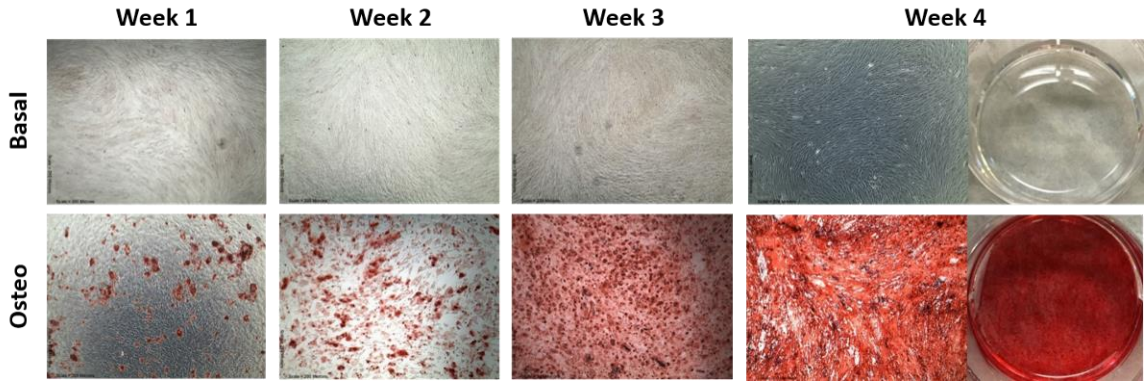

Figure 52 2D Osteogenesis
Mineralization was imaged using Alizarin Red dye at the end of each week of culture. hMSCs grown in basal media showed no staining and those grown in osteogenic media showed increased staining at the end of every week. Scale bars are 200 µm.

4.2.6 Screening osteogenic differentiation

After 13 days, AR staining showed that the basal condition had a low level of osteogenesis but that the osteogenic media resulted in noticeably more mineralization (**Figure 53**). At longer timepoints, this mineralization and therefore staining increased dramatically (**Figure 54**). This mineralization could also be seen with D1 cells cultured in osteogenic media (**Figure 55**).

While the AR staining of the hMSC-containing microhydrogels was visible, these microhydrogels had low contrast with the surrounding water due to the hydrogel composition (20% PEG-4NB + 0.6% DTT + 5 mM RGD). As a result, the ISX had difficulty collecting usable images of the microhydrogels. In another study, D1-containing microhydrogels (20% PEGDA3400 + 5% PEG-4NB + 5% PEG-4SH. Square – 5 mM RGD, Triangle - 1 mM HAVDI) were cultured in osteogenic media for 11 days. After culture, the microhydrogels were fixed and stained with Alizarin Red (**Figure 55**). These samples were then suspended in 2% PVA + 0.1% Tween20 in distilled water at a high concentration and images were collected on the ISX.

These images were masked and sorted based on the templates described in earlier sections. However, these shape barcodes showed reduced throughput now that cells were included and so the shapes were sorted by eye (**Figure 56**,

Figure 57). The mineralization for each population was then compared overall (**Figure 58**) and at the edge or center of the microhydrogels (

Figure 59). However, the variability in the populations was large, the counted microhydrogels fewer than 100 for each condition, and the resulting populations showed that the sorting algorithm designed in IDEAS was not as accurate as could be desired with some images clearly misclassified by the template (**Figure 56**). From the variables measured here for the mineralized microhydrogels, it is clear that there was a range of mineralization observed within each material population and so no clear differences between the materials. However, this may be due to the variable number of cells in each microhydrogel since any cell-cell interactions would limit the effect of including HAVDI peptide in only some of the microhydrogels.

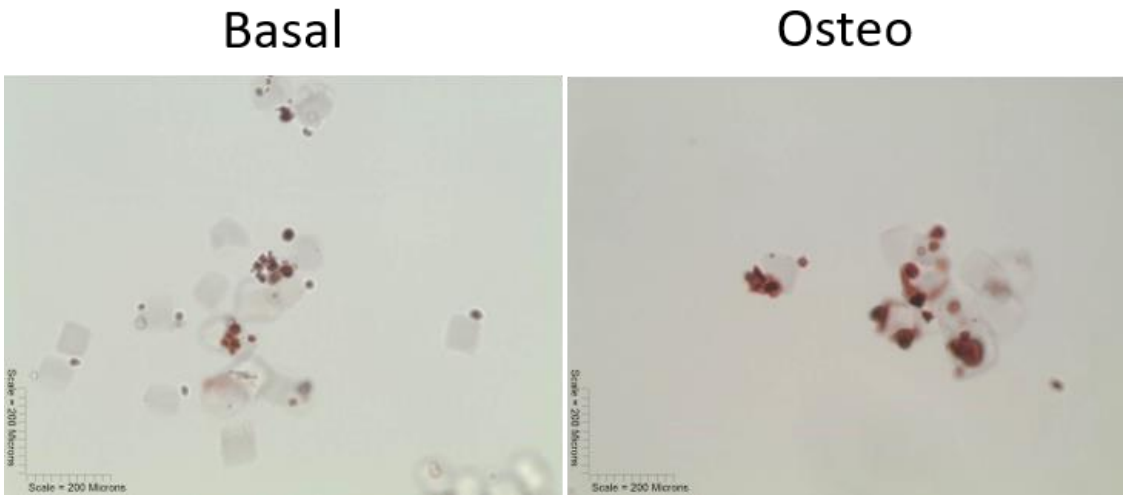

Figure 53 Alizarin Red Staining of Cell-Containing Microhydrogels
hMSCs were cultured for 13 days in basal or osteogenic media. The macromer solution was made of 20% PEG-4NB + 0.6% DTT + 5mM RGD. Scale bars are 200 μm.

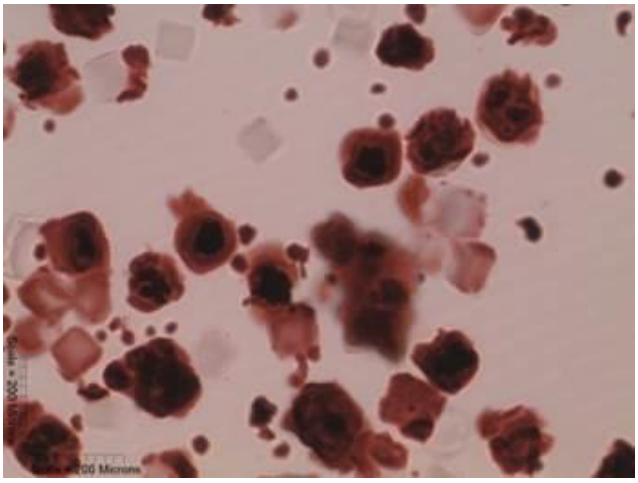

Figure 54 Over-mineralized Microhydrogels
If microhydrogels were allowed to differentiate for a longer period, the mineralization continued to spread and to distort the shape barcode. Note that this image has overly high background due to insufficient washing; however, the extent of mineralization is clear. Scale bars are 200 μm.

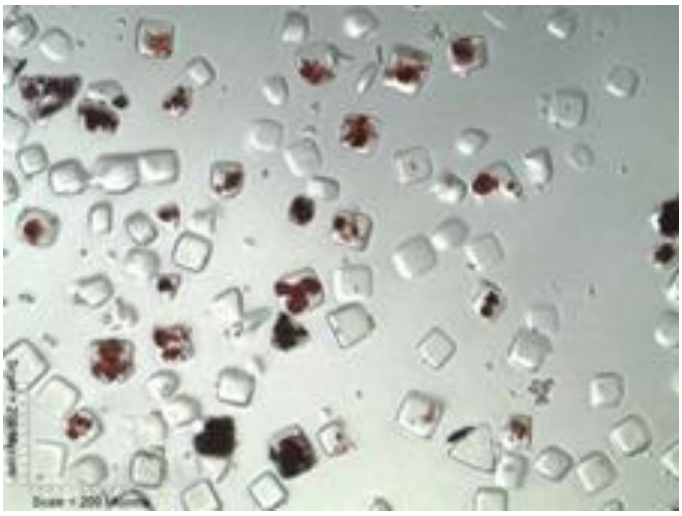

Figure 55 Mineralization of D1 Cells in Microhydrogels
D1 cells could also be induced to mineralize in microhydrogels containing RGD or HAVDI peptide. This formulation was 20% PEGDA3400 + 5% PEG-4NB + 5% PEG-4SH (Square – 5mM RGD, Triangle – 1 mM HAVDI). Scale bar is 200 μm.

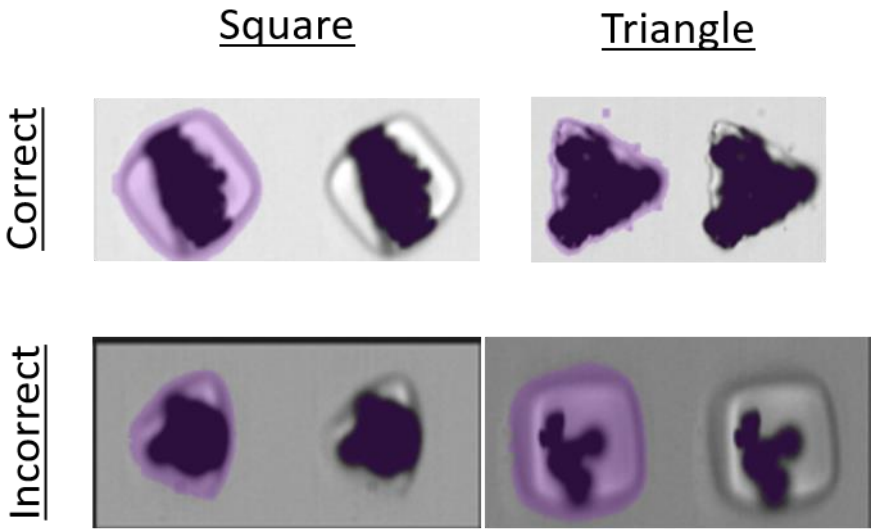

Figure 56 Analysis of Mineralized Cells in the ISX
Microhydrogels containing mineralized material could be imaged using the ISX and masked using the developed shape and mineralization templates. For each of the shapes there were images that were correctly classified and also those that were not.

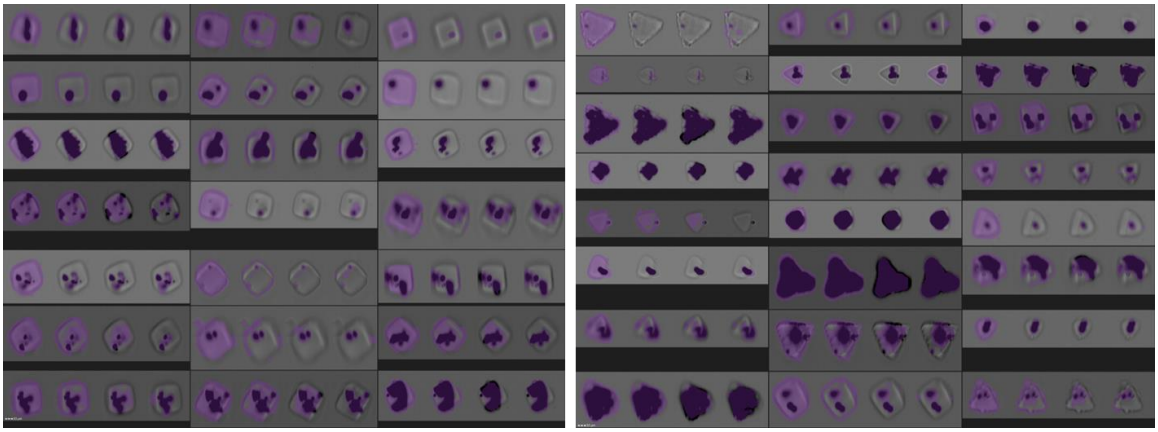

Figure 57 Representative Images of Mineralized Cells in Shaped Microhydrogels
For the two tested materials and shape barcodes, ideal images were identified by eye and masked using multiple designs to capture shape and mineralization. These are presented as representative images to show the range of analyzed images (left – square, right – triangle).

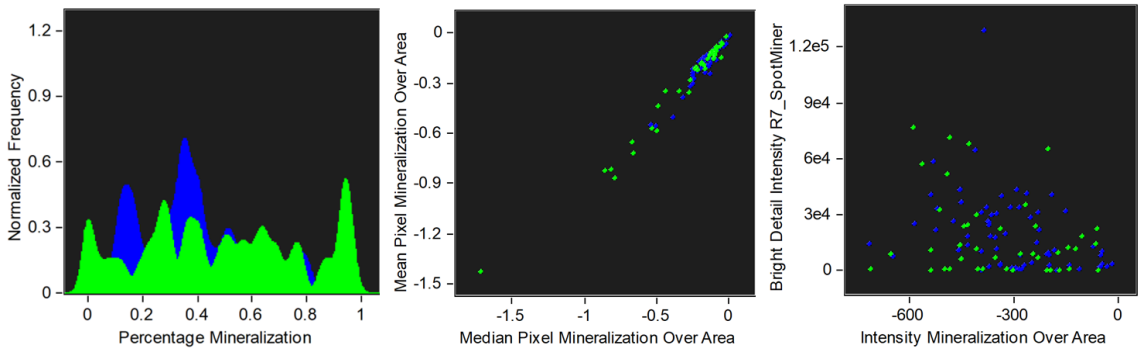

Figure 58 Measuring Mineralization in Shape-barcoded Microhydrogels
Mineralization in two shape-barcoded material compositions was compared. No differences were seen between the two materials in terms of the percentage of the area occupied by mineralization (left), the median pixel per area or the mean pixel per area (middle), or the intensity per area or bright detail intensity (right). (Square – blue, triangle – green)

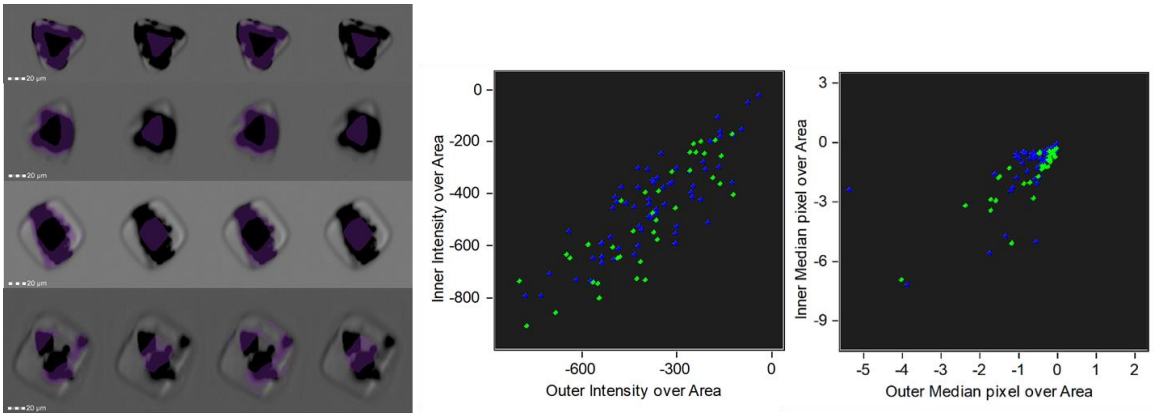

Figure 59 Measuring Mineralization at Edges and Interiors of Microhydrogels
Mineralization was also compared using masks specific for the outer 60-90% and inner 60% of microhydrogels. Examples of these masks are shown for two shapes each using two different masking protocols (left). There were no differences observed in these two masks for intensity per area (middle) or median pixel per area (right). (Square – blue, triangle – green)

4.2.7 Alternative MSC Differentiation – Adipogenesis

Adipogenesis of MSCs was also considered as a model system to illustrate 3DMaC's ability to assay biomaterials systems. Unlike the osteogenic media, adipogenic media did not result in any noticeable spontaneous changes to the microhydrogels. This differentiation system is also robust in *in vitro* culture which makes it another good test

system. hMSCs were shown to differentiate into adipocytes within two weeks of culture when seeded at high density and this could be clearly seen with a phase microscope (**Figure 60**). Oil Red is a small molecule histological stain similar to Alizarin Red which could be used to specifically stain the fat deposits in the cells (**Figure 60**). Antibody staining was also tested as a more specific measure of adipogenesis that would not result in background staining of the microhydrogels (both Oil Red and Alizarin Red do show a small amount of staining of blank microhydrogels). One specific protein expressed during adipogenesis is FABP4 (fatty acid binding protein 4) and so expression of this protein was probed. Interestingly, the cells used in this experiment showed inhomogeneous expression of the protein (**Figure 61**), which would be an important consideration if used as a model system.

Cells that were fixed in suspension instead of on the well-plate were also tested in an imaging flow cytometer to see if the Oil Red staining could be masked in the same manner as the Alizarin Red staining. These cells could be stained, imaged, and masked which suggests that this would also work as a model system (**Figure 62**). However, the adipocytes were fragile and many seemed to burst in either the process of collection or analysis. This bursting was hypothesized based on many collected images of sub-cellular-sized circle images that appeared similarly reflective to the globules in unstained cells. The adipogenesis model system was not tested any further because adipogenesis-inducing materials generally have a lower modulus than the materials tested in this Aim, which suggests that encapsulated cells would likely not differentiate effectively.

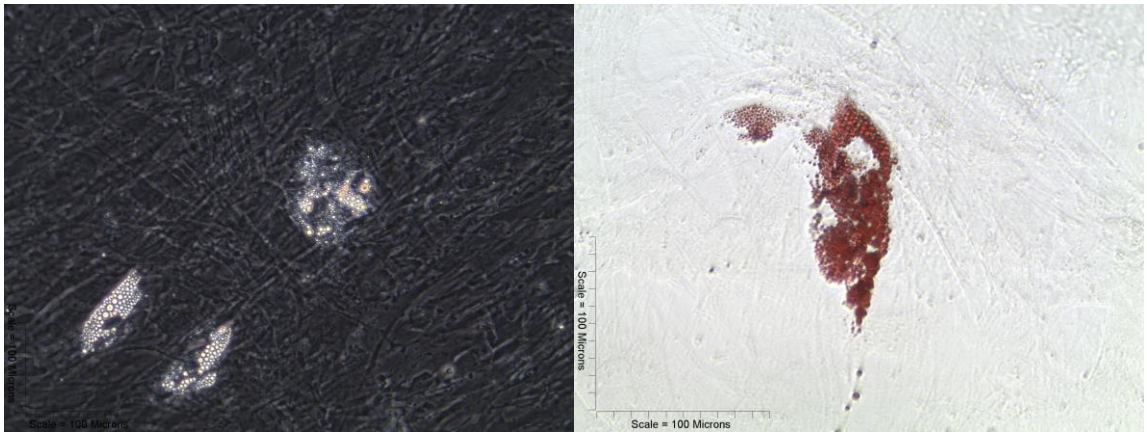

Figure 60 Adipogenesis of MSCs and Small Molecule Staining
hMSCs differentiated into adipocytes over the course of two weeks of culture. This could be seen using a phase microscope (left) or Oil Red histological staining (right).

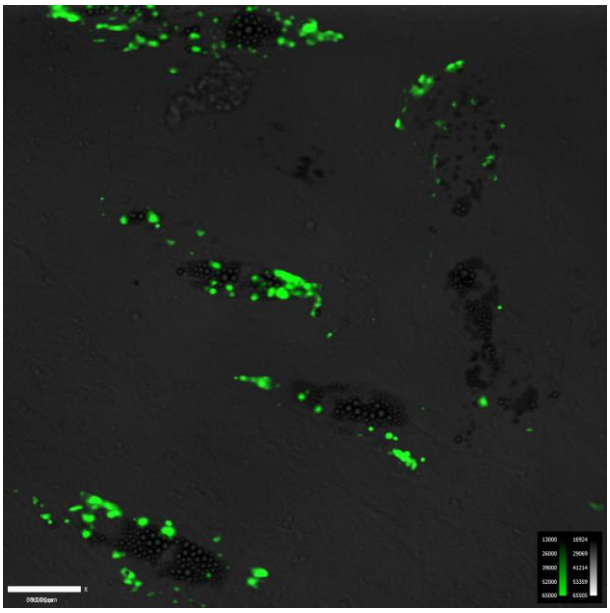

Figure 61 Staining of Adipocytes Using Anti-FABP Antibodies
Antibody staining could also be used to detect adipogenesis (green) via expression of fatty acid binding protein 4.

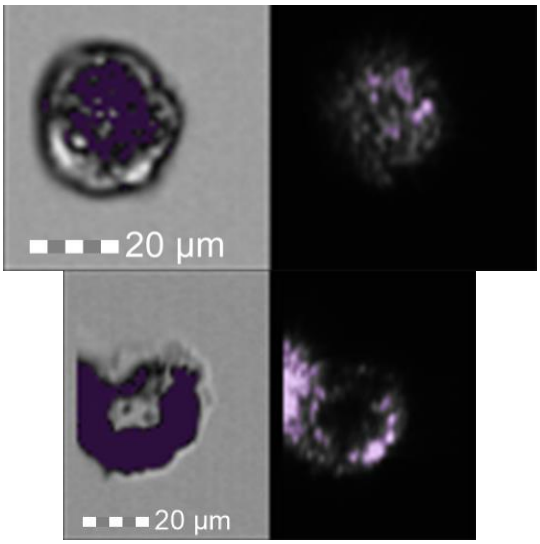

Figure 62 Imaging Flow Cytometer Analysis of Adipogenesis via Oil Red Staining
Cells were fixed, split into two populations, and half were stained in suspension before analysis on a FlowSight machine. The globule regions could be masked in either unstained (top) or stained (bottom) cells in both brightfield (left) and side scatter channels (right).

4.3 Discussion

Biomaterial microgels containing tumor and tumor-supporting cells, and stem cells were chosen for exploratory studies. Both cell types have heterogeneous population characteristics and a behavioral dependence on encapsulating material[100, 171]; and would therefore benefit from population-level statistics gathered from individual events. In stem cell research, the starting population can demonstrate a range of responses to identical biomaterial cues, and in cancer research *in vivo* behavior is best mimicked when tumor cells are co-cultured with supporting cells in an appropriate biomaterial niche[171, 193]. Therefore, while this method can easily be applied to single cell systems (similar to traditional FACS analysis), this method is unique in that it can also analyze entire cell niches within a biomaterial. While shape has important implications for 2D studies[194], no such dependence has been reported in 3D microgel culture. However, this remains an

interesting biological question for future studies and would need to be studied for each specific cell-biomaterial system of interest.

In this Aim the goal was to show how the 3DMaC method could be modified to enable the study of cell-material interactions in a high-throughput manner. Both adipogenesis and osteogenesis were considered before osteogenesis was selected. First, hydroxyapatite was used as a model system to determine an effective way to measure mineralization in the context of the ISX. As hydroxyapatite is very similar to bone, a stain (Alizarin Red) was available to stain mineralized material a bright red color. Because the cell-containing microhydrogels were expected to need additional gating to define the response signals, several different analysis templates were defined. This primarily meant defining an area-modified intensity mask to measure mineralization, however, this aim also showed how fluorescent small molecules and antibodies could be detected in the ISX. A standard curve of mineralization was also developed to correlate imaged mineralized area with a quantitative measurement of mineralized material.

An important caveat to this mineralization curve is that the 2D nature of the quantification does not fully measure the 3D encapsulation of HA in microhydrogels. This is because HA particles in more densely packed microhydrogels are likely to have some degree of stacking through the thickness of the microhydrogel, but the ISX will only see the footprint of these particles blocking light from passing through the microhydrogel. Here, this discrepancy was partially addressed by (1) quantifying primarily lower concentrations of HA that would have minimal stacking and (2) only analyzing images of microhydrogels correctly oriented to the camera. In the future, this could be further improved by using a non-linear fit for the data, using z-stacks in confocal

microscopy to make a more accurate standard curve, or using thinner microhydrogels to limit HA stacking.

Having developed an analysis method on the ISX, the cellular side needed to be addressed. MSCs from both human and mouse sources could be induced to differentiate down an osteogenic lineage using osteogenic media to culture 2D plated cells and this mineralization could be imaged with AR dye. Because the previous macromer formulation was found to induce spontaneous mineralization in microhydrogels during prolonged culture, new microhydrogel formulations were developed to address this problem. By using monomers that lead to larger mesh sizes in the material (and therefore higher swelling), auto-mineralization was not observed during the tested timeframe of two weeks. These new formulations used a similar crosslinking chemistry but led to key changes including increased crosslinking efficiency, higher cell viability, and increased film formation during fabrication. This film formation was addressed by decreasing the crosslinking time and also redesigning the PDMS molds such that the individual features were closer together.[118] These closer features made it more likely that a cell would settle into a well instead of remaining between the two pieces of PDMS and thus creating a space for polymerization.

Using these new macromer formulations, hMSC and D1 cells were observed to produce mineralized material within two weeks and stain strongly with AR. However, analyzing these microhydrogels using the ISX brought new challenges. Highly mineralized microhydrogels were denser than cell-free microhydrogels and much denser than the cell suspensions that the ISX is designed to analyze. As a result, microhydrogels containing mineralized material were imaged before the ISX completed its required calibrations or settled in the sample chamber. It was at this point that the PVA was added to the run

buffer to ensure that microhydrogels would remain suspended throughout the analysis period. Still, the ISX needed to be pulsed between the high and low speeds to keep the highly mineralized microhydrogels flowing.

Another reoccurring challenge was that the sorting template was less accurate for cell-containing microhydrogels. This occurred because the inclusion of cells often disturbed the corners and edges necessary to define the shape barcode. However, the sorting was also less accurate due to the changes in the macromer solution. The higher swelling resulted in less defined corners and a lower contrast between the microhydrogel and surrounding fluid.

To address these challenges and to continue improving the ability of 3DMaC to analyze cell-containing microhydrogels, there are several avenues that could prove productive. The first goal should be to try to improve the shape recognition of the microhydrogels. The low contrast could be approached by introducing an additional staining agent to the system. This could be a fluorescent label throughout the gel or immediately on the surface, either should be fine for the shape barcoding template. Fluorescence could be achieved either by incorporating FITC-PEG-acrylate throughout the gel or by incubating the microhydrogels with a fluorescently-tagged anti-PEG antibody. The contrast could also be improved with brightfield features. PEG can be specifically stained with barium iodide or with less hazardous trypan blue. The trypan blue has been effective and easy to control in our hands; however, it is removed by the addition of Tween-20 to the system and so has not been pursued.

As in the previous Aim, substantially better image classification may be possible by analyzing the images outside the confines of IDEAS. Images and feature values can be

exported for analysis elsewhere and one of the great advantages of flow cytometry is that it is easy to generate the massive number of training images needed for more powerful analytics. Future studies related to this aim might take advantage of the many fluorescence detection channels to look at other important cell characteristics or to evaluate different cell types. The microhydrogels used here are large enough to encapsulate most cell types and possibly entire multicellular microenvironments. As more *in vitro* analyses attempt to account for cell-cell interactions to accurately predict outcomes, 3DMaC provides the multiplexing needed to track multiple variables at once. Also, the 3DMaC SSF barcoding scheme could be extended to non-commercial cytometry systems. Already, many groups have used flow in microfluidics to analyze microhydrogels (barcoded with a range of methods) and such systems might be necessary for organoid cultures that are too large or too heavy for ISX analysis. Lastly, the 3DMaC system could be extended to non-imaging flow cytometers. If the materials are already going to have a fluorescence barcode for analysis, this can be equally well measured by traditional flow cytometers with the caveat that most currently available systems (the Fortessa or Aria for example) will only be able to analyze slightly smaller microhydrogels (<40 μm) due to their smaller fluidics.

CHAPTER 5 Aim 3

Develop and characterize 3DMaC's suitability for performing highly multiplexed, microhydrogel-based sandwich immunoassays

In this Aim, 3DMaC was adapted to assay microhydrogels functionalized for highly multiplexed detection of analytes in solution. The goal was to illustrate how the combination of shape-, size-, and fluorescence-barcodes analyzed in 3DMaC enables a much larger number of analytes to be detected in a single assay. Previously, the SSF barcode of the microhydrogel corresponded to the material composition, but in this Aim the SSF barcode indicates which analyte the microhydrogel is capable of detecting. Substantial modification of the previously developed method was needed for this Aim to conjugate antibodies to microhydrogels, optimize shape barcode fidelity, develop multi-color fluorescence barcoding, and design new analysis templates.

As for any detection platform, a biomaterial-based detection method will ideally combine high precision and sensitivity for the analyte of interest with low background signal. For biological systems this analyte can be any number of things including proteins, mRNA, carbohydrates, etc. There is a need to assay a large number of different analytes in solution in a high throughput manner. Such biological assays are increasingly used to scan serum samples, for example in immunology research, and it is preferable to test as many analytes as possible in a single run. Ideally, the method would be rapid, accurate, test small volumes, readily stored, and highly multiplexed. All of these requirements are met in 3DMaC.

While there is a need for biological detection platforms to be high-throughput to provide data on many replicates or experimental conditions, the greater advantage of 3DMaC is the potentially massive multiplexing that can be achieved. Using the ISX to determine SSF barcodes, potentially many more analytes can be analyzed at once than currently possible using existing methods.

5.1 Methods

5.1.1 Materials

Photomasks were purchased from Cad/Art Services. 0-50% (v/v) Poly(ethylene glycol) PEGDA (MW 575) + 0-30% (w/v) Biotin-PEG-Acrylate (Biotin-PEGA, MW 5kDa) were dissolved in a stock solution of 1% (w/v) LAP and 1% (v/v) NVP in PBS. PBST was prepared from PBS + 0.5%(v/v) Tween-20. Streptavidin was purchased from Bio Basic and Streptavidin-RhodamineRedX was purchased from VWR; both were dissolved in PBS at 2 mg/mL, aliquoted, and stored at -20^{o}C. Biotinylated Atto-647 was purchased from Sigma Aldrich, dissolved in 50% (v/v) DMSO (Dimethyl Sulfoxide) in PBS at 0.5 mg/mL, aliquoted, and stored at -20^{o}C. BSA and BSA-AlexaFluor488 were purchased from ThermoFisher. Antibodies were: AlexaFluor488 Donkey anti-Rabitt IgG (BioLegend, 406416), Anti-IL10 (Abcam, 222630), Anti-TNFα (Abcam, 34674), Anti-IL6 (Abcam, 7737), Anti-BSA (ThermoFisher, A11133), Anti-IFNβ (ThermoFisher, PA5-20390) Biotinylated antibodies were: Anti-TNFα (ThermoFisher, AMC3719), anti-IL6 (BioLegend, 504602), Anti-IL10 (BioLegend, 505004), Anti-IFNβ (BioLegend, 508105). Protein standards were: TNFα (BioLegend, 575209), IL-6 (BioLegend, 575709), IL-10 (BioLegend, 575809).

5.1.2 Microhydrogel Fabrication and Functionalization

PDMS molds were fabricated as previously described. Molds were activated by oxygen plasma for 5 minutes and 10 µL of prepolymer was directly pipetted on the surface. Molds were sealed using an equally sized slab of untreated PDMS and exposed to 365 nm light for 60 seconds. The top slab was removed and PBST was pipetted onto the mold surface to hydrate the microhydrogels. Microhydrogels were collected in low adhesion Eppendorf tubes via centrifugation, counted, and rinsed three times in PBST or TBS (Tris Buffered Saline). 2 mg/mL Streptavidin in PBS was added to the microhydrogels at 7e-7 µg/µm^2 (where the area refers to the surface area of the microhydrogel multiplied by the number of microhydrogels) and rotated for at least 30 minutes. A small sample of microhydrogels were instead rotated with fluorescently-labeled streptavidin and used as a positive control for binding. Rinsing was repeated as before. **Figure 63** shows a schematic of the functionalized microhydrogels.

Microhydrogels were next incubated with biotinylated capture antibody at a concentration of 0.5 mg/mL (in a 3:1 molar ratio of antibody to streptavidin) and rotated for at least two hours. This step was conducted in a TBS-based blocking buffer (Odessey) to limit non-specific binding. Again, a small sample was incubated instead with a biotinylated dye such that binding could be measured after rinsing. Rinsing was repeated before storage at 4^{o}C. **Figure 64** shows a schematic of the functionalized microhydrogels.

An alternative functionalization of microhydrogels was also tested based on the protocol from the Doyle group. In this method, EDC/NHS chemistry is used to modify NH_2 groups on the antibody directly and covalently link the antibodies to a Maleimide-PEG-succinimidyl linker before use. This maleimide group could then participate in the free

radical crosslinking reaction. Two antibodies were tested, one with a TexasRed fluorophore and one with a FITC fluorophore.

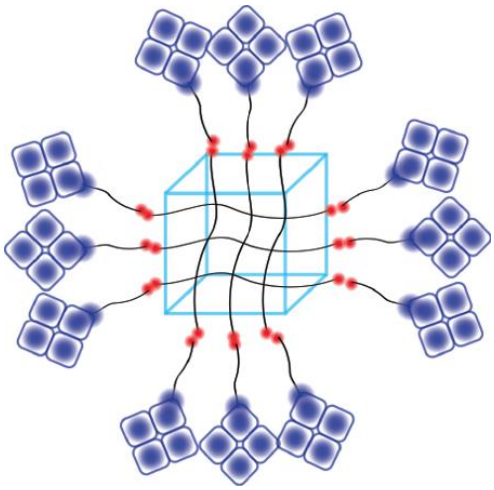

Figure 63 Schematic of Non-specifically Functionalized Microhydrogel
In this example, a cube of PEGDA forms surface acrylate-acrylate (red) bonds and biotin groups (blue) extend from the edge. These biotins are bound to streptavidin (blue squares).

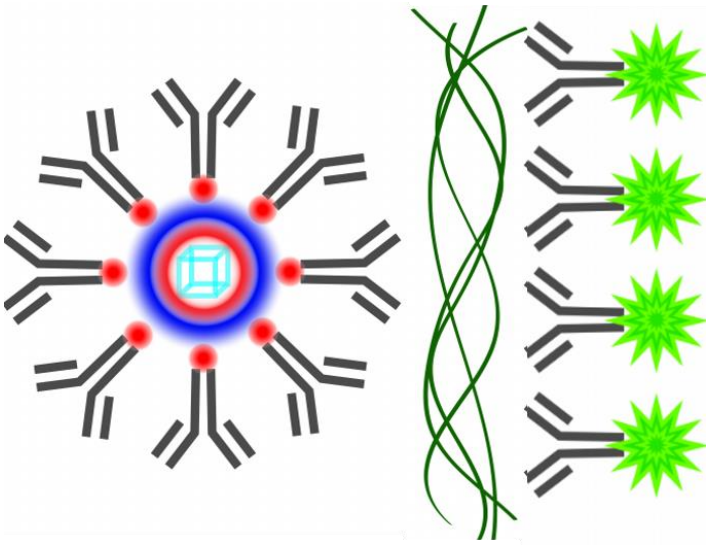

Figure 64 Antibody-functionalized Microhydrogel and Intended Binding
Biotinylated antibodies are bound to the available sites on streptavidin. Incubation with specific proteins (green) will result in binding that can then be detected with fluorescence-tagged detection antibodies.

5.1.3 Detecting Microhydrogels Using Non-imaging Flow Cytometry

For these experiments, Jiaying (Ingrid) Liu from the Roy lab and Sommer Durham from the Georgia Tech Flow Cytometry Core are both acknowledged for data collection. Microhydrogels were fabricated at smaller sizes and collected in PBS at a high concentration. FSC and SSC graphs were used to look for the presence of microhydrogels. The laser intensities were lowered to minimal levels to try to shift the peak of the FSC plot below the highest measurable value on the LSR-Fortessa. Using the FACS-Aria, a neutral density filter was applied with the same goal. For some experiments, microhydrogels were functionalized with fluorescence to assist with detection in the flow cytometer.

5.1.4 Expanded Barcoding Shapes

New shapes were designed in AutoCAD based on the previous set of twelve test barcodes. These new shapes were: pentagon, star, crescent, clover, dogbone, and keyhole. The pentagon and star were intended to test how well the sorting algorithm could identify an increasing number of edges on the shape. The crescent and clover were meant to introduce concavity as an additional variable. The dogbone and the keyhole were designed with one long axis based on the observations that (1) longer shapes would generally orient themselves parallel to the direction of flow and (2) the imaging environment of the ISX is designed such that the length of the image is variable and dependent on the length of the imaged object.

5.1.5 Expanded Barcoding Fluorescence

Microhydrogels were incubated with fluorescently labeled versions of streptavidin (Cy3, APC, or RhodamineX) and biotin (FITC or Atto647) to create a range of combinations.

Single color and blank microhydrogels were collected as well. Note that here fluorescent barcoding was achieved by labeling the linker molecules, however, fluorescence could also be included in the macromer solution either by using labeled macromer or by including functionalized fluorescent nanoparticles capable of polymerizing with the system. To eliminate shape as a possibly confounding variable, a single shape barcode was used for each experiment and a gate of Area vs. AspectRatio was applied to the data to remove disoriented microhydrogels (~60% removed). Laser powers were optimized on single color controls and compensation was performed in IDEAS after data collection.

5.1.6 Standard Curves

Based on the optimized microhydrogel formulation, standard curves were produced to test the amount of streptavidin and subsequent biotin groups could be bound to the surface. The same RhodamineX-functionalized streptavidin was used to measure how much could be bound to the surface. Keeping the solution volume and microhydrogel number constant, the microhydrogels were incubated in ten different concentrations ranging from 0 to 1 µg/µgel and shaken for 2 hours. Dilution was performed in PBS + 0.01%Tween-20.

A standard curve was prepared from BSA (either unconjugated or with an AlexaFluor488 tag). Concentrations tested were: 1 mg/mL, 100 µg/mL, 1 µg/mL, 100 ng/mL, 1 ng/mL, 1 pg/mL, and 0 (negative control). Microhydrogels were added to 0.6 mL Eppendorf tubes, centrifuged, and supernatant removed. Incubation consisted either of 4 hours on a room temperature shakerplate or overnight at 4^{o}C. This step was conducted in a TBS-based blocking buffer to limit non-specific binding. Rinsing was repeated as before. Fluorescently-labeled BSA standard curves were then evaluated in a spinning disk

confocal microscope and using the ISX. Unconjugated BSA standard curves were incubated with a detection antibody, rinsed, and imaged in the same manner.

5.2 Results

5.2.1 Microhydrogel Fabrication and Functionalization

Macromer solution was designed to have high streptavidin binding capability without sacrificing barcoding accuracy. PEGDA575 was selected as the base macromer solution because crosslinked gels will have a small mesh size and little swelling. This will maintain higher shape fidelity and prevent functionalization of the internal volume (rather than the surface). Different ratios of PEG macromer and Biotin-PEGA were fabricated (**Table 5**) and functionalized with fluorescent streptavidin (StrepRhodX) as a proxy for the number of biotin moieties that were present on the surface of the microhydrogels. As seen in **Figure 65** the binding was highest with 10% Biotin-PEG-Acrylate. This was surprising because one would expect that a higher proportion of Biotin-PEGA would result in more moieties present on the surface; however, the Biotin-PEGA also had a low solubility under the chosen experimental conditions with particulate visible at 20% (w/v) and excessive particulate at 30% (w/v).

A second experiment was performed in which the amount of PEGDA575 was varied to determine how the reduced pore size impacts the binding of streptavidin (**Table 6**). Interestingly, the highest tested concentration of PEGDA575 was found to have the highest binding (**Figure 66**). Higher concentrations were not tested as the gels become increasingly brittle but there could be room for improvement still with optimization of the macromer solution.

During testing an unexpected variable, functionalization time, was identified. Namely, for some samples the availability of the Biotin-PEGA groups seemed to decrease over time with immediate streptavidin functionalization resulting in higher observed fluorescence than those samples incubated even one hour later (**Figure 67**). This was primarily seen with the PEGDA575 solutions, microhydrogels derived from PEG-4NB macromer solutions could be functionalized equally well even after a 48 hour waiting period (**Figure 68**). It is posited that those microhydrogels designed with larger mesh sizes and swelling maintain high accessibility of their biotin moieties whereas the PEGDA575 might undergo a less favorable rearrangement of biotin away from the surface.

Finally, an alternative antibody incorporation method was also tested. In this system, the antibodies are covalently incorporated during fabrication by treating attaching the antibodies to a linker group before crosslinking. This is easier from a processing standpoint and did result in antibody incorporation as demonstrated using fluorescently-labeled antibodies (**Figure 69**). However, there are also downsides to this method that led to the biotin attachment strategy being preferred. The covalent incorporation method requires that the barcode-antigen selection happen earlier which results in a less flexible experimental system. It also could lead to waste of material as the antibody will be incorporated throughout the volume of the gel but larger analytes might not be able to penetrate past the surface, which means more antibody was used than necessary. Based on these disadvantages, the biotin-functionalization method was used in following experiments.

Table 5 Conditions for Maximizing Surface Biotin by Varying Biotin-PEGA
Macromer solutions used in **Figure 65**.

PEGDA 575 (%)	PBS + Photoinitiator (uL)	Biotin-PEG-Acrylate (%)	4-arm PEG-Norbornene (%)
40	60	0	
20	80	20	10
40	60	1	
40	60	2	
40	60	5	
40	60	10	
40	60	30	
40	60	40	

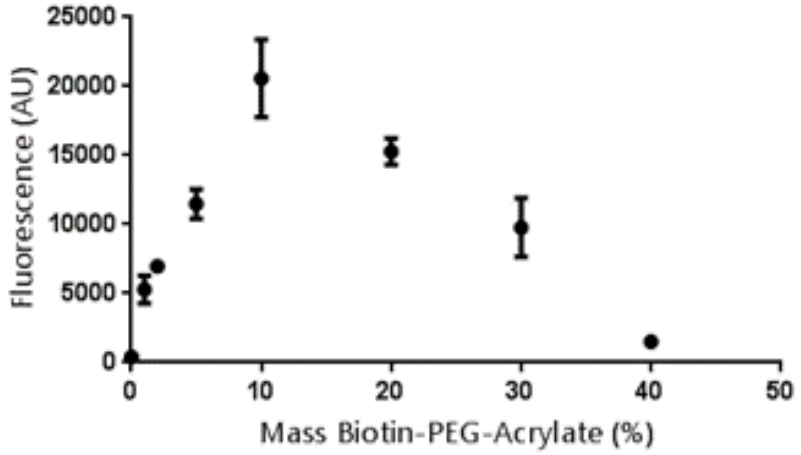

Figure 65 Maximizing Surface Biotin Groups by Varying Biotin-PEGA
Fluorescent streptavidin was bound to surface biotins and quantified via microscopy.

Table 6 Conditions for Maximizing Surface Biotin by Varying PEGDA
Macromer solutions used in **Figure 66**.

Sample	P575 (uL)	Biotin-PEG-Ac (%)	PBS + PI (uL)
Negative	50	0	50
A	50	10	50
Previous	40	10	60
B	40	20	60
C	30	20	70
D	30	30	70
E	20	30	80

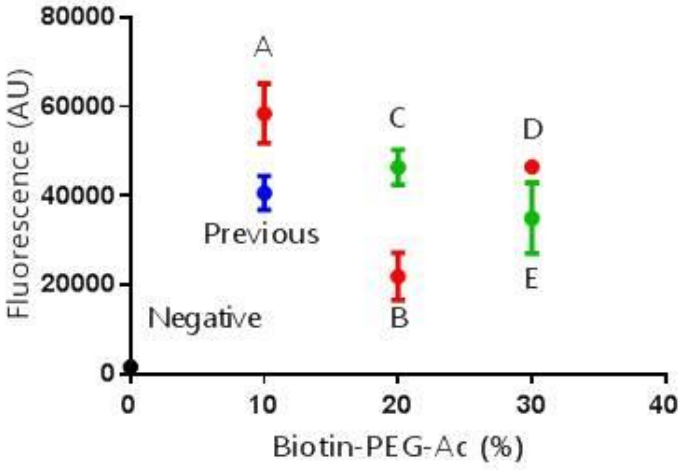

Figure 66 Maximizing Surface Biotin Groups by Varying PEGDA
For each Biotin-PEGA concentration, two concentrations of PEGDA were tested relative to streptavidin binding.

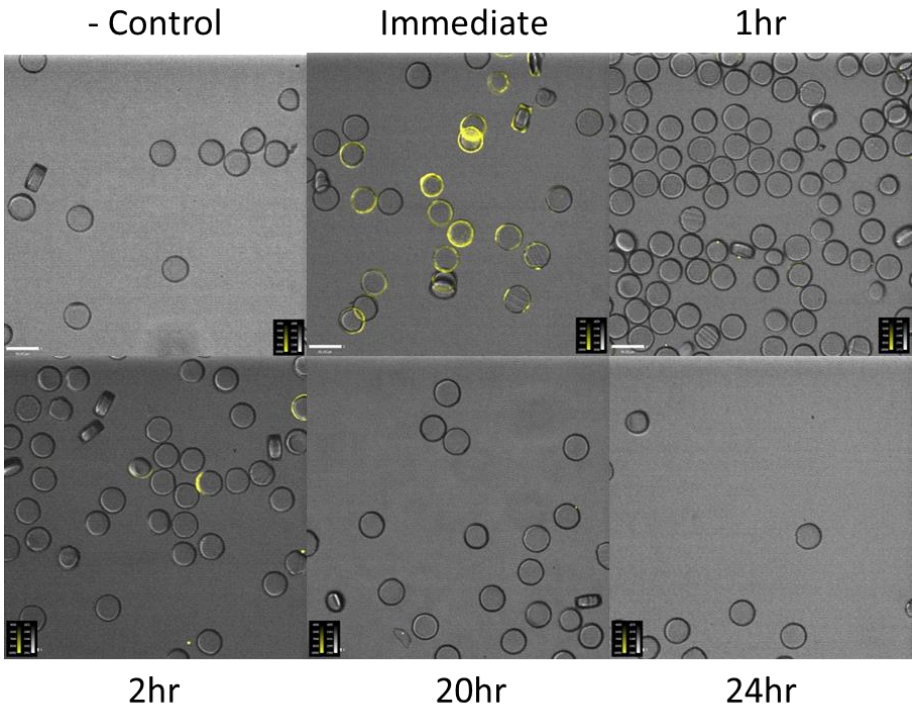

Figure 67 Time Study of Streptavidin Binding with Small Mesh Size
Immediate incubation with streptavidin was necessary for the microhydrogels with smaller mesh size (40% PEGDA (MW 575) + 20% Biotin-PEGA). Scale bars are 100 µm.

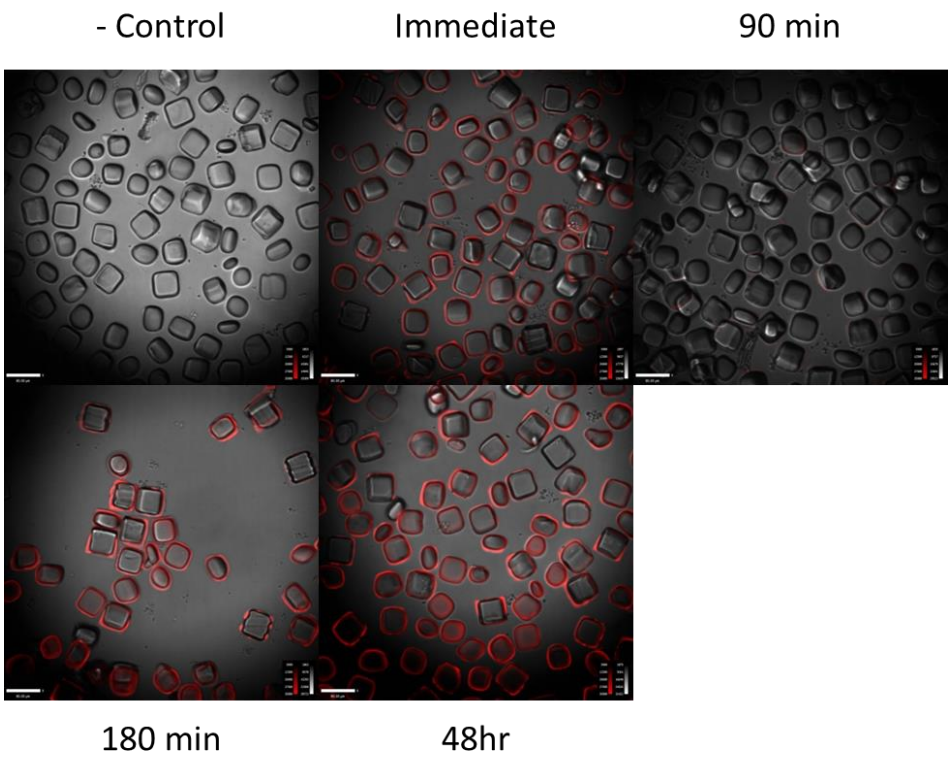

Figure 68 Time Study of Streptavidin Binding with Large Mesh Size
Immediate incubation with streptavidin was unnecessary for the microhydrogels with larger mesh size (Macromer corresponding 10% 4ArmPEGDA (MW 20kDa) + 20% PEGDA (MW 575) + 10% Biotin-PEGA). For unknown reasons, the 90 minute group showed low binding. Scale bars are 100 µm.

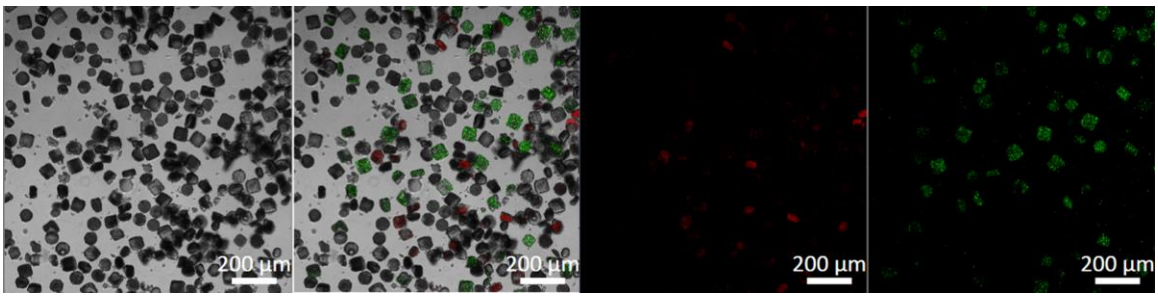

Figure 69 Covalent Incorporation of Fluorescence-tagged Antibodies
Two different antibodies were covalently bound into the hydrogel matrix during crosslinking. After extensive rinsing, the fluorescent signal could be used to show that the antibodies were incorporated successfully. Shown are the phase contrast and fluorescent channels, along with an overlaid image.

5.2.2 Detecting Microhydrogels Using Non-imaging Flow Cytometry[4]

In Aim 1 and Aim 2, the potential to expand SSF barcoding to non-imaging flow cytometers was discussed. This would expand the utility of the method for both the tissue engineering and molecular analytics studies. However, current flow cytometers such as the FACS-Aria and LSR-Fortessa (both from BD Biosciences) have smaller microfluidics than the ISX and so would only accommodate smaller microhydrogels ($\leq$ 40 μm), which are less convenient for TE studies. However, smaller microhydrogels are more favorable for detection applications due to the reduced material necessary for fabrication. Two different experiments were performed to test the potential of the FACS-Aria and LSR-Fortessa (**Figure 70**). These experiments show that microhydrogel events were detectable with the application of the density filter; however, different sizes only showed a small shift on the graph. Nanoparticle sizes can be distinguished using flow cytometers and so the detectors may be more sensitive when detecting smaller sizes. This is a potential avenue for future work along with testing different shapes.

---

[4] Partially adapted from a supplementary figure of Parratt, K.; Jeong, J.; Qiu, P.; Roy, K. 3D Material Cytometry (3DMaC): A Very High-replicate, High-throughput Analytical Method using Microfabricated, Shape-specific, Cell-material Niches. *Lab on a Chip*, 2017, 17, 2861-2872.

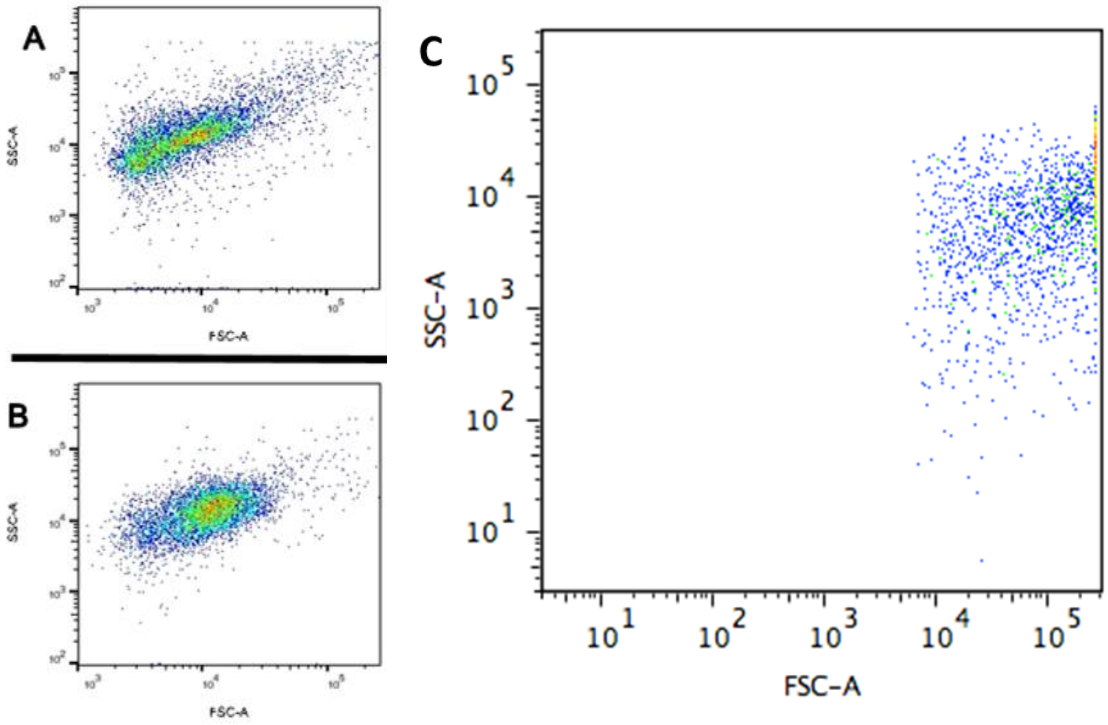

Figure 70 Non-imaging Flow Cytometers Cannot Accurately Detect Microhydrogels Microhydrogels of two different sizes (A) 20 µm and (B) 40 µm were analyzed using the FACS-Aria and a small shift was seen between samples. In the LSR (C), even at low laser powers, the majority of the fluorescently labeled microhydrogels (used to confirm that the events were microhydrogels) appeared only on the right-hand side of the graph.

5.2.3 Expanded Barcoding Shapes

Several shapes were difficult to form due to areas with minimal dimension that could not polymerize consistently under the given polymerization conditions. Namely, the points of the crescent and the smallest length in the dogbone did not always successfully polymerize. However, the overall shapes were still largely determinable to the human eye (**Figure 71**). Using the ISX and labeling the true populations in a similar manner as before, the shapes could be compared against each other to calculate the variables that provide the greatest separation.

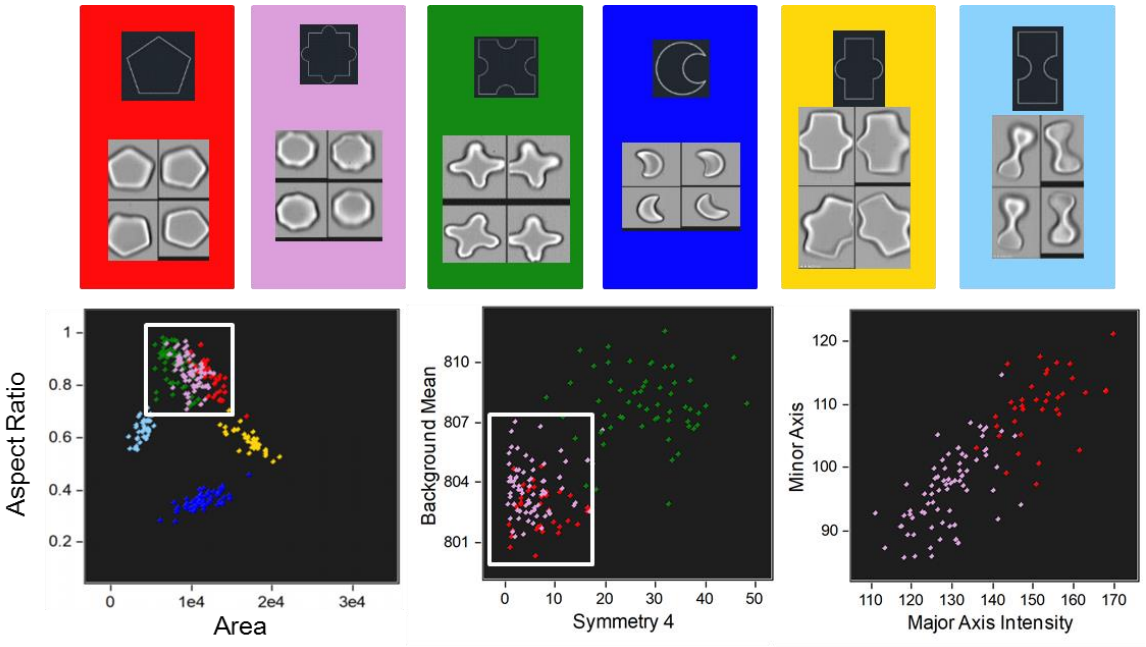

Figure 71 Expanded Shape-based Barcoding
Six new shapes were added (top, AutoCAD design and ISX images) and sequentially graphed relative to six features of interest (bottom left to right). Color-coding relates the points on the graph.

5.2.4 Expanded Barcoding Fluorescence

A range of fluorescent barcodes were explored for the ISX with the intent of testing if a Luminex-like two-color fluorescent barcodes could be used (**Figure 72, Figure 73, Figure 74**). The machine is configured with four lasers and a SSC laser which are collected in ten fluorescent channels which are located on two separate cameras. This means that there are five channels being collected on each camera and therefore that there will be less crosstalk if fluorescent barcodes consist of two colors collected on separate cameras.

After compensation for overlap between the colors used, the images were gated on "Intensity" for Rhodamine intensity and then "Median Pixel" for Atto intensity. Using microhydrogels collected as "true" data, the throughput and accuracy of this gating was

calculated (**Table 7**). For example, the throughput of sample A was equal to the number of A microhydrogels in gate A divided by the total number of A samples that were correctly oriented to the camera. The accuracy was the number of A microhydrogels in gate A divided by the total number of microhydrogels in gate A.

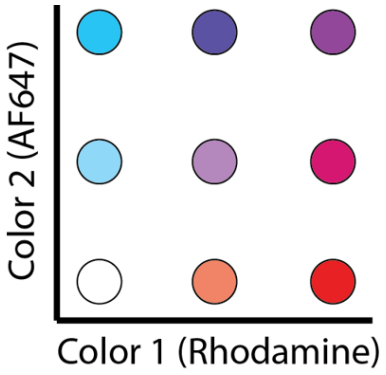

Figure 72 Ideal Fluorescent Barcodes
Microhydrogels were designed to have three concentrations of Rhodamine-streptavidin and then each group divided into three again and incubated with Atto647-biotin to give a total of nine fluorescence barcode.

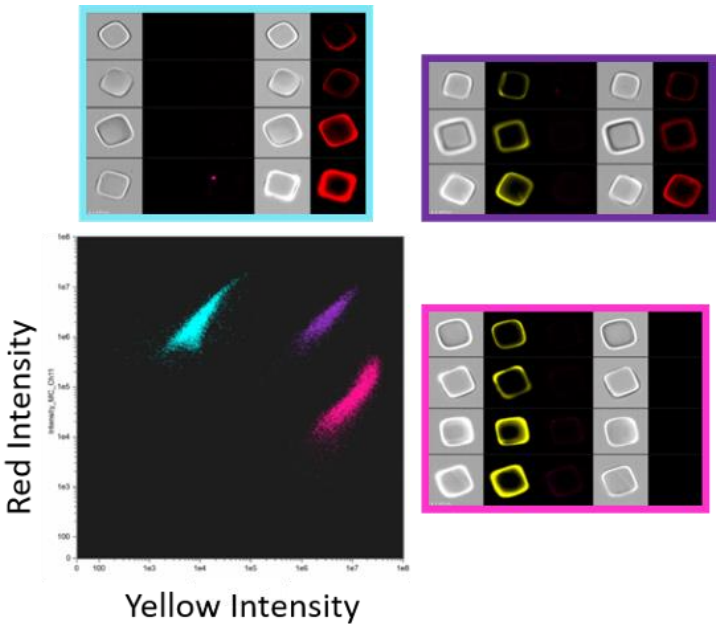

Figure 73 ISX Data from Three Fluorescence Barcodes
Only single and double positive color barcodes were tested to determine concentrations and laser powers.

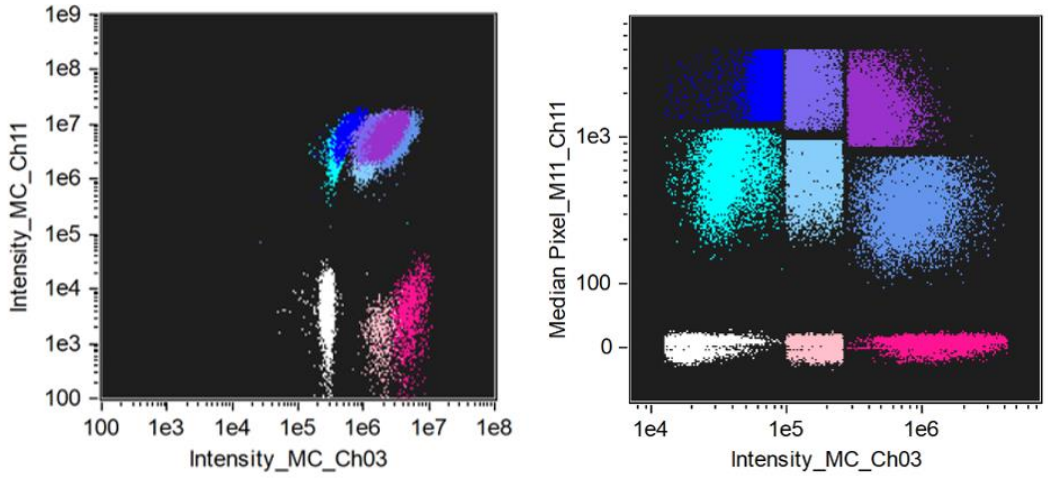

Figure 74 ISX Data from Nine Fluorescence Barcodes
Nine combinations were tested, even with compensation there is visible cross-talk in the samples with the highest Atto concentration. (Left – ungated true populations, right – populations after gating)

Table 7 Fluorescence Barcoded Microhydrogel Throughput and Accuracy
Calculated as described in the text.

Barcode	Throughput (%)	Accuracy (%)
A	99.8	96.3
B	72.0	99.3
C	99.4	81.5
D	88.9	88.9
E	69.8	93.8
F	95.1	91.1
G	72.3	70.9
H	76.1	61.9
I	84.1	88.7

5.2.5 Standard Curves

Standard curves were created to measure the amount of streptavidin (**Figure 75**) and subsequent biotin (**Figure 76**) groups could be bound to the surface of the microhydrogels.

By determining the maximum possible loading of streptavidin and biotin on the surface of the microhydrogels, masses of streptavidin and biotinylated antibody were selected for functionalizing the microhydrogels. It is important to note that a biotinylated antibody is much larger than the biotin small molecule alone and so the maximum surface loading is unlikely to approach that of the test fluorescent biotin. A standard curve was then prepared from fluorescent BSA protein and samples were incubated with anti-BSA functionalized microhydrogels (**Figure 77**). These values were not as sensitive as desired, ELISA and Luminex systems can detect down to the range of pico- to nano-molar amounts.

One possibility is that the sensitivity of the ISX may be higher than that of the confocal microscope and so the samples were also tested on the ISX (**Figure 78**). Unfortunately, the detection of the ISX did not exceed that seen on the confocal microscope and the peaks for the different samples have a wide range of median intensities. Therefore, the current iteration does not match the Luminex or ELISA. However, those systems use a detection antibody coupled to a signal multiplier in the form of either a colorimetric reporter or secondary antibody. Therefore, the standard curve was instead made of normal (non-fluorescent) BSA and a fluorescently-tagged primary antibody was used to detect and report the protein of interest (**Figure 79**). Surprisingly, using a fluorescently-tagged primary detection antibody did not result in noticeable signal magnification with

100 ng/mL remaining the lowest concentration that yielded a measurable signal. This suggests that analyte was not efficiently captured from the solution.

In a separate experiment, incubation with a fluorescently-labeled detection antibody did reduce the detection limit of the microhydrogels (**Figure 80**). There were two changes between this experiment and the previous experiment. First, the detection antibody was incubated with the microhydrogels for an additional hour (previously incubation was only one hour) while on a shaker-plate. The second difference was the specific BSA used as an analyte. In the first experiment, general lab BSA was used as the analyte and in the second experiment a fresh bottle of BioUltra BSA was purchased. It is possible that these changes contributed to the increased sensitivity; however, this improved detection limit was not observed in a follow-up experiment where the analyte of interest was IFNβ (**Figure 81**). This was surprising because the detection antibody was functionalized with AlexaFluor488, which is a brighter fluorophore than the FITC used in the BSA detection experiments. However, each experiment also used a different set of antibodies. Therefore, a key conclusion is that future experiments should utilize ELISA-tested antibodies for both capture and detection, and a standard curve will be necessary for each individual analyte to determine the extent to which it can be detected. This is similar to the Luminex or ELISA protocols where a standard curve is run with each experiment to account for the antibodies used and the condition of the laser.

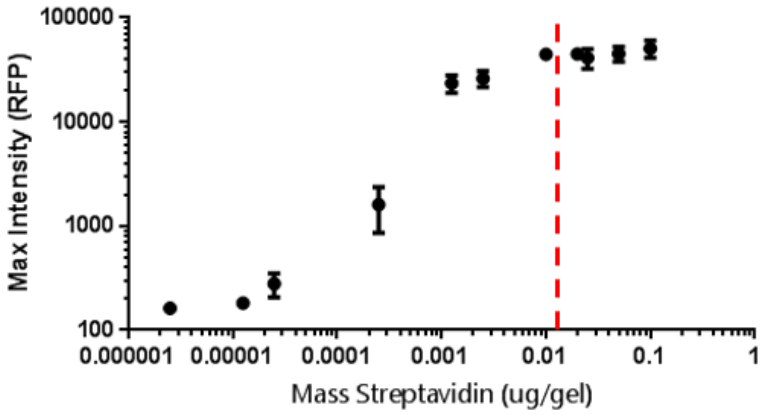

Figure 75 Binding Fluorescent Streptavidin to Microhydrogels
Increasing amounts of streptavidin were incubated with microhydrogels to determine at what mass the microhydrogels' surfaces were saturated.

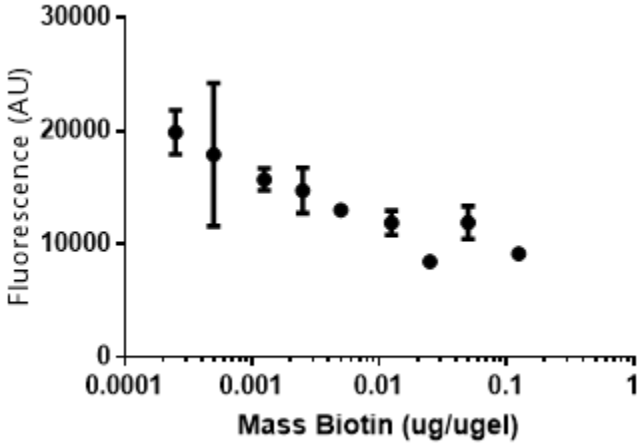

Figure 76 Binding Fluorescent Biotin to Microhydrogels
A similar standard curve was attempted for the subsequent incubation with fluorescently-labeled biotin. By eye, the samples showed increasing deep blue color on the surface of the microhydrogels. However, when the fluorescence was quantified the signal decreased in a surprising manner. Most likely the close proximity of the fluorophores was quenching the emission.

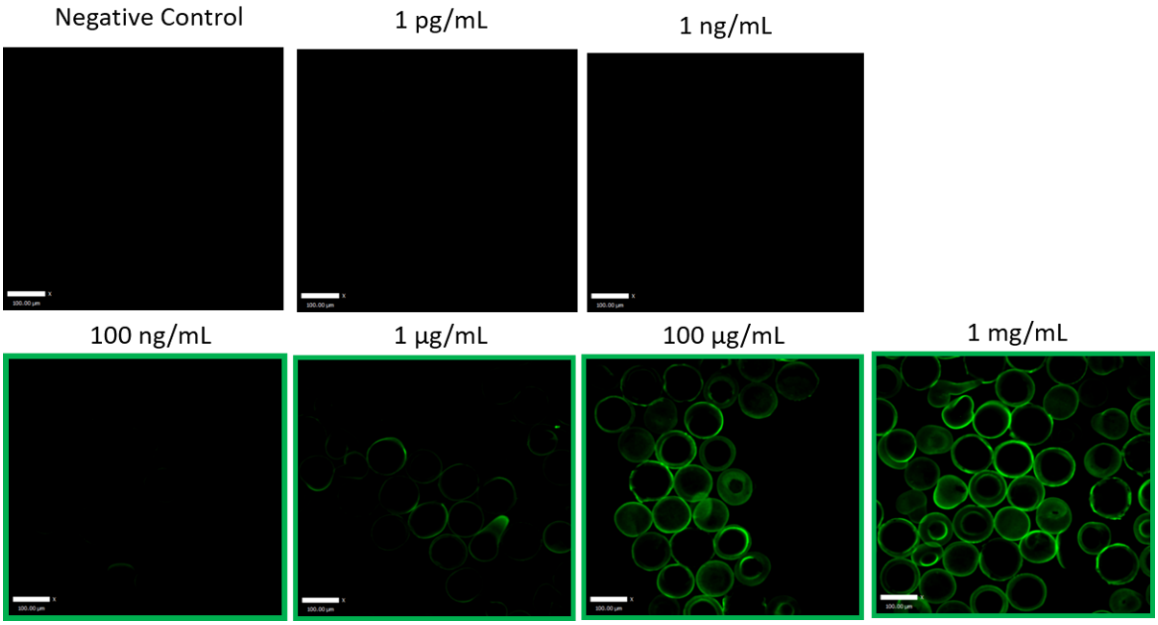

Figure 77 Fluorescently-tagged BSA Standard Curve
Fluorescent BSA could be measured down to a concentration of 100 ng/mL on a spinning disk confocal microscope. Scale bars are 100 µm.

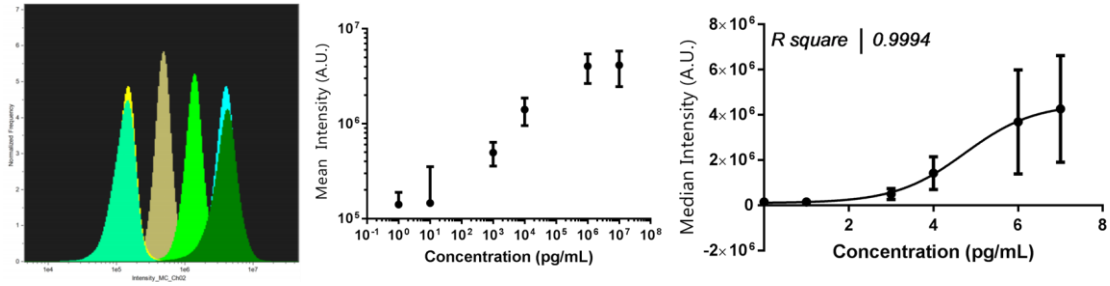

Figure 78 Detection of BSA-AF488 in the ISX
ISX images of microhydrogels with fluorescent BSA were collected for a range of concentrations and quantified to form a standard curve. The averages were fit with a four-parameter dose-response curve.

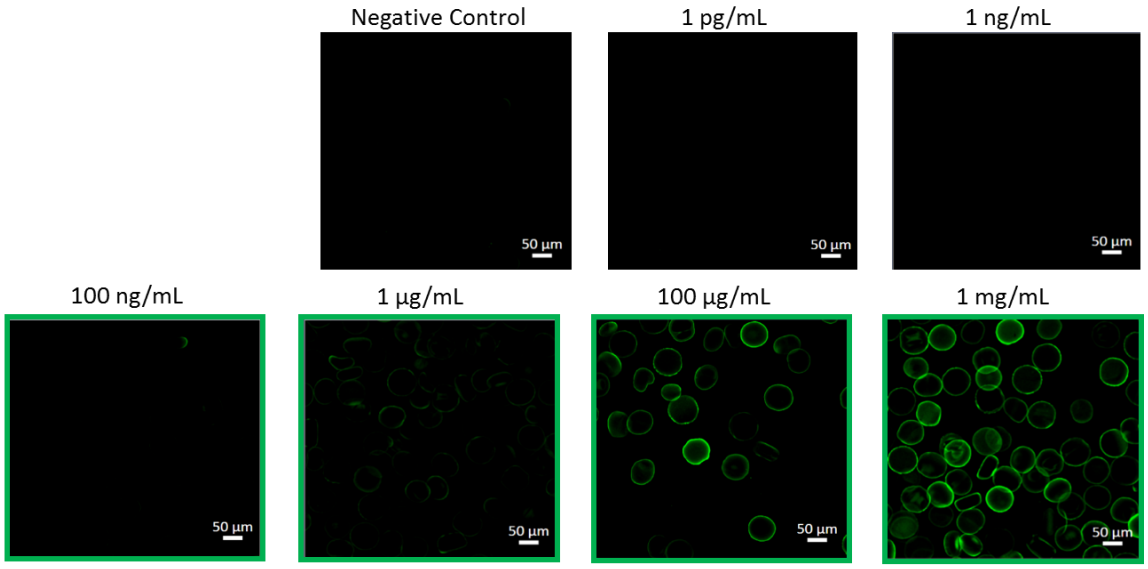

Figure 79 BSA Standard Curve with Fluorescent Detection Antibody
Normal BSA was instead incubated with antibody-functionalized microhydrogels and then detected with FITC-bound antibodies. The detection limit was still 100 ng/mL.

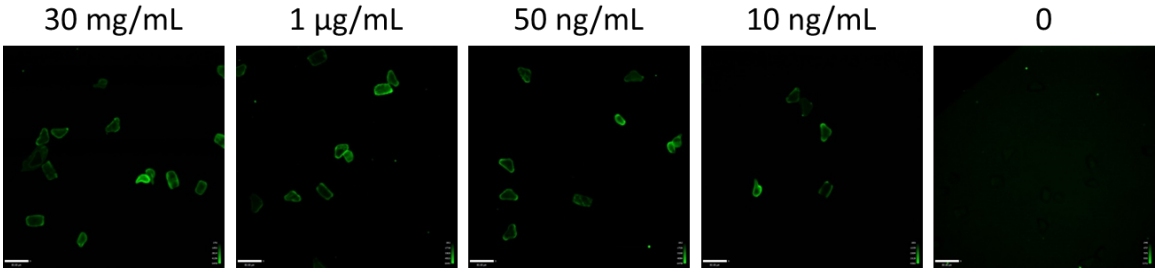

Figure 80 Detection of BioUltra BSA Using Fluorescent Detection Antibodies
In a second BSA detection experiment, two procedural changes resulted in detection at lower concentrations. Note for these images that all were collected at the same laser power but are not graphed on the same fluorescence scale.

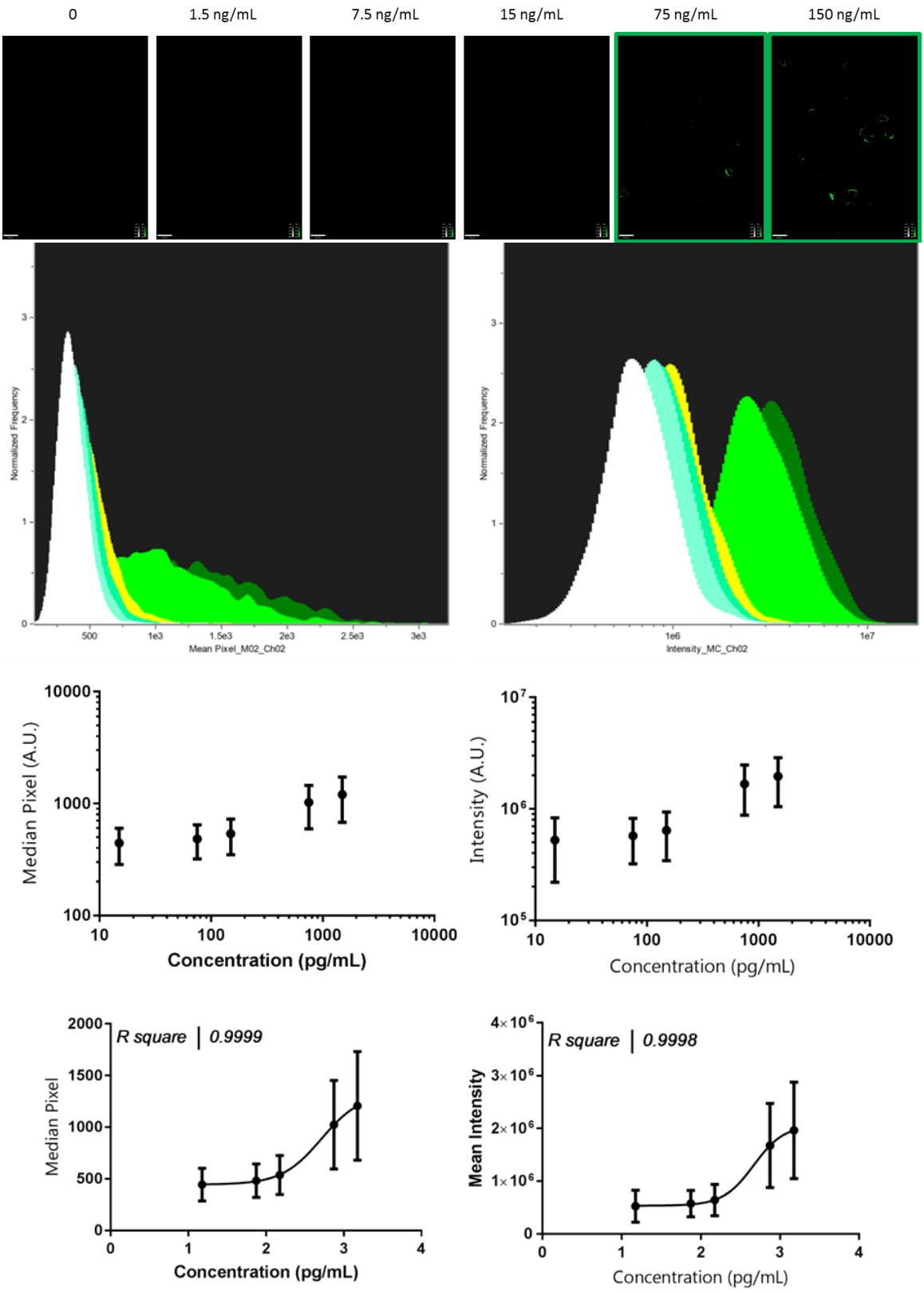
0
1.5 ng/mL
7.5 ng/mL
15 ng/mL
75 ng/mL
150 ng/mL
Normalized Frequency
Mean Pixel_M02_Ch02
Intensity_MC_Ch02
Median Pixel (A.U.)
Concentration (pg/mL)
Intensity (A.U.)
R square | 0.9999
Median Pixel
R square | 0.9998
Mean Intensity

Figure 81 Detection of IFNβ Using Fluorescent Detection Antibodies and the ISX
Using an ELISA protein standard, the microscope detection limit was at best 75 ng/mL (top row) and the ISX (middle row) confirmed that clear separation between groups was only possible for the higher concentrations. In IDEAS, two features (Mean Pixel – left, and Intensity – right) were both analyzed to determine which feature gave greater separation between groups. These data from the ISX were quantified (bottom two rows) for median pixel intensity (left) and intensity (right), and fit with four-parameter dose-response curves.

5.3 Discussion

In this Aim, the base 3DMaC method was modified to serve as a highly multiplexed, high-throughput molecular analytics method. Already microhydrogels have been demonstrated in literature to be useful platforms with which to detect analytes; however, none have matched the ease of use or multiplexing of 3DMaC. In literature, analysis of these microhydrogels has been either slow (requiring manual microscopic analysis, the Koh and Ghosh groups) or required instrumentation that is not commercially available (the microfluidic analysis of the Doyle group). These methods can offer more content during analysis, but are not as high-throughput as flow cytometry analysis.

The most comparable commercially available systems are the ELISA and Luminex technologies. Two key considerations are important for the comparison between these systems and 3DMaC: the potential number of analytes and replicates that can be analyzed at once. Unlike the methods described in literature all of these systems have automated analysis of results. In the ELISA system, the multiplexing is generally restricted to a single analyte and the remainder of the 96-well plate is used for technical and biological replicates. In the Luminex system, the multiplexing can reach 500 analytes and a plate is similarly used to assay replicates. In the 3DMaC method, the multiplexing could potentially reach ~2000 analytes (**Table 2**) and the ISX can also be set-up to read from a 96-well plate. Therefore, this Aim illustrated that the 3DMaC method enables more

highly multiplexed analyte quantification using commercially available technology and automated analysis.

In order to demonstrate 3DMaC's usage as a detection platform, several key fabrication variables were changed. Microhydrogels no longer include cells and so the polymerization conditions do not need to be as carefully tuned. This is beneficial because changing the macromer solution to contain a higher polymer weight percentage and choosing a smaller PEG monomer results in a much stiffer gel. This gel barely swells upon hydration which ensures that the fabricated shape barcodes retain crisp corners and size is a more reliable barcoding variable. This barcode fidelity then enables more shape barcodes to be added to the analysis, a key route by which the multiplexing was increased in this Aim. In the first and second Aims, the barcodes were basic geometric shapes with low perimeter to area ratios to maximize cell encapsulation. However, in this cell-free Aim, the feasible types of shape were expanded to also include shapes with cutout and protruding regions. As the microhydrogel shape diverges more from a cell-like shape, advanced image analysis methods are likely to be more useful than IDEAS-based analysis. In theory, this fabrication and analysis method could also be extended to pattern-based barcoding that would enable even more analytes to be analyzed at once.

The microhydrogels used in this Aim were also smaller than those used in Aim 2 because they did not need to contain cells and lowering the surface area means fewer streptavidin molecules and antibodies are needed to coat the surface while maintaining the same surface density. There is potential to use still smaller hydrogels as detection agents. All studies here were performed using a 20x magnification; however, the ISX is also equipped with a 40x and 60x option. Smaller microhydrogels have the additional benefit

of a slower settling time which means a higher density running buffer is not required for long assay times. This increases the overall throughput of the method.

The other avenue by which multiplexing was increased was the addition of fluorescence barcoding. In the first Aim, fluorescence barcodes were introduced as binary values and demonstrated for a few color combinations. In this Aim, following the methodology used in the Luminex system, fluorescence barcoding was expanded to show different levels of fluorescence within the same detection channel. When combining three levels of intensity across two fluorescence channels, this demonstrates nine potential color combinations. This also necessitated expanding the gating tree to account for fluorescence levels. Using true populations, the throughput and accuracy were calculated for this new tree. Accuracies were high for some groups but not others, which showed that even with compensation there is still need for precise control over fluorophore loading to prevent detectable overlap in the emission spectra. The throughput on these microhydrogels was much higher than for the shape barcodes shown in Aim 1, this is likely because of homogeneous surface labeling with the fluorophores and the relative ease of measuring intensity rather than shape. As all test microhydrogels had the same shape barcode, only a rough shape gate was applied and is not reflected in the accuracy and throughput calculations. With careful titration of the fluorophore incorporation and the addition of more colors, this barcoding variable could be further increased.

One area of further improvement is the functionalization chemistry for the microhydrogels. Specifically, in this Aim the fabrication conditions of the microhydrogels were tuned to maximize particle functionalization to enable protein detection. When using antibodies as capture agents the two key considerations are affinity and avidity. The affinity of the antibody quantifies how tightly an analyte will be

bound by its specific antibody. The binding is not covalent and so binding is thought of as a balance between the time that the analyte is bound and unbound. When using a single capture antibody molecule, there is the possibility that the captured analyte will move away and be lost while in this unbound state. However, many proteins have multiple antigen sites that can be bound to adjacent antibodies. If multiple antibodies capture the analyte, it is unlikely that they will all be in the unbound state at once and so the analyte is less likely to escape. This is called binding avidity. Using the fabrication and antibody conjugation chemistries described in this Aim, the detection limit was found to be between 10 and 100 ng/mL depending on the tested system. In the future, this could be improved by exploring other fabrication chemistries or increasing the volume of the microhydrogel that is accessible to proteins by adding porogens.[19]

CONCLUSIONS AND FUTURE DIRECTIONS

In this dissertation, a new method for high replicate, high-throughput analyses of material-cell interactions was designed and validated. Dubbed 3D Material Cytometry (3DMaC), this method uses flow cytometry to analyze 3D material constructs. The impact on the field can be broadly summarized as follows: (1) An imaging flow cytometer was shown to enable size-, shape-, and fluorescence-barcoding and (2) flow cytometry was used to analyze 3D hydrogel materials rather than suspended cells. In the first Aim, key design choices were made and explained, and the capabilities of the method were quantified. This method was then applied to two different applications of interest: tissue engineering (Aim 2) and molecular analytics (Aim 3). This new method has great potential to contribute to biomaterials studies and is, to the best of our knowledge, the only effort to adapt flow cytometry technology to assay hydrogels. As biological studies increasingly focus on higher sample numbers and reproducibility, methods such as 3DMaC provide a route to adapt existing technology to meet new challenges. Given the impressive ability of the flow cytometer to assay microhydrogels, even though it was designed with cells in mind, 3DMaC opens up many new avenues for flow cytometry-based analysis of biomaterials.

For tissue engineering, there is a need for high-throughput screening of cell-material interactions due to the sheer number of variables that determine efficacy and variability within cell populations. While osteogenesis of MSCs was used as a model system in Aim 2, the method is applicable to many other cell-material systems of interest. Only PEG-based materials were used in this dissertation; but other materials have been microfabricated with shape barcodes (by our group and others). The ability to screen a massive amount of materials in conjunction with different culture conditions is critical to

exploring the design space for biomaterial constructs. This will enable studies to either screen materials for further study or to iterate around a promising material to optimize performance. This iterative process might become especially useful for patient-specific applications since biomaterial implants may require optimization for each patient. 3DMaC also could contribute greatly to bench research by screening materials on the microscale to select materials for more expensive full testing.

To use 3DMaC for other materials, it is important to consider which fabrication methods could be used to generate the microhydrogels. In this dissertation, UV-initiated chain polymerization was used, but other methods may offer alternative fabrication advantages. The PDMS micromolding method used here is most favorable for less viscous materials with user-controlled or slower crosslinking methods. The viscosity is important because monomer solution will coat the PDMS mold surface in contact with the hydrophobic surface and this layer can be minimized at lower viscosities. At higher viscosities, it might be possible to use doctor-blading to remove this layer, but the PDMS mold would need to be made deeper to compensate for any material stripped from the wells. PDMS is UV-transparent which was convenient for the crosslinking used here, but the same polymerization could be achieved using a visible light crosslinking. For example, using Eosin Y as a photoinitiator could result in higher viability due to the absence of UV and the resulting background green fluorescence might improve barcoding. A time-dependent crosslinking, such as a Michael addition reaction between thiol and acrylate or maleimide groups, should also work well with PDMS micromolding. In this case, monomers would be mixed at the appropriate pH, sealed into molds, and allowed to sit until crosslinking was complete. The acrylate/thiol system is probably more promising because these reactions are slower than maleimide/thiol reactions which should result in a more

homogeneous polymer network. These crosslinking reactions are also favorable because the same peptide incorporation demonstrated in this dissertation can be used.

Moving away from the PDMS micromolding, spincoating monomer is a good alternative because the spincoating method readily accommodates more viscous materials. However, this method requires that photopolymerization be used to mold the microhydrogels. Microfluidic fabrication methods are flexible and clever design might allow for a variety of polymerization methods to be used. But, in general, these methods are lower throughput than the molding methods because they are a continuous fabrication process that needs to run for a long time to generate large numbers.

When expanding this method to other materials, there are key parameters to keep in mind. When changing between the PEGDA and PEG-4NB/DTT chemistries, the increased swelling resulted in microhydrogels with less contrast. This made identification of the barcode more difficult using the ISX and barcode visibility needs to be considered for each material used. Most materials could be stained by incorporating a small amount of fluorescence (for example, by conjugating a fluorophore to the backbone or a subset of endgroups before crosslinking) and this staining may make boundaries more identifiable. The elasticity of the materials also needs to be considered due to the mechanical constraints of flow cytometry. The machines are designed to pick up cells in the fluidics system; cells are relatively fragile but also much smaller relative to the apertures. The materials used in this dissertation were relatively stiff and robust compared to cells and barcodes observed before flow were similar to those seen in the ISX images. However, applying 3DMaC to softer materials might be difficult if any of the forces related to sample pick-up result in deformation.

Another key improvement would be improving the degree of control over the number of cells in each individual microhydrogel. In this dissertation, cell numbers were only roughly controlled by the starting cell concentration in the monomer solution and the result was a distribution of cell numbers in the microhydrogels. This led to several challenges. The first was that the cells were distributed through the volume of the microhydrogel. The microhydrogels used in this dissertation were relatively small compared to the size of a human cell and so in many cases the cell could reach the exterior of a microhydrogel. An edge-based cell often would not adhere sufficiently to the microhydrogel (such that it was lost during culture or staining), or bind to culture plastics or cells on other microhydrogels. Also, even if a cell remained at the exterior of a microhydrogel, often it would result in a slight protrusion that altered the shape-based masking and reduced the accuracy of the sorting tree. These cell-inclusion issues were among the greatest reasons for loss of replicates before or during analysis.

The second challenge was that multiple cells in a microhydrogel will interact with the surrounding material differently compared to when there is a single cell. If there are multiple cells in a microhydrogel, the biological situation being investigated is likely to be different than if there were only one. This is because the cells may communicate via chemical signals or be close enough to physically interact. In this dissertation, the goal was to study material-directed stem cell differentiation and so limiting cell-cell contact was important. This is especially true for the hypothesis described in Aim 2 because the HAVDI peptide was incorporated to mimic cell-cell contact and any other contact affects the testing.

Without reproducible cell numbers and cell placement in the microhydrogels, it is difficult to ensure that there are no artifacts in the data analysis. These artifacts could

include the mis-identified shape barcodes and also signal detection limitations. As described in Aim 2, cells could be stacked on top of each other in the microhydrogels but the analysis is performed on 2D images so some signal could be hidden. This is possible for brightfield intensity detection and fluorescence. Some of this might be resolved by using the extended depth of field function available on some imaging flow cytometers. However, this does not address artifacts that might arise from the distance between the microhydrogel and the detectors. Because the detection is microscope-based, it is important to consider the plane of detection because out-of-plane signals will be weaker. While the ISX adjusts keep images in focus, the movement is not sufficient to capture the range over which the microhydrogels drift. In the first Aim, the microhydrogels were thin relative to the cross-sectional area which helped reduce microhydrogel tumbling during analysis. However, once cells were included the microhydrogels needed to be thicker to fully incorporate the cells so tumbling increased. Once the volume of the microhydrogels increased, the microhydrogels were a more significant disruption of the flow profile and so cells were not always in the same plane during analysis.

Fixing this problem could be approached in two ways: controlling the cells or controlling the flow. Controlling the flow would require dramatic changes to the flow cytometer, including the size of the microfluidics, and is beyond the scope of this work. However, there could be improvements made to the microhydrogels that might improve the analysis efficiency and cell incorporation. Microhydrogels should be made of minimal thickness necessary and one axis should be elongated to help align with the direction of flow. Fluorescence barcoding also should be tested for cell-containing microhydrogels to explore the impact of 3D shape on cell behaviors. The fabrication method could also be improved to control cell numbers. This would likely be achievable using a microfluidic method to place a desired cell number in each microhydrogel before crosslinking. It also

might be possible to use direct-write methods to crosslink a microhydrogel around a cell cluster of the correct size. Microhydrogels could also be crosslinked first just as a tiny shape-irrelevant cell-containing hydrogel and then the shape-barcoded microhydrogel crosslinked around this cluster.

Rather than controlling the cell number before fabrication, the microhydrogels could also be sorted depending on the number of encapsulated cells. For example, this might mean staining all the cells with a CellTrace dye and then using a FACS system to sort microhydrogels based on intensity to collect populations with roughly the same number of cells per microhydrogel. In the case of the mineralized microhydrogels, the differences in density between the different microhydrogels mean that they could potentially be separated using a density gradient.

For molecular analytics, there is a need to increase the number of analytes that can be detected at once and in Aim 3 3DMaC was shown to be a promising way to measure a large number of analytes using SSF barcoded particles. Compared to existing methods in literature or those commercially available, 3DMaC offers potentially the fastest way to assay the largest number of analytes in a single test. Before this can be achieved using the 3DMaC system, there are a few improvements that need to be made. First is increasing the number of barcodes that can be detected simultaneously. This dissertation showed a maximum of ten shapes, three sizes, and nine fluorescence barcodes but there is potential to include more. Also, it will be important to test the barcoding variables in combination to prove that they do not result in any detection artifacts and truly can be multiplexed together.

Second, 3DMaC detection needs to be improved to be able to detect lower amounts of analyte and to have less variability. The analyte detection limit is tied to the amount of analyte that is bound to the microhydrogels. This dissertation focused on maximizing microhydrogel functionalization, but more incubation conditions and times could be investigated to maximize analyte binding and then detection. This method is not designed to give rapid information and so longer times could be tested to try to capture more protein from solution.

Currently, 3DMaC detection shows more variability than is desirable. This is apparent in the detection profiles from Aim 3 where even for the standard curves there is large variability at each concentration. While the means could be accurately fit using a four-parameter dose-response curve, the range at each concentration was large. This is likely because the signal is being detected over the area of the microhydrogel and this area changes for each event, which suggests that a normalization factor could be selected to control for this variation or that a strict shape gate could be drawn to limit variability. Another option would be to refine the fluorescence masking to only incorporate the exterior of the microhydrogel. It is also possible that this range comes from the fluorescence reporters used to label the analyte. The number of analytes and the number of fluorophores per detection antibody can vary which means the signal will be more variable between microhydrogels. This could be controlled for by using well-defined detection antibodies or by standardizing against a set of calibration beads. Such improvements to the signal variability are important because ideally the method would use a minimal number of microhydrogels to detect since this will use less supply material and let a larger number of microhydrogels be scanned in the assay period.

As technology improves, there is the potential for 3DMaC to be useful for additional problems and situations. Within the two applications demonstrated here, both will benefit from advanced optics and image analysis methods that enable the classification of a larger number of shape barcodes to expand the number of conditions that can be measured at once. The flexibility of imaging cytometers to detect bright-field and fluorescence channels means that there is great potential to measure differentiation or other cellular responses using existing reporter technologies. This would make the technique useful for analyzing a wide range of cell-material interactions. For molecular analytics, many different types of barcoded particles have been developed to report on many different analytes of interest. In addition to the particles and methods developed here, many existing technologies are compatible with 3DMaC analysis and there are improvements that could be made to sensitivity as well.

There are also a large number of potential areas of research where 3DMaC could be applied in its present state. Broadly divided into cell-based and sensing applications, these possible applications leverage the imaging flow cytometer to enable high-throughput, high replicate studies of biomaterials. Among the cellular applications, this dissertation has discussed primarily the ability to study the response of cells to an encapsulating material. It is important to note the diversity of cell types and biomaterials currently being researched, many of which could be converted to 3DMaC studies without large changes in material or end-point assay. However, there are many more applications to consider. The barcoding method in this dissertation need not be restricted to material composition or analyte specificity. Instead the barcode could denote a specific media composition or drug screening combination.

There is also room for studies of how 3D shape and size relate to cell behavior. Studies could be expanded to include co-culture conditions that are of high importance for understanding how multiple cell types interact *in vivo*. This encompasses studies of multiple cell types in a single microhydrogel (for example, modeling tumor microenvironment with immune and tumor cells) and also cases where the barcode designates the type of encapsulated cell. In the latter cases, this could be used to study how cellular populations affect one another through chemical signals when each cell type is constrained to a particular material environment. This last point is particularly important for tissue engineering applications as cells encapsulated in a transplanted biomaterial will need to contend with the response from immune cells on the periphery of the implant. All of these cell-based applications can be further studied in the 3DMaC system to acquire high replicate, high-throughput data. One particular advantage of 3DMaC is that, in its current implementation, a massive number of replicates are cultured in suspension in aggregate and this population can be sampled at multiple timepoints to track progress and obtain longitudinal data. Particularly for clinical and cell manufacturing-related applications, this sampling could be important for maintaining quality metrics.

3DMaC could also contribute to a large number of non-cell-based studies. Already, many groups have shown that microhydrogels (or other microparticles) can be used for detection studies, but these studies lack an easily accessible, rapid assay system. In this case, the main advantage of 3DMaC is not that it is high replicate (though this is still advantageous for quantifying population averages), but that it offers large multiplexing in high-throughput. This dissertation showed how microhydrogels functionalized for a sandwich immunoassay could be analyzed using 3DMaC with increased barcode numbers. 3DMaC could also be used to measure changes in shape in response to stimuli,

as described in the Background of this dissertation. For example, rather than using antibodies, a molecularly imprinted system could be used where a binding event is measured via a resulting change in size. In this case, multiplexing would be achieved with shape and fluorescence, which already offer the greatest number of potential barcodes. Another possibility would be to fabricate microhydrogels where the barcode designates a particular crosslinker susceptible to degradation. For example, microhydrogels could be crosslinked with peptides and then exposed to solutions that may contain particular enzymes. Microhydrogels whose peptide could be cleaved by those enzymes would then be dissolved and 3DMaC could identify the enzymes via the absence of that barcode during analysis. These are only a few examples of how high-throughput analysis of microparticles might contribute to sensing studies; 3DMaC does not necessarily need to be restricted to microhydrogels and other microparticles could be analyzed with slight experimental accommodations.

Finally, if SSF barcodes could be determined for a non-imaging flow cytometer, this method would be accessible to many more researchers. This would also enable FACS methods to be used to collect specific microhydrogels for further study which would greatly increase the data that could be obtained. It is also possible that imaging flow cytometers such as the ISX might be upgraded such that populations of interest could be collected thus enabling collection using existing gating methods shown here. One of the biggest advantages of 3DMaC is that the method is designed for use with existing flow cytometers and does not require specialized equipment. Taken together, this dissertation and all of these future possibilities prove that 3DMaC can increase the utility and applications of flow cytometry by bringing its advantages to bear on current questions in the field of biomaterials.

REFERENCES

1. D. F. Williams, *Biomaterials*, 2009, **30**, 5897-5909.
2. B. D. Ratner, A. S. Hoffman, F. J. Schoen and J. E. Lemons, eds., *Biomaterials Science: An Introduction to Materials in Medicine*, Elsevier Academic Press, 2004.
3. Science Education - Biomaterials, https://www.nibib.nih.gov/science-education/science-topics/biomaterials, (accessed May 5th, 2018, 2018).
4. Science Education - Sensors, https://www.nibib.nih.gov/science-education/science-topics/sensors, (accessed May 5th, 2018, 2018).
5. S. Yang, K. F. Leong, Z. Du and C. K. Chua, *Tissue engineering*, 2001, **7**, 679-689.
6. M. J. Lysaght, A. Jaklenec and E. Deweerd, *Tissue Eng Part A*, 2008, **14**, 305-315.
7. L. G. Halsey, D. Curran-Everett, S. L. Vowler and G. B. Drummond, *Nat Methods*, 2015, **12**, 179-185.
8. M. B. Elowitz, A. J. Levine, E. D. Siggia and P. S. Swain, *Science*, 2002, **297**, 1183-1186.
9. K. S. Button, J. P. Ioannidis, C. Mokrysz, B. A. Nosek, J. Flint, E. S. Robinson and M. R. Munafo, *Nat Rev Neurosci*, 2013, **14**, 365-376.
10. Organ Procurement and Transplantation Network, (accessed May 9th, 2016).
11. M. P. Lutolf and J. A. Hubbell, *Nat Biotech*, 2005, **23**, 47-55.
12. F. Brandl, F. Sommer and A. Goepferich, *Biomaterials*, 2007, **28**, 134-146.
13. D. J. Prockop, *Science*, 1997, **276**, 71-74.

14. L. H. Nguyen, A. K. Kudva, N. L. Guckert, K. D. Linse and K. Roy, *Biomaterials*, 2011, **32**, 1327-1338.

15. L. H. Nguyen, A. K. Kudva, N. S. Saxena and K. Roy, *Biomaterials*, 2011, **32**, 6946-6952.

16. K. Parratt, M. Smerchansky, Q. Stiggers and K. Roy, *Journal of Materials Chemistry B*, 2017, **5**, 6237-6248.

17. E. Gomez-Barrena, P. Rosset, D. Lozano, J. Stanovici, C. Ermthaller and F. Gerbhard, *Bone*, 2015, **70**, 93-101.

18. D. Wang and S. Bodovitz, *Trends Biotechnol*, 2010, **28**, 281-290.

19. M. A. Al-Ameen, J. Li, D. G. Beer and G. Ghosh, *Analyst*, 2015, **140**, 4530-4539.

20. Chapter 2 - Types of ELISA, https://www.bio-rad-antibodies.com/elisa-types-direct-indirect-sandwich-competition-elisa-formats.html#Sandwich, (accessed June 27, 2018, 2018).

21. xMAP® Technology, https://www.luminexcorp.com/research/our-technology/xmap-technology/, (accessed June 28, 2018, 2018).

22. ELISpot Assay Principle, https://www.rndsystems.com/products/elispot-assay-principle, (accessed June 28, 2018, 2018).

23. R. Agarwal, V. Singh, P. Jurney, L. Shi, S. V. Sreenivasan and K. Roy, *ACS Nano*, 2012, **6**, 2524-2531.

24. M. Caldorera-Moore, M. K. Kang, Z. Moore, V. Singh, S. V. Sreenivasan, L. Shi, R. Huang and K. Roy, *Soft Matter*, 2011, **7**, 2879.

25. L. C. Glangchai, M. Caldorera-Moore, L. Shi and K. Roy, *J Control Release*, 2008, **125**, 263-272.

26. R. M. Nerem and A. Sambanis, *Tissue engineering*, 1995, **1**, 3-13.

27. A. H. Reddi, *Tissue engineering*, 2000, **6**, 351-359.

28. J. L. Drury and D. J. Mooney, *Biomaterials*, 2003, **24**, 4337-4351.

29. J. A. Hubbell, *Biotechnology (N Y)*, 1995, **13**, 565-576.

30. M. W. Tibbitt and K. S. Anseth, *Biotechnol Bioeng*, 2009, **103**, 655-663.

31. M. C. Cushing and K. S. Anseth, *Science*, 2007, **316**, 1133-1134.

32. J. L. Ifkovits and J. A. Burdick, *Tissue engineering*, 2007, **13**, 2369-2385.

33. G. Odian, in *Principles of Polymerization*, John Wiley & Sons, Inc., Hoboken, New Jersey, Fourth edn., 2004, vol. 1, ch. 3, pp. 198-346.

34. B. D. Fairbanks, M. P. Schwartz, C. N. Bowman and K. S. Anseth, *Biomaterials*, 2009, **30**, 6702-6707.

35. E. S. Place, N. D. Evans and M. M. Stevens, *Nat Mater*, 2009, **8**, 457-470.

36. J. S. Temenoff and A. G. Mikos, *Biomaterials*, 2000, **21**, 2405-2412.

37. D. E. Discher, P. Janmey and Y.-l. Wang, *Science*, 2005, **310**, 1139.

38. A. J. Engler, S. Sen, H. L. Sweeney and D. E. Discher, *Cell*, 2006, **126**, 677-689.

39. I. D. Learmonth, C. Young and C. Rorabeck, *Lancet*, 2007, **370**, 1508-1519.

40. L. E. Bertassoni, M. Cecconi, V. Manoharan, M. Nikkhah, J. Hjortnaes, A. L. Cristino, G. Barabaschi, D. Demarchi, M. R. Dokmeci, Y. Yang and A. Khademhosseini, *Lab on a Chip*, 2014, **14**, 2202-2211.

41. B. Kolesky David, L. Truby Ryan, A. S. Gladman, A. Busbee Travis, A. Homan Kimberly and A. Lewis Jennifer, *Advanced Materials*, 2014, **26**, 3124-3130.

42. J. A. Whisler, M. B. Chen and R. D. Kamm, *Tissue Eng Part C Methods*, 2014, **20**, 543-552.

43. J. S. Jeon, S. Bersini, J. A. Whisler, M. B. Chen, G. Dubini, J. L. Charest, M. Moretti and R. D. Kamm, *Integrative Biology*, 2014, **6**, 555-563.

44. J. D. Bryers, *Biotechnol Bioeng*, 2008, **100**, 1-18.

45. D. Campoccia, L. Montanaro and C. R. Arciola, *Biomaterials*, 2006, **27**, 2331-2339.

46. J. A. Burdick and K. S. Anseth, *Biomaterials*, 2002, **23**, 4315-4323.

47. A. Atala, F. K. Kasper and A. G. Mikos, *Sci Transl Med*, 2012, **4**, 160rv112.

48. J. A. Burdick and G. Vunjak-Novakovic, *Tissue Eng Part A*, 2009, **15**, 205-219.

49. F. H. Chen, K. T. Rousche and R. S. Tuan, *Nat Clin Pract Rheumatol*, 2006, **2**, 373-382.

50. J. S. Temenoff and A. G. Mikos, *Biomaterials*, 2000, **21**, 431-440.

51. C. A. Poole, *Journal of Anatomy*, 1997, **191**, 1-13.

52. B. Sharma and J. H. Elisseeff, *Ann Biomed Eng*, 2004, **32**, 148-159.

53. D. J. Huey, J. C. Hu and K. A. Athanasiou, *Science*, 2012, **338**, 917-921.

54. T. K. Kim, B. Sharma, C. G. Williams, M. A. Ruffner, A. Malik, E. G. McFarland and J. H. Elisseeff, *Osteoarthritis Cartilage*, 2003, **11**, 653-664.

55. B. T. Estes, B. O. Diekman, J. M. Gimble and F. Guilak, *Nat Protoc*, 2010, **5**, 1294-1311.

56. T. Karimi, D. Barati, O. Karaman, S. Moeinzadeh and E. Jabbari, *Integr Biol (Camb)*, 2015, **7**, 112-127.

57. S. Moeinzadeh, S. R. Pajoum Shariati and E. Jabbari, *Biomaterials*, 2016, **92**, 57-70.

58. S. B. Anderson, C. C. Lin, D. V. Kuntzler and K. S. Anseth, *Biomaterials*, 2011, **32**, 3564-3574.

59. S. L. Vega, M. Kwon, R. L. Mauck and J. A. Burdick, *Ann Biomed Eng*, 2016, **44**, 1921-1930.

60. R. L. Mauck, S. B. Nicoll, S. L. Seyhan, G. A. Ateshian and C. T. Hung, *Tissue engineering*, 2004, **9**, 597-611.

61. N. J. Steinmetz, E. A. Aisenbrey, K. K. Westbrook, H. J. Qi and S. J. Bryant, *Acta Biomater*, 2015, **21**, 142-153.

62. N. J. Steinmetz and S. J. Bryant, *Acta Biomater*, 2011, **7**, 3829-3840.

63. I. Villanueva, S. K. Gladem, J. Kessler and S. J. Bryant, *Matrix Biol*, 2010, **29**, 51-62.

64. S. C. Tran, A. J. Cooley and S. H. Elder, *Biotechnol Bioeng*, 2011, **108**, 1421-1429.

65. E. G. Lima, L. Bian, K. W. Ng, R. L. Mauck, B. A. Byers, R. S. Tuan, G. A. Ateshian and C. T. Hung, *Osteoarthritis Cartilage*, 2007, **15**, 1025-1033.

66. A. Mohyeldin, T. Garzon-Muvdi and A. Quinones-Hinojosa, *Cell Stem Cell*, 2010, **7**, 150-161.

67. D. Loessner, K. S. Stok, M. P. Lutolf, D. W. Hutmacher, J. A. Clements and S. C. Rizzi, *Biomaterials*, 2010, **31**, 8494-8506.

68. M. M. Caron, P. J. Emans, M. M. Coolsen, L. Voss, D. A. Surtel, A. Cremers, L. W. van Rhijn and T. J. Welting, *Osteoarthritis Cartilage*, 2012, **20**, 1170-1178.

69. K. von der Mark, T. Kirsch, A. Nerlich, A. Kuss, G. Weseloh, K. Gluckert and H. Stoss, *Arthritis Rheum*, 1992, **35**, 806-811.

70. S. A. Bencherif, A. Srinivasan, F. Horkay, J. O. Hollinger, K. Matyjaszewski and N. R. Washburn, *Biomaterials*, 2008, **29**, 1739-1749.

71. M. F. Tsai, H. Y. Tsai, Y. S. Peng, L. F. Wang, J. S. Chen and S. C. Lu, *J Biomed Mater Res A*, 2008, **84**, 727-739.

72. R. K. Korhonen, M. S. Laasanen, J. Toyras, J. Rieppo, J. Hirvonen, H. J. Helminen and J. S. Jurvelin, *J Biomech*, 2002, **35**, 903-909.

73. Y. J. Choi, T. G. Kim, J. Jeong, H. G. Yi, J. W. Park, W. Hwang and D. W. Cho, *Adv Healthc Mater*, 2016, **5**, 2636-2645.

74. S. Rhee, J. L. Puetzer, B. N. Mason, C. A. Reinhart-King and L. J. Bonassar, *ACS Biomaterials Science & Engineering*, 2016, **2**, 1800-1805.

75. K. T. Nguyen and J. L. West, *Biomaterials*, 2002, **23**, 4307-4314.

76. J. Friedrich, C. Seidel, R. Ebner and L. A. Kunz-Schughart, *Nat Protoc*, 2009, **4**, 309-324.

77. D. Barbone, T. M. Yang, J. R. Morgan, G. Gaudino and V. C. Broaddus, *J Biol Chem*, 2008, **283**, 13021-13030.

78. B. M. Baker and C. S. Chen, *Journal of Cell Science*, 2012, **125**, 3015.

79. K. Murphy, ed., *Janeway's Immunobiology*, Garland Science, 2012.

80. A. I. Caplan, *Tissue Eng Part A*, 2010, **16**, 2415-2417.

81. A. I. Caplan, *Stem Cells Translational Medicine*, 2017, **6**, 1445-1451.

82. D. G. Phinney and D. J. Prockop, *Stem Cells*, 2007, **25**, 2896-2902.

83. M. Dominici, K. Le Blanc, I. Mueller, I. Slaper-Cortenbach, F. Marini, D. Krause, R. Deans, A. Keating, D. Prockop and E. Horwitz, *Cytotherapy*, 2006, **8**, 315-317.

84. A. Uccelli, L. Moretta and V. Pistoia, *Nat Rev Immunol*, 2008, **8**, 726-736.

85. Achieving large-scale, cost-effective, reproducible manufacturing of high-quality cells: A technology roadmap to 2025., http://www.cellmanufacturingusa.org/sites/default/files/NCMC_Roadmap_021816_high_res-2.pdf, (accessed June 22, 2018, 2018).

86. J. C. Reichert and D. W. Hutmacher, in *Tissue Engineering: From Lab to Clinic*, eds. N. Pallua and C. V. Suscheck, Springer Berlin Heidelberg, Berlin, Heidelberg, 2011, DOI: 10.1007/978-3-642-02824-3_21, pp. 431-456.

87. M. R. Nelson and K. Roy, *Journal of Materials Chemistry B*, 2016, **4**, 3490-3503.

88. V. D. Roobrouck, F. Ulloa-Montoya and C. M. Verfaillie, *Experimental Cell Research*, 2008, **314**, 1937-1944.

89. P. M. Mountziaris, P. P. Spicer, F. K. Kasper and A. G. Mikos, *Tissue Eng Part B Rev*, 2011, **17**, 393-402.

90. L. Claes, S. Recknagel and A. Ignatius, *Nat Rev Rheumatol*, 2012, **8**, 133-143.

91. S. Weiner and H. D. Wagner, *Annual Review of Materials Science*, 1998, **28**, 271-298.

92. A. M. Kloxin, J. A. Benton and K. S. Anseth, *Biomaterials*, 2010, **31**, 1-8.

93. O. Chaudhuri, L. Gu, D. Klumpers, M. Darnell, S. A. Bencherif, J. C. Weaver, N. Huebsch, H.-p. Lee, E. Lippens, G. N. Duda and D. J. Mooney, *Nature Materials*, 2015, **15**, 326.

94. K. S. Anseth, V. R. Shastri and R. Langer, *Nat Biotechnol*, 1999, **17**, 156-159.

95. B. Geiger, J. P. Spatz and A. D. Bershadsky, *Nat Rev Mol Cell Biol*, 2009, **10**, 21-33.

96. C. S. Chen, J. Tan and J. Tien, *Annu Rev Biomed Eng*, 2004, **6**, 275-302.

97. L. C. Palmer, C. J. Newcomb, S. R. Kaltz, E. D. Spoerke and S. I. Stupp, *Chem Rev*, 2008, **108**, 4754-4783.

98. Medtronic, INFUSE Bone Graft, http://www.medtronic.com/us-en/healthcare-professionals/products/spinal-orthopaedic/bone-grafting/infuse-bone-graft.html, (accessed April 28th 2018).

99. FDA, *Journal*, 2005.

100. D. S. Benoit, M. P. Schwartz, A. R. Durney and K. S. Anseth, *Nat Mater*, 2008, **7**, 816-823.

101. C. N. Salinas and K. S. Anseth, *J Tissue Eng Regen M*, 2008, **2**, 296-304.

102. D. L. Hern and J. A. Hubbell, *J Biomed Mater Res*, 1998, **39**, 266-276.

103. C. N. Salinas and K. S. Anseth, *Biomaterials*, 2008, **29**, 2370-2377.

104. A. M. Kloxin, A. M. Kasko, C. N. Salinas and K. S. Anseth, *Science*, 2009, **324**, 59-63.

105. A. E. Rydholm, N. L. Held, D. S. Benoit, C. N. Bowman and K. S. Anseth, *J Biomed Mater Res A*, 2008, **86**, 23-30.

106. M. S. Hahn, J. S. Miller and J. L. West, *Advanced Materials*, 2006, **18**, 2679-2684.

107. B. D. Cosgrove, K. L. Mui, T. P. Driscoll, S. R. Caliari, K. D. Mehta, R. K. Assoian, J. A. Burdick and R. L. Mauck, *Nat Mater*, 2016, **15**, 1297-1306.

108. A. M. Delise and R. S. Tuan, *Dev Dyn*, 2002, **225**, 195-204.

109. M. Zhu, S. Lin, Y. Sun, Q. Feng, G. Li and L. Bian, *Biomaterials*, 2016, **77**, 44-52.

110. S. N. Bhatia and D. E. Ingber, *Nat Biotechnol*, 2014, **32**, 760-772.

111. D. Huh, D. C. Leslie, B. D. Matthews, J. P. Fraser, S. Jurek, G. A. Hamilton, K. S. Thorneloe, M. A. McAlexander and D. E. Ingber, *Science Translational Medicine*, 2012, **4**, 159ra147.

112. S. Chung, R. Sudo, P. J. Mack, C. R. Wan, V. Vickerman and R. D. Kamm, *Lab Chip*, 2009, **9**, 269-275.

113. L. M. Griep, F. Wolbers, B. de Wagenaar, P. M. ter Braak, B. B. Weksler, I. A. Romero, P. O. Couraud, I. Vermes, A. D. van der Meer and A. van den Berg, *Biomed Microdevices*, 2013, **15**, 145-150.

114. S. H. Nam, H. J. Lee, K. J. Son and W. G. Koh, *Biomicrofluidics*, 2011, **5**, 32001-3200110.

115. Y. Du, E. Lo, S. Ali and A. Khademhosseini, *Proc Natl Acad Sci U S A*, 2008, **105**, 9522-9527.

116. F. Yanagawa, H. Kaji, Y. H. Jang, H. Bae, D. Yanan, J. Fukuda, H. Qi and A. Khademhosseini, *J Biomed Mater Res A*, 2011, **97**, 93-102.

117. P. Panda, S. Ali, E. Lo, B. G. Chung, T. A. Hatton, A. Khademhosseini and P. S. Doyle, *Lab Chip*, 2008, **8**, 1056-1061.

118. J. Yeh, Y. Ling, J. M. Karp, J. Gantz, A. Chandawarkar, G. Eng, J. Blumling, 3rd, R. Langer and A. Khademhosseini, *Biomaterials*, 2006, **27**, 5391-5398.

119. G. T. Franzesi, B. Ni, Y. Ling and A. Khademhosseini, *J Am Chem Soc*, 2006, **128**, 15064-15065.

120. H. Tekin, M. Anaya, M. D. Brigham, C. Nauman, R. Langer and A. Khademhosseini, *Lab Chip*, 2010, **10**, 2411-2418.

121. Y. Mei, K. Saha, S. R. Bogatyrev, J. Yang, A. L. Hook, Z. I. Kalcioglu, S. W. Cho, M. Mitalipova, N. Pyzocha, F. Rojas, K. J. Van Vliet, M. C. Davies, M. R. Alexander, R. Langer, R. Jaenisch and D. G. Anderson, *Nat Mater*, 2010, **9**, 768-778.

122. D. G. Anderson, S. Levenberg and R. Langer, *Nat Biotechnol*, 2004, **22**, 863-866.

123. D. G. Anderson, D. Putnam, E. B. Lavik, T. A. Mahmood and R. Langer, *Biomaterials*, 2005, **26**, 4892-4897.

124. C. J. Flaim, S. Chien and S. N. Bhatia, *Nat Methods*, 2005, **2**, 119-125.

125. D. R. Albrecht, G. H. Underhill, T. B. Wassermann, R. L. Sah and S. N. Bhatia, *Nat Methods*, 2006, **3**, 369-375.

126. M. E. Todhunter, N. Y. Jee, A. J. Hughes, M. C. Coyle, A. Cerchiari, J. Farlow, J. C. Garbe, M. A. LaBarge, T. A. Desai and Z. J. Gartner, *Nat Methods*, 2015, **12**, 975-981.

127. M. Gruene, M. Pflaum, C. Hess, S. Diamantouros, S. Schlie, A. Deiwick, L. Koch, M. Wilhelmi, S. Jockenhoevel, A. Haverich and B. Chichkov, *Tissue Eng Part C Methods*, 2011, **17**, 973-982.

128. A. Dolatshahi-Pirouz, M. Nikkhah, A. K. Gaharwar, B. Hashmi, E. Guermani, H. Aliabadi, G. Camci-Unal, T. Ferrante, M. Foss, D. E. Ingber and A. Khademhosseini, *Scientific reports*, 2014, **4**, 3896.

129. S. L. Vega, M. Kwon, R. L. Mauck and J. A. Burdick, *Annals of Biomedical Engineering*, 2016, **44**, 1921-1930.

130. M. E. Todhunter, N. Y. Jee, A. J. Hughes, M. C. Coyle, A. Cerchiari, J. Farlow, J. C. Garbe, M. A. LaBarge, T. A. Desai and Z. J. Gartner, *Nat Meth*, 2015, **12**, 975-981.

131. D. R. Bandura, V. I. Baranov, O. I. Ornatsky, A. Antonov, R. Kinach, X. Lou, S. Pavlov, S. Vorobiev, J. E. Dick and S. D. Tanner, *Anal Chem*, 2009, **81**, 6813-6822.

132. S. C. Bendall, E. F. Simonds, P. Qiu, A. D. Amir el, P. O. Krutzik, R. Finck, R. V. Bruggner, R. Melamed, A. Trejo, O. I. Ornatsky, R. S. Balderas, S. K. Plevritis, K. Sachs, D. Pe'er, S. D. Tanner and G. P. Nolan, *Science*, 2011, **332**, 687-696.

133. C. Giesen, H. A. Wang, D. Schapiro, N. Zivanovic, A. Jacobs, B. Hattendorf, P. J. Schuffler, D. Grolimund, J. M. Buhmann, S. Brandt, Z. Varga, P. J. Wild, D. Gunther and B. Bodenmiller, *Nat Methods*, 2014, **11**, 417-422.

134. G. C. Le Goff, R. L. Srinivas, W. A. Hill and P. S. Doyle, *Eur Polym J*, 2015, **72**, 386-412.

135. M. E. Byrne, K. Park and N. A. Peppas, *Advanced Drug Delivery Reviews*, 2002, **54**, 149-161.

136. L. Brannon-Peppas and N. A. Peppas, *Chemical Engineering Science*, 1991, **46**, 715-722.

137. N. A. Peppas, P. Bures, W. Leobandung and H. Ichikawa, *Eur J Pharm Biopharm*, 2000, **50**, 27-46.

138. D. C. Appleyard, S. C. Chapin and P. S. Doyle, *Anal Chem*, 2011, **83**, 193-199.

139. D. C. Appleyard, S. C. Chapin, R. L. Srinivas and P. S. Doyle, *Nat Protoc*, 2011, **6**, 1761-1774.

140. H. Lee, J. Kim, H. Kim, J. Kim and S. Kwon, *Nat Mater*, 2010, **9**, 745-749.

141. Y. LeCun, Y. Bengio and G. Hinton, *Nature*, 2015, **521**, 436.

142. J. C. Caicedo, S. Cooper, F. Heigwer, S. Warchal, P. Qiu, C. Molnar, A. S. Vasilevich, J. D. Barry, H. S. Bansal, O. Kraus, M. Wawer, L. Paavolainen, M. D. Herrmann, M. Rohban, J. Hung, H. Hennig, J. Concannon, I. Smith, P. A. Clemons, S. Singh, P. Rees, P. Horvath, R. G. Linington and A. E. Carpenter, *Nature Methods*, 2017, **14**, 849.

143. T. J. Merkel, K. P. Herlihy, J. Nunes, R. M. Orgel, J. P. Rolland and J. M. DeSimone, *Langmuir*, 2010, **26**, 13086-13096.

144. C. M. Hwang, W. Y. Sim, S. H. Lee, A. M. Foudeh, H. Bae, S. H. Lee and A. Khademhosseini, *Biofabrication*, 2010, **2**, 045001.

145. B. E. Jensen, A. A. Smith, B. Fejerskov, A. Postma, P. Senn, E. Reimhult, M. Pla-Roca, L. Isa, D. S. Sutherland, B. Stadler and A. N. Zelikin, *Langmuir*, 2011, **27**, 10216-10223.

146. A. Khademhosseini, G. Eng, J. Yeh, J. Fukuda, J. Blumling, 3rd, R. Langer and J. A. Burdick, *J Biomed Mater Res A*, 2006, **79**, 522-532.

147. S. Jung and H. Yi, *Langmuir*, 2012, **28**, 17061-17070.

148. S. Jung and H. Yi, *Biomacromolecules*, 2013, **14**, 3892-3902.

149. C. H. Choi, J. Lee, K. Yoon, A. Tripathi, H. A. Stone, D. A. Weitz and C. S. Lee, *Angew Chem Int Ed Engl*, 2010, **49**, 7748-7752.

150. J. P. Rolland, B. W. Maynor, L. E. Euliss, A. E. Exner, G. M. Denison and J. M. DeSimone, *J Am Chem Soc*, 2005, **127**, 10096-10100.

151. S. E. Gratton, P. D. Pohlhaus, J. Lee, J. Guo, M. J. Cho and J. M. Desimone, *J Control Release*, 2007, **121**, 10-18.

152. A. I. Neto, K. Demir, A. A. Popova, M. B. Oliveira, J. F. Mano and P. A. Levkin, *Adv Mater*, 2016, **28**, 7613-7619.

153. Y. Lu, M. Sturek and K. Park, *Int J Pharm*, 2014, **461**, 258-269.

154. G. Acharya, C. S. Shin, M. McDermott, H. Mishra, H. Park, I. C. Kwon and K. Park, *J Control Release*, 2010, **141**, 314-319.

155. D. Dendukuri, D. C. Pregibon, J. Collins, T. A. Hatton and P. S. Doyle, *Nat Mater*, 2006, **5**, 365-369.

156. K. W. Bong, J. Xu, J. H. Kim, S. C. Chapin, M. S. Strano, K. K. Gleason and P. S. Doyle, *Nat Commun*, 2012, **3**, 805.

157. K. W. Bong, D. C. Pregibon and P. S. Doyle, *Lab Chip*, 2009, **9**, 863-866.

158. S. C. Chapin, D. C. Pregibon and P. S. Doyle, *Lab Chip*, 2009, **9**, 3100-3109.

159. G. C. Le Goff, J. Lee, A. Gupta, W. A. Hill and P. S. Doyle, *Adv Sci (Weinh)*, 2015, **2**, 1500149.

160. D. C. Pregibon and P. S. Doyle, *Anal Chem*, 2009, **81**, 4873-4881.

161. C. L. Lewis, Y. Lin, C. Yang, A. K. Manocchi, K. P. Yuet, P. S. Doyle and H. Yi, *Langmuir*, 2010, **26**, 13436-13441.

162. M. A. Al-Ameen and G. Ghosh, *Biosens Bioelectron*, 2013, **49**, 105-110.

163. W. Lee, D. Choi, J. H. Kim and W. G. Koh, *Biomed Microdevices*, 2008, **10**, 813-822.

164. S. Park, H. J. Lee and W. G. Koh, *Sensors (Basel)*, 2012, **12**, 8426-8436.

165. N. C. dupont, K. Wang, P. D. Wadhwa, J. F. Culhane and E. L. Nelson, *J Reprod Immunol*, 2005, **66**, 175-191.

166. D. C. Pregibon, M. Toner and P. S. Doyle, *Science*, 2007, **315**, 1393-1396.

167. B. Biosciences, *Journal*, 2016.

168. N. Baumgarth and M. Roederer, *Journal of Immunological Methods*, 2000, **243**, 77-97.

169. ImageStreamX Mark II Imaging Flow Cytometer, (accessed May 9th, 2016).

170. A. Astashkina and D. W. Grainger, *Adv Drug Deliv Rev*, 2014, **69-70**, 1-18.

171. C. Fischbach, H. J. Kong, S. X. Hsiong, M. B. Evangelista, W. Yuen and D. J. Mooney, *Proc Natl Acad Sci U S A*, 2009, **106**, 399-404.

172. G. M. Cruise, D. S. Scharp and J. A. Hubbell, *Biomaterials*, 1998, **19**, 1287-1294.

173. N. S. Hwang, S. Varghese, Z. Zhang and J. Elisseeff, *Tissue engineering*, 2006, **12**, 2695-2706.

174. C. A. DeForest and K. S. Anseth, *Angew Chem Int Ed Engl*, 2012, **51**, 1816-1819.

175. H. A. Awad, M. Q. Wickham, H. A. Leddy, J. M. Gimble and F. Guilak, *Biomaterials*, 2004, **25**, 3211-3222.

176. T. G. Fernandes, M. M. Diogo, D. S. Clark, J. S. Dordick and J. M. Cabral, *Trends Biotechnol*, 2009, **27**, 342-349.

177. J. J. Kim, K. W. Bong, E. Reategui, D. Irimia and P. S. Doyle, *Nat Mater*, 2017, **16**, 139-146.

178. D. Barata, C. van Blitterswijk and P. Habibovic, *Acta Biomater*, 2016, **34**, 1-20.

179. N. W. Choi, J. Kim, S. C. Chapin, T. Duong, E. Donohue, P. Pandey, W. Broom, W. A. Hill and P. S. Doyle, *Anal Chem*, 2012, **84**, 9370-9378.

180. E. Jang and W.-G. Koh, *Sensors and Actuators B: Chemical*, 2010, **143**, 681-688.

181. A. Revzin, R. J. Russell, V. K. Yadavalli, W.-G. Koh, C. Deister, D. D. Hile, M. B. Mellott and M. V. Pishko, *Langmuir*, 2001, **17**, 5440-5447.

182. M. Roederer, *Cytometry*, 2001, **45**, 194-205.

183. A. I. Konokhova, M. A. Yurkin, A. E. Moskalensky, A. V. Chernyshev, G. A. Tsvetovskaya, E. D. Chikova and V. P. Maltsev, *J Biomed Opt*, 2012, **17**, 057006.

184. R. Mathaes, G. Winter, J. Engert and A. Besheer, *Int J Pharm*, 2013, **453**, 620-629.

185. A. K. Lau, H. C. Shum, K. K. Wong and K. K. Tsia, *Lab Chip*, 2016, **16**, 1743-1756.

186. Y. Saeys, S. Van Gassen and B. N. Lambrecht, *Nat Rev Immunol*, 2016, **16**, 449-462.

187. J. D. Kretlow and A. G. Mikos, *Tissue engineering*, 2007, **13**, 927-938.

188. V. Karageorgiou and D. Kaplan, *Biomaterials*, 2005, **26**, 5474-5491.

189. V. Keskar, N. W. Marion, J. J. Mao and R. A. Gemeinhart, *Tissue Eng Part A*, 2009, **15**, 1695-1707.

190. D. A. Wang, C. G. Williams, F. Yang, N. Cher, H. Lee and J. H. Elisseeff, *Tissue engineering*, 2005, **11**, 201-213.

191. L. E. Jansen, L. J. Negron-Pineiro, S. Galarza and S. R. Peyton, *Acta Biomater*, 2018, **70**, 120-128.

192. E. Jang and W. G. Koh, *Sensor Actuat B-Chem*, 2010, **143**, 681-688.

193. K. M. Yamada and E. Cukierman, *Cell*, 2007, **130**, 601-610.

194. J. Lee, A. A. Abdeen, K. L. Wycislo, T. M. Fan and K. A. Kilian, *Nat Mater*, 2016, **15**, 856-862.